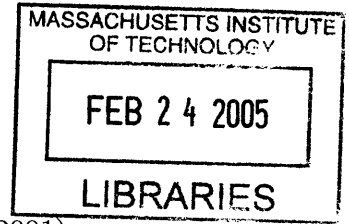# Prediction of Early-Age Cracking of UHPC Materials and Structures: A Thermo-Chemo-Mechanics Approach

by

JongMin Shim

M.S., Korea Advanced Institute of Science of Technology (2001)
B.S., Korea Advanced Institute of Science of Technology (1998)

Submitted to the Department of Civil and Environmental Engineering
in partial fulfillment of the requirements for the degree of

Master of Science in Civil and Environmental Engineering

at the

MASSACHUSETTS INSTITUTE OF TECHNOLOGY

February 2005

Signature of Author....................
Department of Civil and Environmental Engineering
February 1, 2005

Certified by...
Franz-Josef Ulm
Associate Professor of Civil and Environmental Engineering
Thesis Supervisor

Accepted by.............................
Andrew Whittle
Chairperson, Department Committee on Graduate Studies

Prediction of Early-Age Cracking of UHPC Materials and Structures: A Thermo-Chemo-Mechanics Approach

by

JongMin Shim

Submitted to the Department of Civil and Environmental Engineering
on February 1, 2005, in partial fulfillment of the
requirements for the degree of
Master of Science in Civil and Environmental Engineering

Abstract

Ultra-High Performance Concrete [UHPC] has remarkable performance in mechanical properties, ductility, economical benefit, etc., but early-age cracking of UHPC can become an issue during the manufacturing process due to the high cement content and the highly exothermic hydration reaction. Because of the risk of early-age UHPC cracking, there is a need to develop a material model that captures the behavior of UHPC at early-ages.

The objective of this research is to develop a new material model for early-age UHPC through a thermodynamics approach. The new model is a two-phase thermo-chemo-mechanical model, which is based on two pillars: the first is a hardened two-phase UHPC material model, and the second is a hydration kinetics model for ordinary concrete. The coupling of these two models is achieved by considering the evolution of the strength and stiffness properties in the two-phase UHPC material model in function of the hydration degree.

The efficiency of the model and finite element implementation is validated with experimental data obtained during the casting of a Ductal^{TM} optimized bridge girder. Based on some decoupling hypothesis, the application of the early-age UHPC model can be carried out in a two-step manner: the thermo-chemical problem is solved first, before solving the two-phase thermo-chemo-mechanical problem. It is shown that the newly developed model is able to accurately predict temperature history and deformation behavior of the bridge girder. Furthermore, with this versatile engineering model, it is possible to predict the risk of cracking, and eventually to reduce it.

Thesis Supervisor: Franz-Josef Ulm
Title: Associate Professor of Civil and Environmental Engineering

3

Contents

List of Tables

List of Figures

10

11

Chapter 1

INTRODUCTION

1.1 Project Description

Ultra-High Performance Concrete [UHPC] is a new generation of fiber reinforced cementitious materials with enhanced mechanical and aesthetic properties. An example of UHPC is Ductal^{TM}, made by Lafarge, shown in Figure 1-1. It is composed of 710 kg/m^3 of cement and 160 kg/m^3 of steel fibers. Moreover, it has a very low water cement ratio of roughly 20 %, and superplasticizer is employed in this material to ensure workability. A typical mix design for Ductal^{TM}-Steel Fiber is given in Table 1.1. Its remarkable properties can be summarized as follows:

- It has $3 - 7$ times the compressive, flexural, and tensile strength of normal concrete;

- It behaves as an elasto-plastic ductile material in tension;

- It allows smaller section sizes which do not require secondary steel reinforcement;

- It has high workability which enables structural elements to be cast in any shape.

Thus, UHPC eventually enables the reduction of global construction costs by using less materials, allowing faster construction, reducing labour, reducing maintenance, increasing usage life, etc. However, due to the high cement content and highly exothermal hydration reaction, early-age cracking can become an issue during the manufacturing process.
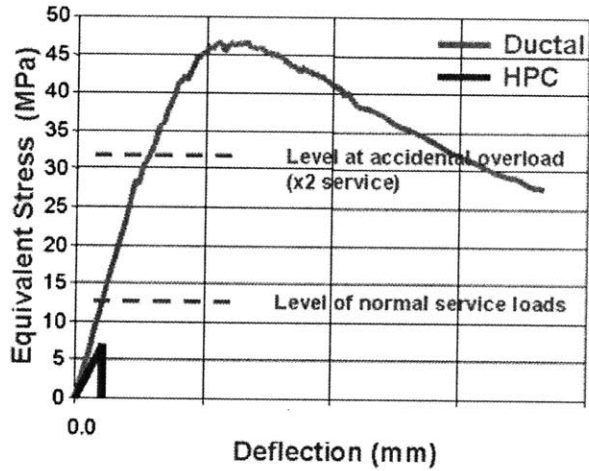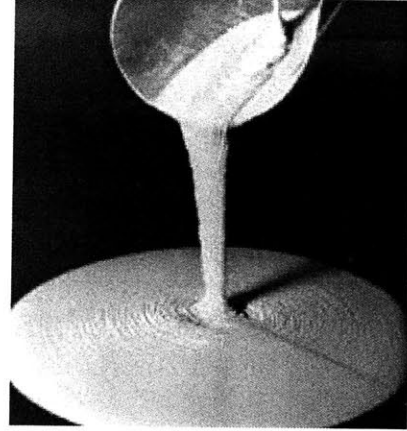
Figure 1-1: (a) Comparison of the flexural strength of UHPC (Ductal^{TM}) and Conventional Concrete (HPC), (b) Enhanced rheology of Ductal^{TM} [12].

Material	Mass/Volume [kg/m^3]	Mass Ratio
Cement	710	1.000
Silica Fume	230	0.324
Ground Quartz	210	0.296
Sand	1020	1.437
Metallic Fibers	160	0.225
Superplasticizer	13	0.018
Water	140	0.197

Table 1.1: A typical mix design for Ductal^{TM}-Steel Fiber [12].

15

As a part of a UHPC bridge development program, Prestress Service Inc. [PSi] cast four Ductal^{TM} optimized bridge girders at Lexington, Kentucky. These tests were carried out under contract of the Federal Highway Administration [FHWA] over the period of October 11, 2003 to January 31, 2004 (Figure 1-2). The optimized girder section was developed at MIT using a model-based simulation approach [18], with the collaboration of FHWA, PSi and Lafarge North America. During casting of the girders, early-age cracks were observed, and one of them is shown in Figure 1-3. Thus, it becomes clear that an accurate modeling of the behavior of UHPC at early ages is necessary to avoid early-age cracking, which affects the durability of UHPC structures.

1.2 Research Objective and Approach

The ultimate industrial goal of this research is the prevention of early-age cracking in UHPC structures. The first step toward this goal is to predict when and where early-age cracking occurs in a structure so that one can reduce the risk of cracking. To reach this goal, there is a necessity to develop a material model which captures the behavior of UHPC at early ages. This development, which is focus of this research, is based on two previous developments: a hardened UHPC material model and a hydration kinetics model.

More precisely, a two-phase constitutive model for hardened UHPC materials has been recently developed at MIT [7]. This nonlinear constitutive model for UHPC was implemented in a commercial finite element program, CESAR-LCPC, and validated for 2-D and 3-D structures [7] [21]. The model has been also used for the design of a prototype UHPC highway bridge girder for the U.S. market place [18].

Hydration of concrete is a highly exothermic and thermally activated reaction, so that a thermochemical model is necessary for the modeling of hydration reaction. A simple hydration kinetics model for ordinary early-age concrete is the one developed by Ulm and Coussy [25] [26]. In this model, it is assumed that the diffusion of water through the layers of hydrates is the dominant mechanism of the hydration kinetics. The hydration process of concrete is viewed, from a macroscopic perspective, as a single chemical reaction in which the free water is a reactant phase that combines with the unhydrated phase to form solid material.
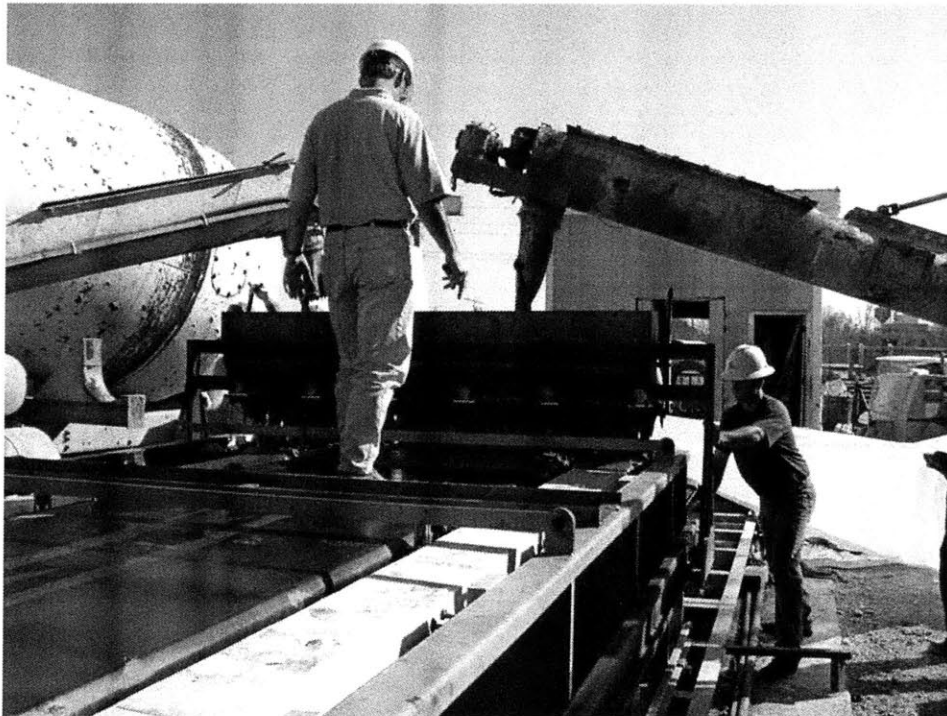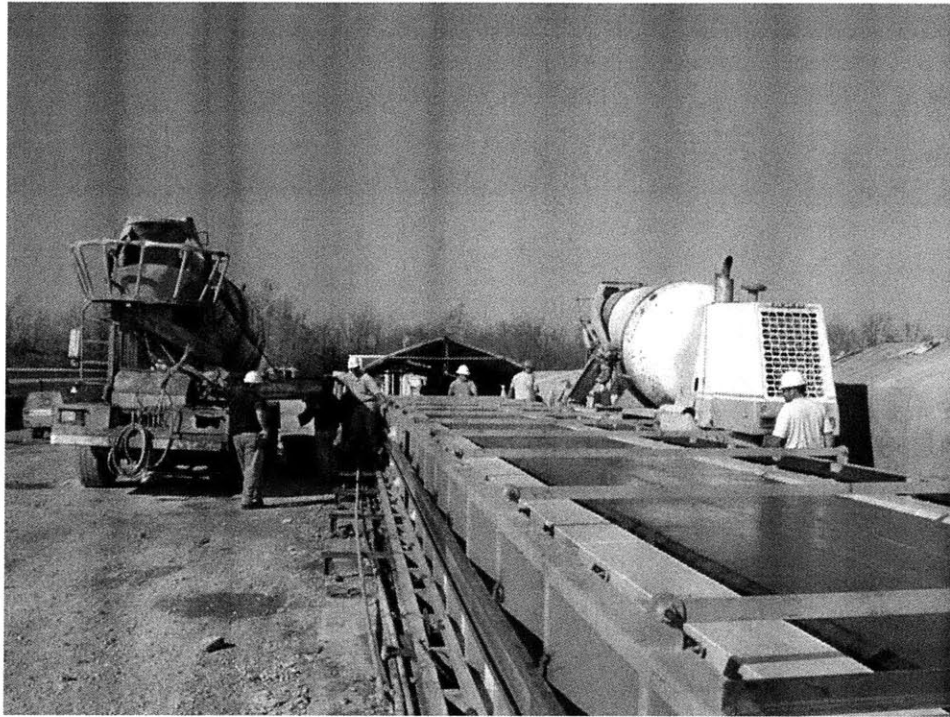
Figure 1-2: Construction of the Ductal^{TM} bridge girders at Lexington, Kentucky [9].
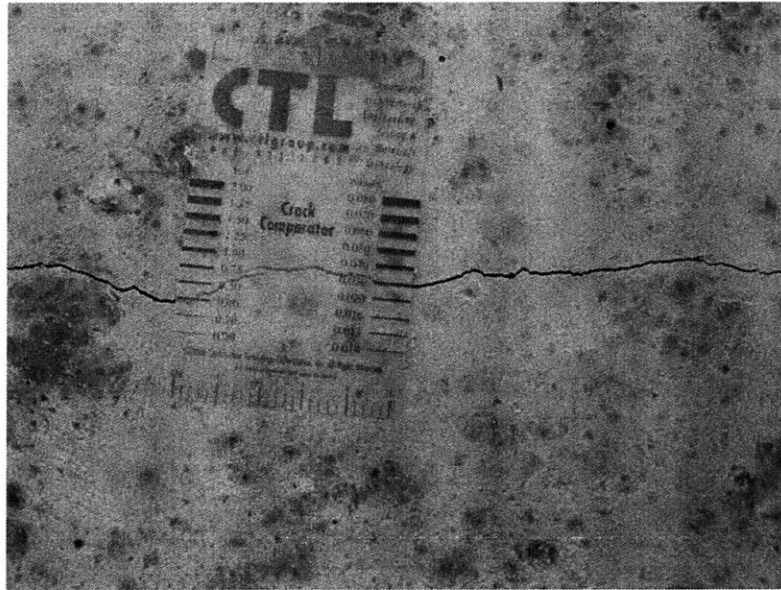
Figure 1-3: Early-age cracking observed during casting of on UHPC bridge girder [9].

Given these backgrounds, the objective of the presented research is to develop a new material model for early-age UHPC, which combines these two approaches: the MIT-UHPC model and the Ulm-Coussy hydration model. In order to achieve the research objectives, the following tasks need to be performed:

1. To understand the hardened UHPC material model;

2. To combine the hydration kinetics model with the hardened UHPC material model;

3. To implement the new material model into a finite element program;

4. To validate the proposed material model through an application to a UHPC structure.

1.3 Outline of Report

This report is divided into seven chapters, starting with the hardened UHPC material model and the hydration kinetics model, moving on to the development of the novel early-age UHPC material model and its finite element implementation, and finishing with the validation of the proposed model.

Chapter 2 begins with a brief review of the two-phase hardened UHPC material model. The two-phase model reflects the material composition with one phase representing the matrix and the other representing the reinforcing fibers. This separation of the overall composite behavior into individual matrix and fiber phases is very effective because the plastic strain in the composite matrix is used to represent the cracking in the UHPC material.

Chapter 3 reviews the hydration kinetics model for ordinary concrete. One important assumption of this kinetics model is the decoupling hypothesis, which neglects the effect of mechanical change on the thermal and chemical process.

In Chapter 4, the newly developed early-age UHPC material model is presented in detail. The coupling of the two mentioned models requires to consider the evolution of the strength and stiffness properties in the two-phase UHPC material model.

Chapter 5 presents details of the implementation of the early-age UHPC models in a finite element environment. The implementation is verified for consistency and stability with respect to analytical models and mesh size to demonstrate the viability of the finite element implementation.

Chapter 6 is devoted to structural simulations using the finite element program. The effectiveness of the model and finite element program is validated with experimental data. Thanks to the decoupling hypothesis, the application of the early-age UHPC model is carried out in a two-step manner: thermo-chemical problem and then two-phase thermo-chemo-mechanical problem. In this Chapter, the simulation results from both problems are compared with experimental data from the Kentucky casting.

Finally, Chapter 7 summarizes the results of this project, and discusses current limitations and suggestions for future research.

Part I

BACKGROUND WORKS

Chapter 2

HARDENED UHPC MATERIAL MODEL

One of the great benefits of UHPC is that it shows considerable tensile strength that can be taken into account in the design of UHPC structures. Thus, the tensile behavior of UHPC needs to be captured correctly in a UHPC constitutive model. This Chapter reviews the UHPC material model that has been developed at MIT [7]. The model is a two-phase model; one phase representing the matrix and the other phase representing the reinforcing fibers. In addition, the matrix-fiber interaction is taken into account as an internal coupling effect between the irreversible deformation of the composite constituents.

2.1   Hardened UHPC Material Behavior

A typical tensile response of hardened UHPC is shown in Figure 2-1 (a). It can be simplified into four domains shown in Figure 2-1 (b); first a linear elastic behavior, second a brittle strength drop, third a post-cracking behavior, and fourth a composite yielding. Figure 2-2 shows the simplified macroscopic stress-strain behavior of UHPC (macroscopic stress, Σ, and macroscopic strain, E) and the evolution of the matrix and the fiber stresses (σ_F and σ_M) for the modeling of UHPC. This simplified stress-strain behavior can be described by the following three stages:

1. Initial Elasticity: When the composite is first loaded, UHPC behaves elastically with a stiffness of K_0 until the composite stress reaches an initial tensile strength $\Sigma_{t,1}^-$. At this
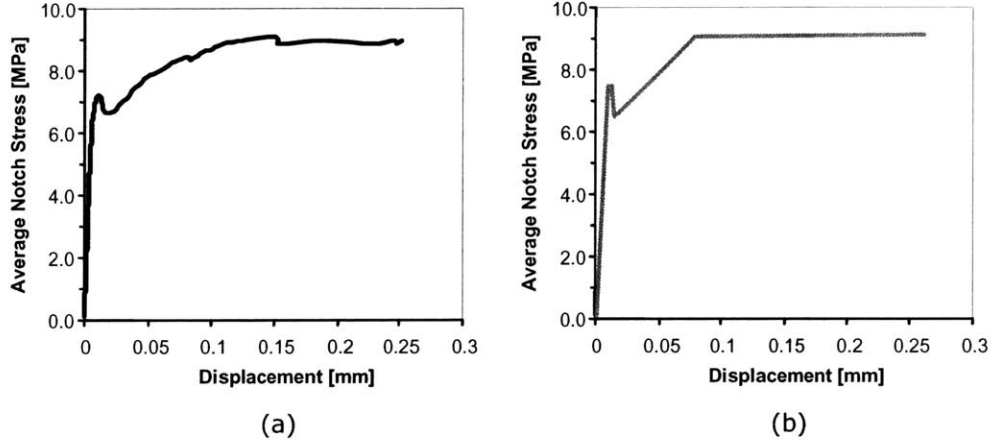
Figure 2-1: (a) Experimental notched tensile test data of a UHPC material with steel fibers [5], (b) Stress-displacement response extracted from the test data.

point, significant cracking in the matrix develops causing a stress drop to a post-cracking tensile strength $\Sigma_{t,1}^+$.

2. Post-cracking Behavior: After the matrix cracks, there is a second linear behavior with a stiffness of K_1 until the fibers start to yield.

3. Yielding and Failure: Finally, the composite yields and ultimately fails at an ultimate tensile yield strength $\Sigma_{t,2}$. Tension softening behavior is neglected in the material model.

The complex tensile behavior is condensed into five macroscopic material properties (K_0, K_1, $\Sigma_{t,1}^-$, $\Sigma_{t,1}^+$, and $\Sigma_{t,2}$), which can be extracted from tensile test data.

2.2 Hardened 1-D UHPC Model

In order to represent the simplified UHPC material behavior, Chuang and Ulm [8] proposed the 1-D Think Model displayed in Figure 2-3. In this model, matrix and fiber phases are modeled as separate phases with the same macroscopic strain, E, but with different stress states, σ_M and σ_F. In turn, the macroscopic stress, Σ, is always the sum of the composite matrix stress, σ_M, and the composite fiber stress, σ_F.
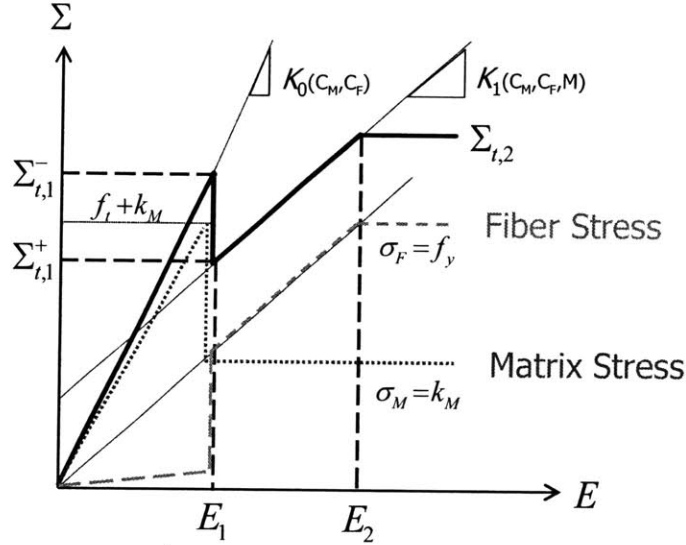
Figure 2-2: Simplified stress-strain curve for the two-phase model.

The macroscopic material model is composed of three parts: a brittle-plastic matrix phase, an elasto-plastic fiber phase and an elastic coupling spring. The matrix phase consists of an elastic spring of stiffness C_M, a tensile plate element of strength f_t, and a frictional element of strength k_M. From a micro-mechanical point of view, the elastic spring represents the elastic *contribution* of the matrix, the plate device represents the brittle behavior of the matrix and the frictional device represents the fracture resistance of the matrix. The fiber phase behavior is represented by an elastic spring of stiffness C_F, and a frictional element of strength f_y. The elastic spring represents the elastic *contribution* of the fibers and the friction element can be associated with the plastic pullout behavior of the fibers during composite yielding. In addition, the two parallel phases are coupled by an elastic spring of stiffness M, which links the irreversible matrix behavior (plastic strain ε_M^p) with the irreversible reinforcing fiber behavior (plastic strain ε_F^p). At the micro-scale, this elastic coupling can be associated with a possible shear stress transfer from the matrix to the fiber over their interface, and intact matrix ligaments which transfer stresses even after cracking. The 6 model parameters (C_M, C_F, M, f_t, k_M and f_y) govern the tensile behavior of the composite material.

While a single tensile stress-strain relation provides *five* macroscopic material properties
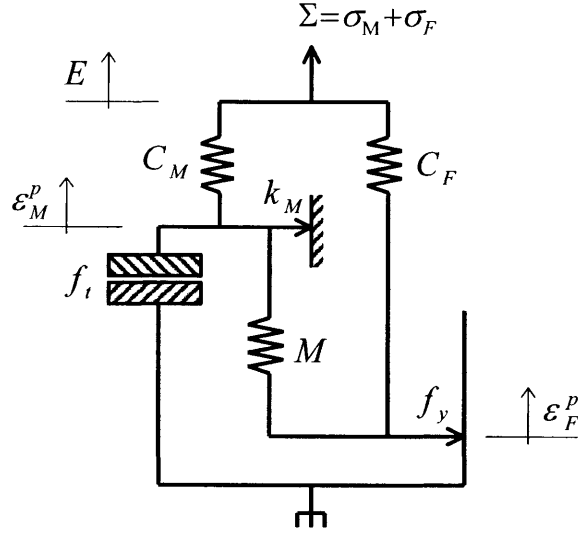
Figure 2-3: 1D Think Model of a two-phase matrix-fiber composite material for hardened UHPC.

$(K_0, K_1, \Sigma_{t,1}^-, \Sigma_{t,1}^+$ and $\Sigma_{t,2})$, the composite model involves *six* model parameters $(C_M, C_F, M, f_t, k_M$ and $f_y)$. They are related by the following equations:

$$K_0 = C_M + C_F$$
$$K_1 = C_F + \frac{C_M M}{C_M + M}$$

$$(2.1)$$

$$\Sigma_{t,1}^- = \left(1 + \frac{C_F}{C_M}\right)(f_t + k_M) \quad \text{with} \quad E_1^- = \frac{f_t + k_M}{C_M}$$
$$\Sigma_{t,1}^+ = \Sigma_{t,1}^- - \frac{C_M}{C_M + M} f_t \quad \text{with} \quad E_1^+ = \frac{f_t + k_M}{C_M}$$
$$\Sigma_{t,2} = f_y + k_M \quad \text{with} \quad E_2 = \frac{k_M M + f_y(C_M + M)}{C_F(C_M + M) + C_M M}$$

$$(2.2)$$

Thus, in order to close the identification problem of model parameters, another relation is required. A typical UHPC material has a characteristic low fiber volume fraction, $c_F = \frac{V_F}{V} \leq$ 6%. For $c_F \leq 6\%$ and typical elastic moduli of the matrix and the fiber phases, the composite stiffness ratio, $\kappa = \frac{C_F}{C_M}$, shows the following range of values:

$$0.02 \leq \kappa \leq 0.13$$

$$(2.3)$$

Thus, the six model parameters can be practically obtained by an asymptotic analysis, setting the composite stiffness ratio $\kappa \to 0$. Then, (2.1) and (2.2) reduce to:

$$K_0 \simeq C_M$$
$$K_1 \simeq \frac{C_M M}{C_M + M}$$

(2.4)

$$\Sigma_{t,1}^- \simeq f_t + k_M \quad \text{with} \quad E_1^- = \frac{f_t + k_M}{C_M}$$
$$\Sigma_{t,1}^+ \simeq k_M \quad \text{with} \quad E_1^+ = \frac{f_t + k_M}{C_M}$$
$$\Sigma_{t,2} = f_y + k_M \quad \text{with} \quad E_2 \simeq \frac{k_M M + f_y(C_M + M)}{C_M M}$$

(2.5)

2.3 Hardened 3-D UHPC Model

The 1-D Think Model has the ability to continuously model the stress-strain behavior of UHPC materials while capturing the micro-mechanical behavior of the composite material. Since the UHPC material model is a macroscopic model, the extension to 3-D is straightforward, essentially requiring to substitute for 1-D macroscopic parameters and functions with their 3-D counterparts. The 3-D macroscopic model is constructed around three main components:

- The 3-D constitutive relations: The 3-D stress-strain relation is derived from the energy consideration for a stress-strain expression which is thermodynamically consistent with the 1-D result.

- Plasticity of the 3-D model: The 3-D failure criteria and the corresponding plastic flow rules are considered. The 3-D loading functions require 3-D strength limits, i.e. tension, compression, shear, etc. An associated plastic flow rule is adopted.

- Consistency with the 1-D model: The uniaxial behavior of the 3-D model is calibrated with the 1-D model so that the 3-D model gives tension output which is consistent with that of the 1-D model.

These different components, developed in detail in [7], are briefly recalled below.

2.3.1 The 3-D Constitutive Relations

The starting point of the 3-D model is the Clausius-Duhem inequality, which for isothermal conditions reads [24]:

$$\varphi dt = \mathbf{\Sigma} : d\mathbf{E} - d\Psi \geq 0 \tag{2.6}$$

where φdt stands for the dissipation; $\mathbf{\Sigma}$ and $\mathbf{E}$ are the 2nd order macroscopic stress tensor and macroscopic strain tensor, respectively; and Ψ is the free energy. For UHPC materials, using the elastic contribution of the different springs in Figure 2-3, the free energy reads:

$$
\begin{aligned}
\Psi &= \Psi\left(\mathbf{E}, \varepsilon_M^p, \varepsilon_F^p\right) \\
&= \frac{1}{2}\left(\mathbf{E} - \varepsilon_M^p\right) : \mathbb{C}_M : \left(\mathbf{E} - \varepsilon_M^p\right) + \frac{1}{2}\left(\mathbf{E} - \varepsilon_F^p\right) : \mathbb{C}_F : \left(\mathbf{E} - \varepsilon_F^p\right) \\
&\quad + \frac{1}{2}\left(\varepsilon_M^p - \varepsilon_F^p\right) : \mathbb{M} : \left(\varepsilon_M^p - \varepsilon_F^p\right)
\end{aligned}
\tag{2.7}
$$

where $\mathbb{C}_M$, $\mathbb{C}_F$, and $\mathbb{M}$ are the 4th order stiffness tensors of the composite matrix, the composite fiber, and the matrix-fiber coupling, respectively. Use of (2.7) in (2.6) yields the incremental form of the general 3-D stress-strain relations, which is an incremental form read:

$$
\left\{
\begin{array}{c}
d\mathbf{\Sigma} \\
d\boldsymbol{\sigma}_M \\
d\boldsymbol{\sigma}_F
\end{array}
\right\}
=
\left[
\begin{array}{cc}
\mathbb{C}_M & \mathbb{C}_F \\
\mathbb{C}_M + \mathbb{M} & -\mathbb{M} \\
-\mathbb{M} & \mathbb{C}_F + \mathbb{M}
\end{array}
\right]
:
\left\{
\begin{array}{c}
d\mathbf{E} - d\varepsilon_M^p \\
d\mathbf{E} - d\varepsilon_F^p
\end{array}
\right\}
\tag{2.8}
$$

We verify that the macroscopic stress, $\mathbf{\Sigma}$, is always the sum of the matrix stress, $\boldsymbol{\sigma}_M$, and fiber stress, $\boldsymbol{\sigma}_F$:

$$
\begin{aligned}
d\mathbf{\Sigma} &= d\boldsymbol{\sigma}_M + d\boldsymbol{\sigma}_F \\
&= \left(\mathbb{C}_M + \mathbb{M}\right) : \left(d\mathbf{E} - d\varepsilon_M^p\right) - \mathbb{M} : \left(d\mathbf{E} - d\varepsilon_F^p\right) \\
&\quad + \left(\mathbb{C}_F + \mathbb{M}\right) : \left(d\mathbf{E} - d\varepsilon_F^p\right) - \mathbb{M} : \left(d\mathbf{E} - d\varepsilon_M^p\right)
\end{aligned}
\tag{2.9}
$$

The general 3-D constitutive model with matrix-fiber interaction involves 3×21 stiffness parameters associated with the stiffness tensors, $\mathbb{C}_M$, $\mathbb{C}_F$, and $\mathbb{M}$. In a first approach to

26

UHPC materials with random fiber orientation, the behavior can be assumed to be isotropic. Similarly, using the assumption of randomly oriented cracks after matrix cracking, the post-cracking stiffness behavior of the modeled material can also be approximated as isotropic. In this case, the stiffness tensors can be described with two unique scalar values:

$$\mathbb{C}_M = 3K_M\mathbb{K} + 2G_M\mathbb{J}$$
$$\mathbb{C}_F = 3K_F\mathbb{K} + 2G_F\mathbb{J} \tag{2.10}$$
$$\mathbb{M} = 3K_I\mathbb{K} + 2G_I\mathbb{J}$$

where $\mathbb{K} = K_{ijkl} = \frac{1}{3}\delta_{ij}\delta_{kl}$ is the volumetric part of the 4th order unit tensor $\mathbb{I}$, and $\mathbb{J} = \mathbb{I} - \mathbb{K}$ is the deviatoric part [1]. K_M, K_F and K_I are the bulk moduli of the composite matrix, the composite fiber and the matrix-fiber coupling; G_M, G_F and G_I are the shear moduli of the composite matrix, the composite fiber and the matrix-fiber coupling. The bulk moduli and the shear moduli are related to elastic moduli of the composite matrix, C_M, the composite fiber, C_F, and matrix-fiber coupling, M, by:

$$
\begin{aligned}
K_M &= \frac{C_M}{3(1-2\nu_M)}; & G_M &= \frac{C_M}{2(1+\nu_M)}; \\
K_F &= \frac{C_F}{3(1-2\nu_F)}; & G_F &= \frac{C_F}{2(1+\nu_F)}; \\
K_I &= \frac{M^{3D}}{3(1-2\nu_I)}; & G_I &= \frac{M^{3D}}{2(1+\nu_I)}
\end{aligned}
\tag{2.11}
$$

where ν_M, ν_F and ν_I are the Poisson's ratios of the composite matrix, the composite fiber and the matrix-fiber coupling, respectively; and M^{3D} is the 3-D counterpart of M in the 1-D model (Figure 2-3). However, unlike the composite matrix stiffness and the composite fiber stiffness, the 3-D coupling stiffness tensor $\mathbb{M}$ is not directly related to its 1-D counterpart M. The 3-D coupling stiffness tensor must be formulated in such a way that the 3-D model gives the same macroscopic uniaxial response as the 1-D model, as detailed later on.

---

[1] The symmetric 4th order tensors can be written in the following matrix forms:

$$
\mathbb{I} = \begin{bmatrix}
1 & 0 & 0 & 0 & 0 & 0 \\
0 & 1 & 0 & 0 & 0 & 0 \\
0 & 0 & 1 & 0 & 0 & 0 \\
0 & 0 & 0 & 1 & 0 & 0 \\
0 & 0 & 0 & 0 & 1 & 0 \\
0 & 0 & 0 & 0 & 0 & 1
\end{bmatrix};
\quad
\mathbb{K} = \begin{bmatrix}
\frac{1}{3} & \frac{1}{3} & \frac{1}{3} & 0 & 0 & 0 \\
\frac{1}{3} & \frac{1}{3} & \frac{1}{3} & 0 & 0 & 0 \\
\frac{1}{3} & \frac{1}{3} & \frac{1}{3} & 0 & 0 & 0 \\
0 & 0 & 0 & 0 & 0 & 0 \\
0 & 0 & 0 & 0 & 0 & 0 \\
0 & 0 & 0 & 0 & 0 & 0
\end{bmatrix};
\quad
\mathbb{J} = \begin{bmatrix}
\frac{2}{3} & -\frac{1}{3} & -\frac{1}{3} & 0 & 0 & 0 \\
-\frac{1}{3} & \frac{2}{3} & -\frac{1}{3} & 0 & 0 & 0 \\
-\frac{1}{3} & -\frac{1}{3} & \frac{2}{3} & 0 & 0 & 0 \\
0 & 0 & 0 & 1 & 0 & 0 \\
0 & 0 & 0 & 0 & 1 & 0 \\
0 & 0 & 0 & 0 & 0 & 1
\end{bmatrix}
$$

Equation (2.8) can be restated in an isotropic format:

$$d\mathbf{\Sigma} = d\Sigma^v \mathbf{1} + d\mathbf{\Sigma}^d$$
$$d\boldsymbol{\sigma}_M = d\sigma^v_M \mathbf{1} + d\mathbf{s}_M \qquad (2.12)$$
$$d\boldsymbol{\sigma}_F = d\sigma^v_F \mathbf{1} + d\mathbf{s}_F$$

where $\mathbf{1}$ is the 2nd order unit tensor; $d\Sigma^v = \frac{1}{3}tr\,(d\mathbf{\Sigma})$, $d\sigma^v_M = \frac{1}{3}tr\,(d\boldsymbol{\sigma}_M)$ and $d\sigma^v_F = \frac{1}{3}tr\,(d\boldsymbol{\sigma}_F)$ are volumetric stress increments; and $d\mathbf{\Sigma}^d$, $d\mathbf{s}_M$ and $d\mathbf{s}_F$ are deviatoric stress increments. The volumetric stress-strains are represented by:

$$
\left\{
\begin{array}{c}
d\Sigma^v \\
d\sigma^v_M \\
d\sigma^v_F
\end{array}
\right\}
= 3
\left[
\begin{array}{cc}
K_M & K_F \\
K_M + K_I & -K_I \\
-K_I & K_F + K_I
\end{array}
\right]
\left\{
\begin{array}{c}
dE^v - d\epsilon^p_M \\
dE^v - d\epsilon^p_F
\end{array}
\right\}
\qquad (2.13)
$$

where $dE^v = \frac{1}{3}tr\,(d\mathbf{E})$, $d\epsilon^p_M = \frac{1}{3}tr\,(d\varepsilon^p_M)$ and $d\epsilon^p_F = \frac{1}{3}tr\,(d\varepsilon^p_F)$ are volumetric strain increments. Similarly, the deviatoric stress-strain relations are given by:

$$
\left\{
\begin{array}{c}
d\mathbf{\Sigma}^d \\
d\mathbf{s}_M \\
d\mathbf{s}_F
\end{array}
\right\}
= 2
\left[
\begin{array}{cc}
G_M & G_F \\
G_M + G_I & -G_I \\
-G_I & G_F + G_I
\end{array}
\right]
:
\left\{
\begin{array}{c}
d\mathbf{E}^d - d\mathbf{e}^p_M \\
d\mathbf{E}^d - d\mathbf{e}^p_F
\end{array}
\right\}
\qquad (2.14)
$$

where $d\mathbf{E}^d = d\mathbf{E} - dE^v \mathbf{1}$, $d\mathbf{e}^p_M = d\varepsilon^p_M - d\epsilon^p_M \mathbf{1}$ and $d\mathbf{e}^p_F = d\varepsilon^p_F - d\epsilon^p_F \mathbf{1}$ are deviatoric strain increments.

In a randomly oriented fiber system, there are six composite elastic properties to be determined. Four of them $(G_M, G_F, \nu_M$ and $\nu_F)$ are associated with the elasticity of the matrix and the fiber, and they are parameters that relate to the *elastic* composite matrix behavior. However, two of them $(M^{3D}$ and $\nu_I)$ are associated with the elasticity of the matrix-fiber coupling, and they are the constants related to the *irreversible* composite matrix behavior, i.e. post-cracking behavior. Thus, it is first necessary to consider the strength domain and post-cracking plasticity behavior of the model in order to obtain meaningful expressions for M^{3D} and ν_I.
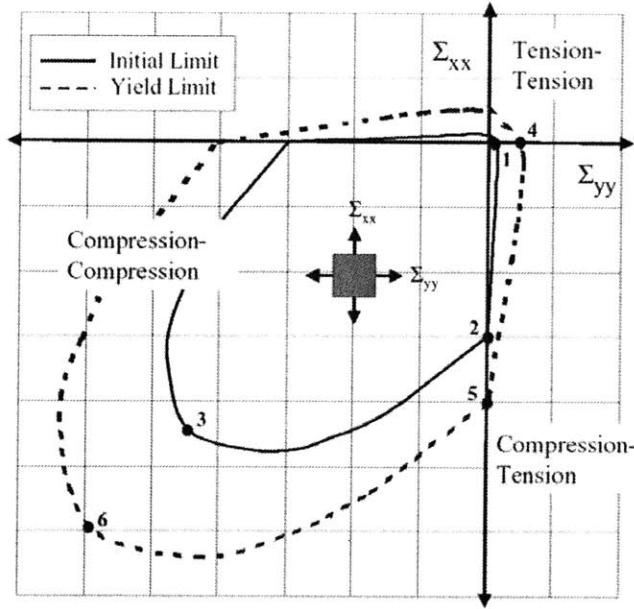
Figure 2-4: UHPC strength domain in the $\Sigma_{xx} \times \Sigma_{yy}$ plane ($\Sigma_{zz} = 0$) [7].

2.3.2 Plasticity of the 3-D Model

The 3-D Strength Domain

The UHPC strength domain is characterized by two different strength limits, an initial limit and a yield limit. This triaxial strength domain can be captured by 6 macroscopic strength values, as shown in Figure 2-4, represented by the following: (1) initial tensile strength, $\Sigma_{t,1}^-$; (2) initial compressive strength, $\Sigma_{c,1}^-$; (3) initial biaxial compressive strength, $\Sigma_{b,1}^-$; (4) tensile yield strength, $\Sigma_{t,2}$; (5) compressive yield strength, $\Sigma_{c,2}$; (6) biaxial compressive yield strength, $\Sigma_{b,2}$.

From a modeling point of view, the strength domain $\mathcal{D}_E$ of UHPC, which is described by the 3-D loading function F, is governed by the individual behaviors of the composite matrix and the composite fiber:

$$\Sigma \in \mathcal{D}_E \quad \Leftrightarrow \quad F = \max\left[F_M,\, F_F\right] \leq 0 \quad \Leftrightarrow \quad \left\langle \begin{array}{ccc} \sigma_M \in \mathcal{D}_M & \Leftrightarrow & F_M\left(\sigma_M\right) \leq 0 \\ \sigma_F \in \mathcal{D}_F & \Leftrightarrow & F_F\left(\sigma_F\right) \leq 0 \end{array} \right\rangle \quad (2.15)$$

where $\mathcal{D}_M$ and $\mathcal{D}_F$ are the strength domains of the matrix and the fiber; F_M and F_F are the
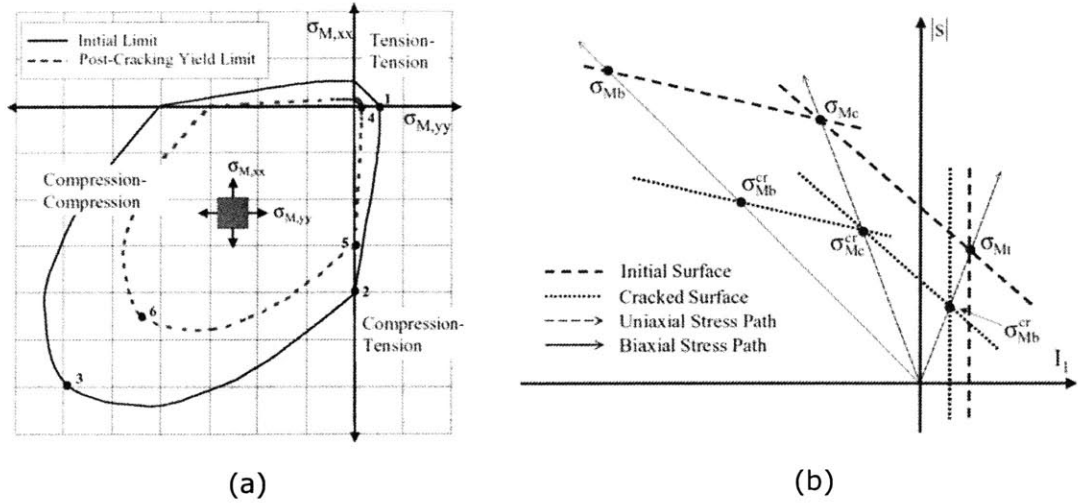
Figure 2-5: (a) Composite matrix strength domain in the $\sigma_{M,xx} \times \sigma_{M,yy}$ plane ($\sigma_{M,zz} = 0$), (b) Loading function of the composite matrix before and after cracking [7].

3-D loading function of the matrix and the fiber, respectively.

The composite matrix strength domain The elasto-brittle-plastic behavior of the matrix phase is captured by the matrix strength domain with a higher initial limit and a lower yield limit. This strength domain is depicted by 6 characteristic values shown in Figure 2-5 (a):

1. The initial tensile strength, σ_{Mt}. This is the same as the matrix cracking strength of the 1-D UHPC model, $\sigma_{Mt} = f_t + k_M$.

2. The initial compressive strength, σ_{Mc}.

3. The initial biaxial compressive strength, σ_{Mb}.

4. The tensile post-cracking yield strength, σ_{Mt}^{cr}. This is equivalent to the matrix post-cracking strength of the 1-D UHPC model, $\sigma_{Mt}^{cr} = k_M$.

5. The compressive yield strength, σ_{Mc}^{cr}.

6. The biaxial compressive yield strength, σ_{Mb}^{cr}.

Before matrix cracking, the initial strength parameters govern the loading function of the composite matrix. To describe these initial strength limits, a tension cut-off [TC] criterion is

considered to capture the tension-tension stress states $\left(f_M^{TC,0}\right)$; a Drucker-Prager [DP] criterion is considered for the compression-tension stress states $\left(f_M^{UN,0}\right)$; and another DP criterion is considered for the compression-compression stress states $\left(f_M^{BI,0}\right)$. The initial loading functions read:

$$f_M^{TC,0} = I_{1,M} - \sigma_{Mt} \leq 0$$
$$f_M^{UN,0} = \alpha_M^{UN} I_{1,M} + |\mathbf{s}_M| - c_M^{UN,0} \leq 0 \qquad (2.16)$$
$$f_M^{BI,0} = \alpha_M^{BI} I_{1,M} + |\mathbf{s}_M| - c_M^{BI,0} \leq 0$$

where

$$I_{1,M} = tr\boldsymbol{\sigma}_M \qquad (2.17)$$

$$\alpha_M^{UN} = \frac{\sqrt{2/3}(\sigma_{Mc}-\sigma_{Mc})}{\sigma_{Mc}+\sigma_{Mc}}; \quad c_M^{UN,0} = \left(\sqrt{\frac{2}{3}} - \sigma_M^{UN}\right)\sigma_{Mc};$$
$$\alpha_M^{BI} = \frac{\sqrt{2/3}(\sigma_{Mb}-\sigma_{Mc})}{2\sigma_{Mb}-\sigma_{Mc}}; \quad c_M^{BI,0} = \left(\sqrt{\frac{2}{3}} - \sigma_M^{BI}\right)\sigma_{Mc} \qquad (2.18)$$

After cracking, the post-cracking strength parameters govern the loading function of the composite matrix. In order to reduce modeling parameters, it is assumed that the post-cracking composite strengths are reduced by the same factor:

$$\gamma^{cr} = \frac{\sigma_{Mt}^{cr}}{\sigma_{Mt}} = \frac{\sigma_{Mc}^{cr}}{\sigma_{Mc}} = \frac{\sigma_{Mb}^{cr}}{\sigma_{Mb}} \qquad (2.19)$$

where the superscript "cr" denotes a cracked state. Now, the post-cracking loading functions read:

$$f_M^{TC,cr} = I_{1,M} - \sigma_{Mt}^{cr} \leq 0$$
$$f_M^{UN,cr} = \alpha_M^{UN} I_{1,M} + |\mathbf{s}_M| - c_M^{UN,cr} \leq 0 \qquad (2.20)$$
$$f_M^{BI,cr} = \alpha_M^{BI} I_{1,M} + |\mathbf{s}_M| - c_M^{BI,cr} \leq 0$$

where

$$c_M^{UN,cr} = \gamma^{cr} c_M^{UN,0} \; ; \quad c_M^{BI,cr} = \gamma^{cr} c_M^{BI,0} \qquad (2.21)$$

These loading functions are illustrated in Figure 2-5 (b) in the $I_1 - |\mathbf{s}|$ plane. In summary, we can describe the strength domain of the composite matrix as follows:

$$\boldsymbol{\sigma}_M \in \mathcal{D}_M \quad \Leftrightarrow \quad F_M\left(\boldsymbol{\sigma}_M\right) = \left\langle \begin{array}{ll} F_M^0 = \max\left[f_M^{TC,0}, \; f_M^{UN,0}, \; f_M^{BI,0}\right] & \text{before cracking} \\ F_M^{cr} = \max\left[f_M^{TC,cr}, \; f_M^{UN,cr}, \; f_M^{BI,cr}\right] & \text{after cracking} \end{array} \right\rangle \leq 0$$
$$(2.22)$$
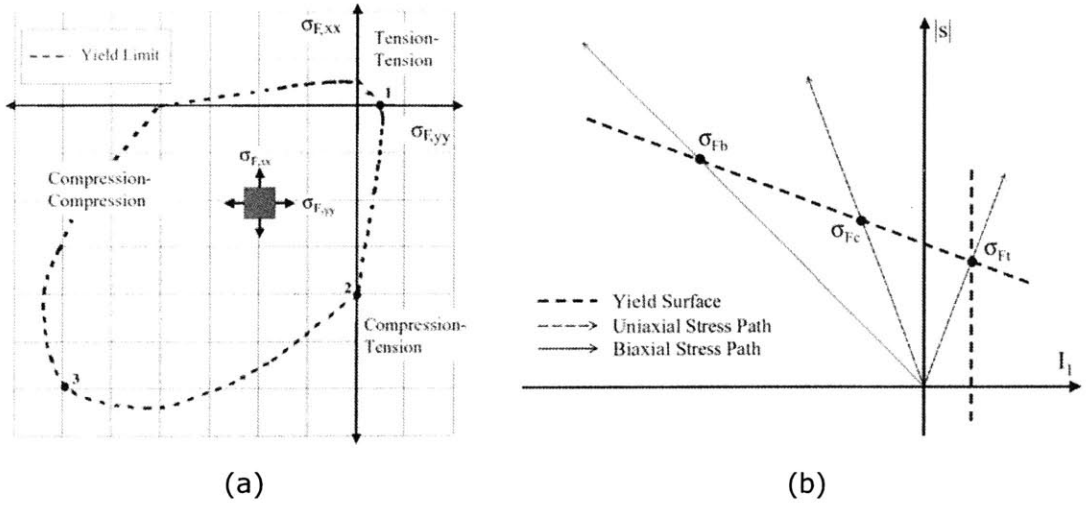
Figure 2-6: (a) Composite fiber strength domain in the $\sigma_{F,xx} \times \sigma_{F,yy}$ plane ($\sigma_{F,zz} = 0$), (b) Loading function of the composite fiber before and after cracking [7].

The composite fiber strength domain Second, an elasto-plastic behavior of the composite fiber phase is captured by three characteristic values shown in Figure 2-6 (a):

1. The tensile strength, σ_{Ft}. This is the same as the fiber strength of the 1-D UHPC model, $\sigma_{Ft} = f_y$.

2. The compressive strength, σ_{Fc}.

3. The biaxial compressive strength, σ_{Fb}.

Like the elastic spring of the composite fiber in the 1-D UHPC model, the characteristic compressive strengths of the composite fiber are not the compressive strengths of the reinforcing fiber but the compressive *contributions* added to the overall UHPC composite strength as a result of reinforcing fibers. As a simplifying assumption, one single criterion is not specifically designated to limit the composite fiber's biaxial compressive strength, σ_{Fb}. Thus, to describe the strength limits, a TC criterion is chosen for the tension-tension stress states $\left(f_F^{TC}\right)$ and a DP criterion governs the compression-tension stress states $\left(f_F^{DP}\right)$:

$$f_F^{TC} = I_{1,F} - \sigma_{Ft} \leq 0$$
$$f_F^{DP} = \alpha_F^{UN} I_{1,F} + |\mathbf{s}_F| - c_F^{DP} \leq 0$$

(2.23)

where

$$I_{1,F} = tr\boldsymbol{\sigma}_F \tag{2.24}$$

$$\alpha_F^{DP} = \frac{\sqrt{2/3}(\sigma_{Fc} - \sigma_{Fc})}{\sigma_{Fc} + \sigma_{Fc}}; \quad c_F^{DP} = \left(\sqrt{2/3} - \sigma_F^{DP}\right)\sigma_{Fc}; \tag{2.25}$$

With these relations, we can describe the strength domain of the composite fiber as follows:

$$\boldsymbol{\sigma}_F \in \mathcal{D}_F \quad \Leftrightarrow \quad F_F(\boldsymbol{\sigma}_F) = \max\left[f_F^{TC}, \ f_F^{DP}\right] \leq 0 \tag{2.26}$$

Plastic Flow Rule

The composite matrix and composite fiber are both governed by the following Kuhn-Tucker conditions:

$$F_M(\boldsymbol{\sigma}_M) \leq 0; \quad d\lambda_M \geq 0; \quad F_M(\boldsymbol{\sigma}_M)\,d\lambda_M = 0 \tag{2.27}$$

$$F_F(\boldsymbol{\sigma}_F) \leq 0; \quad d\lambda_F \geq 0; \quad F_F(\boldsymbol{\sigma}_F)\,d\lambda_F = 0 \tag{2.28}$$

where $d\lambda_M$ and $d\lambda_F$ are the plastic multipliers that represent the intensity of the plastic yielding in the composite matrix and the composite fiber, respectively. In this study, an associated plastic flow rule is adopted, so that plastic deformations occurs in the normal direction to the loading function ($\frac{\partial F_M}{\partial \boldsymbol{\sigma}_M}$ and $\frac{\partial F_F}{\partial \boldsymbol{\sigma}_F}$). Since the two types of loading function (TC and DP) are used to describe the plasticity of the early-age UHPC, the direction of the plastic flow for each loading function now reads:

$$\frac{\partial f^{TC}(\boldsymbol{\sigma})}{\partial \boldsymbol{\sigma}} = \mathbf{1}; \quad \frac{\partial f^{DP}(\boldsymbol{\sigma})}{\partial \boldsymbol{\sigma}} = \alpha\mathbf{1} + \mathbf{N_s} \tag{2.29}$$

where $\mathbf{N_s} = \frac{\mathbf{s}}{|\mathbf{s}|}$ is the normalized deviatoric stress tensor. Now, the permanent deformations of the composite matrix and the composite fiber read:

$$
\begin{aligned}
d\boldsymbol{\varepsilon}_M^p &= \sum_i d\lambda_{M,i} \frac{\partial F_{M,i}(\boldsymbol{\sigma}_M, \xi)}{\partial \boldsymbol{\sigma}_M} \\
&= d\lambda_M^{TC} \frac{\partial f_M^{TC}}{\partial \boldsymbol{\sigma}_M} + d\lambda_M^{UN} \frac{\partial f_M^{UN}}{\partial \boldsymbol{\sigma}_M} + d\lambda_M^{BI} \frac{\partial f_M^{BI}}{\partial \boldsymbol{\sigma}_M} \\
&= d\lambda_M^{TC}\mathbf{1} + d\lambda_M^{UN}\left[\alpha_M^{UN}\mathbf{1} + \mathbf{N_{s_M}}\right] + d\lambda_M^{BI}\left[\alpha_M^{BI}\mathbf{1} + \mathbf{N_{s_M}}\right]
\end{aligned} \tag{2.30}
$$

33

	Before Matrix Cracking	After Matrix Cracking
$f_M^{TC} =$	$f_M^{TC,0}$	$f_M^{TC,cr}$
$f_M^{UN} =$	$f_M^{UN,0}$	$f_M^{UN,cr}$
$f_M^{BI} =$	$f_M^{BI,0}$	$f_M^{BI,cr}$

Table 2.1: Loading functions for the composite matrix depending on the cracking condition of the composite matrix.

$$
\begin{aligned}
d\varepsilon_F^p &= \sum_i d\lambda_{F,i} \frac{\partial F_{F,i}(\boldsymbol{\sigma}_F, \xi)}{\partial \boldsymbol{\sigma}_F} \\
&= d\lambda_F^{TC} \frac{\partial f_F^{TC}}{\partial \boldsymbol{\sigma}_M} + d\lambda_F^{DP} \frac{\partial f_F^{DP}}{\partial \boldsymbol{\sigma}_M} \\
&= d\lambda_F^{TC} \mathbf{1} + d\lambda_F^{DP} \left[\alpha_F^{UN} \mathbf{1} + \mathbf{N}_{\mathbf{s}_F} \right]
\end{aligned}
\tag{2.31}
$$

where the loading functions of the composite matrix are defined in Table 2.1; and $\mathbf{N}_{\mathbf{s}_M} = \frac{\mathbf{s}_M}{|\mathbf{s}_M|}$ and $\mathbf{N}_{\mathbf{s}_F} = \frac{\mathbf{s}_F}{|\mathbf{s}_F|}$ is the normalized deviatoric stress tensor of the composite matrix and the composite fiber, respectively.

Due to the intrinsic characteristics of the TC and DP, the loading criteria for 3-D UHPC model defines the following dilatation behavior in plastic deformation:

$$
\begin{aligned}
tr(d\boldsymbol{\varepsilon}^p) &= tr\left(\sum_i d\lambda_i \frac{\partial F_i(\boldsymbol{\sigma})}{\partial \boldsymbol{\sigma}} \right) \\
&= tr\left(\sum_j d\lambda_j^{TC} \frac{\partial f_j^{TC}(\boldsymbol{\sigma})}{\partial \boldsymbol{\sigma}} + \sum_k d\lambda_k^{DP} \frac{\partial f_k^{DP}(\boldsymbol{\sigma})}{\partial \boldsymbol{\sigma}} \right) \\
&= \sum_j 3 d\lambda_j^{TC} + \sum_k 3\alpha d\lambda_k^{DP}
\end{aligned}
\tag{2.32}
$$

where j and k are the numbers of TC loading function and DP loading function employed for each composite phase, respectively. This plastic dilatation behavior does not allow to capture crack closure in the composite matrix.

2.3.3 Consistency with the 1-D Model

Unlike the elastic properties of the composite matrix and the composite fiber, the properties of the matrix-fiber coupling (M^{3D} and ν_I) are not directly related to the 1-D model parameters. The strength domain needs to be considered to obtain meaningful coupling properties in order

for the 3-D model to generate the same uniaxial response as the 1-D model. The uniaxial loading for the 3-D model requires the following conditions:

- A loading strain is applied in one direction (x-direction) and there are no shear strains:

$$
\begin{aligned}
E_{xx} &\neq 0; \\
E_{yy} &= E_{zz} \neq 0; \\
E_{xy} &= E_{yz} = E_{zx} = 0
\end{aligned}
\tag{2.33}
$$

- The loading strain produces the corresponding stresses:

$$
\begin{aligned}
\Sigma_{xx} &= \Sigma_{xx}\left(E_{xx}\right); \\
\Sigma_{yy} &= \Sigma_{zz} = 0; \\
\Sigma_{xy} &= \Sigma_{yz} = \Sigma_{zx} = 0
\end{aligned}
\tag{2.34}
$$

- The 3-D loading function defined by (2.15) must be obeyed:

$$
F = \max\left[F_M,\ F_F\right] \leq 0
\tag{2.35}
$$

When loading functions are activated, plastic strains occur through the plastic multipliers, i.e. $d\lambda_M^{TC}$, $d\lambda_M^{UN}$, $d\lambda_M^{BI}$, $d\lambda_F^{TC}$ and $d\lambda_F^{DP}$.

Stress-Strain Curve of the 3-D Model

During the first cracking under uniaxial loading, cracking occurs in all directions including transverse cracks perpendicular to the load direction and randomly oriented fiber debonding cracks. The reinforcing fibers restrict the opening of cracks in the composite matrix. Due to the intrinsic characteristics of the Tension-Cut Off and the Drucker-Prager loading functions, the macroscopic UHPC model represents these cracks as dilating plastic strains in the composite matrix, see relation (2.32). Figure 2-7 shows the stress evolution of the composite matrix and composite fiber during uniaxial loading as predicted by the 3-D hardened UHPC model. While the stress-strain curve in the 1-D model shows only one post-cracking stiffness (K_1), the 3-D model shows two different post-cracking stiffnesses (K_1^{3D} and K_{2A}^{3D}) after the first cracking in

35
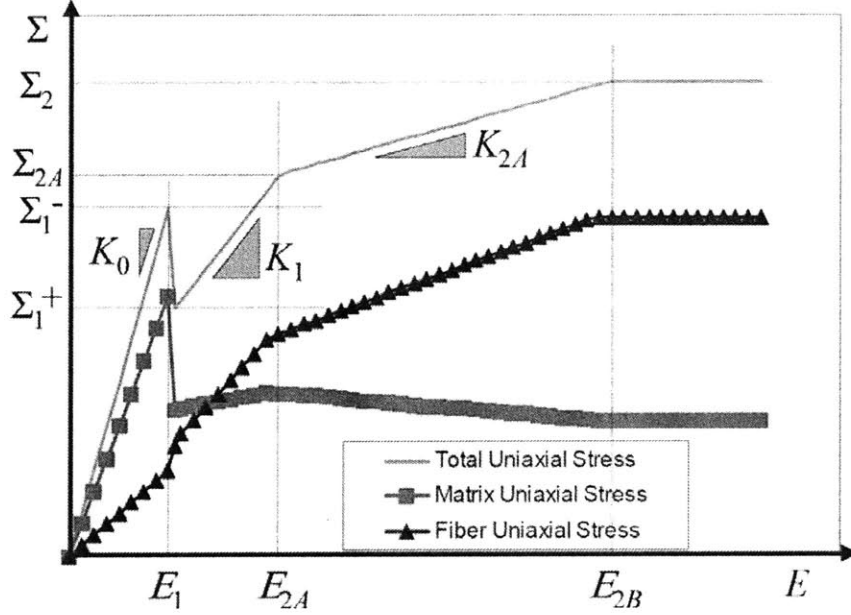
Figure 2-7: Evolution of composite matrix and composite fiber stresses given by the uniaxial output from the 3-D hardened UHPC model (in this graph, the subscripts "xx" are omitted for simplicity) [7].

matrix. The second post-cracking behavior of slope K_{2A}^{3D} was called "*kinking*" by Chuang [7]. In order to accomplish the consistency of the 3-D model with the 1-D model, we need to first obtain analytically the stress-strain behavior of the 3-D model, i.e. the $E_{xx} - \Sigma_{xx}$ curve. There are four points and three stiffnesses to be identified:

$$\left(E_{xx,1},\ \Sigma_{xx,1}^{-}\right);\quad \left(E_{xx,1},\ \Sigma_{xx,1}^{+}\right);$$
$$\left(E_{xx,2A},\ \Sigma_{xx,2A}\right);\quad \left(E_{xx,2B},\ \Sigma_{xx,2}\right) \tag{2.36}$$

$$K_0^{3D};\quad K_1^{3D};\quad K_{2A}^{3D} \tag{2.37}$$

Stress-Strain Points Before the first cracking in the composite matrix ($0 \leq E_{xx} < E_{xx,1}$), the 3-D model shows elastic behavior. The first noteworthy point in the stress-strain curve is when the macroscopic stress meets the initial tensile strength, $\Sigma_{xx} = \sigma_{Mt}$. At this point,

there are two unknowns (E_{xx} and E_{yy}) and two equations ($\Sigma_{xx} = \sigma_{Mt}$ and $\Sigma_{yy} = 0$). Thus, the unknown macroscopic strains can be obtained from the following equations:

$$\left\{ \begin{array}{c} E_{xx} \\ E_{yy} \end{array} \right\} = [\mathcal{J}_1]^{-1} \left\{ \begin{array}{c} \sigma_{Mt} \\ 0 \end{array} \right\} \tag{2.38}$$

where:

$$[\mathcal{J}_1] = \begin{bmatrix} \left\langle \begin{array}{c} (K_M + K_F) \\ +\frac{4}{3}(G_M + G_F) \end{array} \right\rangle & \left\langle \begin{array}{c} 2(K_M + K_F) \\ -\frac{4}{3}(G_M + G_F) \end{array} \right\rangle \\ \left\langle \begin{array}{c} (K_M + K_F) \\ -\frac{2}{3}(G_M + G_F) \end{array} \right\rangle & \left\langle \begin{array}{c} 2(K_M + K_F) \\ +\frac{2}{3}(G_M + G_F) \end{array} \right\rangle \end{bmatrix} \tag{2.39}$$

Solving (2.38) yields the macroscopic strain and the macroscopic stress:

$$\left(E_{xx,1},\ \Sigma_{xx,1}^{-} \right) = (E_{xx},\ \Sigma_{xx})|_{\Sigma_{xx}=\sigma_{Mt},\ \Sigma_{yy}=0} \tag{2.40}$$

Moreover, right after the first cracking at the macroscopic strain E_1, the abrupt stress drop leads to the post-cracking tensile strength $\Sigma_{xx} = \sigma_{Mt}^{cr}$. This second point is denoted by:

$$\left(E_{xx,1},\ \Sigma_{xx,1}^{+} \right) = \left(E_{xx}|_{\Sigma_{xx}=\sigma_{Mt},\ \Sigma_{yy}=0},\ \Sigma_{xx}|_{\Sigma_{xx}=\sigma_{Mt}^{cr}} \right) \tag{2.41}$$

The kinking behavior of the 3-D model occurs in the macroscopic strain range $E_{xx,1} \leq E_{xx} < E_{xx,2A}$. At the third point, we have three unknowns (E_{xx}, E_{yy} and λ_M^{UN}) and three equations ($\Sigma_{yy} = 0$, $f_M^{UN,cr} = 0$ and $f_F^{TC} = 0$). The unknown quantities can be solved from:

$$\left\{ \begin{array}{c} E_{xx} \\ E_{yy} \\ \lambda_M^{UN} \end{array} \right\} = [\mathcal{J}_2]^{-1} \left\{ \begin{array}{c} 0 \\ c_M^{UN,cr} \\ \sigma_{Ft} \end{array} \right\} \tag{2.42}$$

37

where:

$$[\mathcal{J}_2] = \begin{bmatrix} \left\langle \begin{array}{c} (K_M + K_F) \\ -\frac{2}{3}(G_M + G_F) \end{array} \right\rangle & \left\langle \begin{array}{c} 2(K_M + K_F) \\ +\frac{2}{3}(G_M + G_F) \end{array} \right\rangle & -3\alpha_M^{UN} K_M + \sqrt{\frac{2}{3}} G_M \\ 3\alpha_M^{UN} K_M + \sqrt{\frac{8}{3}} G_M & 6\alpha_M^{UN} K_M - \sqrt{\frac{8}{3}} G_M & \left\langle \begin{array}{c} -9\left(\alpha_M^{UN}\right)^2 (K_M + K_F) \\ -2(G_M + G_F) \end{array} \right\rangle \\ 3K_F & 6K_F & 9\alpha_M^{UN} K_I \end{bmatrix}$$

$$(2.43)$$

Furthermore, the corresponding macroscopic stress reads:

$$\Sigma_{xx} = \left\{ \begin{array}{c} (K_M + K_F) + \frac{4}{3}(G_M + G_F) \\ 2(K_M + K_F) - \frac{4}{3}(G_M + G_F) \\ -3\alpha_M^{UN} K_M - \sqrt{\frac{8}{3}} G_M \end{array} \right\}^T \left\{ \begin{array}{c} E_{xx} \\ E_{yy} \\ \lambda_M^{UN} \end{array} \right\} \qquad (2.44)$$

leading to the third stress-strain point:

$$(E_{xx,2A}, \ \Sigma_{xx,2A}) = (E_{xx}, \ \Sigma_{xx})|_{\Sigma_{yy}=0, \ f_M^{UN,cr}=0, \ f_F^{TC}=0} \qquad (2.45)$$

At the fourth point, both the composite matrix and the composite fiber are at yield, and there are four unknowns (E_{xx}, E_{yy}, λ_M^{UN} and λ_F^{TC}) and four equations ($\Sigma_{yy} = 0$, $f_M^{TC,cr} = 0$, $f_M^{UN,cr} = 0$ and $f_F^{TC} = 0$). We obtain the unknown quantities from:

$$\left\{ \begin{array}{c} E_{xx} \\ E_{yy} \\ \lambda_M^{UN} \\ \lambda_F^{TC} \end{array} \right\} = [\mathcal{J}_3]^{-1} \left\{ \begin{array}{c} 0 \\ \sigma_{Mt}^{cr} \\ c_M^{UN,cr} \\ \sigma_{Ft} \end{array} \right\} \qquad (2.46)$$

where

$$[\mathcal{J}_3] = \begin{bmatrix} \left\langle \begin{array}{c} (K_M+K_F) \\ -\frac{2}{3}(G_M+G_F) \end{array} \right\rangle & \left\langle \begin{array}{c} 2(K_M+K_F) \\ +\frac{2}{3}(G_M+G_F) \end{array} \right\rangle & -3\alpha_M^{UN}K_M+\sqrt{\frac{2}{3}}G_M & -3K_F \\[3mm] 3K_M & 6K_M & -9\alpha_M^{UN}(K_M+K_I) & -9K_I \\[3mm] 3\alpha_M^{UN}K_M+\sqrt{\frac{8}{3}}G_M & 6\alpha_M^{UN}K_M-\sqrt{\frac{8}{3}}G_M & \left\langle \begin{array}{c} -9\left(\alpha_M^{UN}\right)^2(K_M+K_F) \\ -2(G_M+G_F) \end{array} \right\rangle & -9\alpha_M^{UN}K_I \\[3mm] 3K_F & 6K_F & 9\alpha_M^{UN}K_I & -9(K_F+K_I) \end{bmatrix} \qquad (2.47)$$

The corresponding macroscopic stress reads:

$$\Sigma_{xx} = \left\{ \begin{array}{c} (K_M+K_F)+\frac{4}{3}(G_M+G_F) \\ 2(K_M+K_F)-\frac{4}{3}(G_M+G_F) \\ -3\alpha_M^{UN}K_M-\sqrt{\frac{8}{3}}G_M \\ -3K_F \end{array} \right\}^T \left\{ \begin{array}{c} E_{xx} \\ E_{yy} \\ \lambda_M^{UN} \\ \lambda_F^{TC} \end{array} \right\} = \sigma_{Mt}^{cr} + \sigma_{Ft} \qquad (2.48)$$

This last point in the stress-strain curve is denoted by:

$$\begin{aligned} (E_{xx,2B}, \ \Sigma_{xx,2}) &= (E_{xx}, \ \Sigma_{xx})|_{\Sigma_{yy}=0, \ f_M^{TC,cr}=0,} \qquad\qquad\qquad\qquad (2.49) \\ & \hspace{3cm} {}_{f_M^{UN,cr}=0, \ f_F^{TC}=0} \\[3mm] &= \left(E_{xx}|_{\substack{\Sigma_{yy}=0, \ f_M^{TC,cr}=0, \\ f_M^{UN,cr}=0, \ f_F^{TC}=0}}, \ \ \Sigma_{xx}|_{\Sigma_{xx}=\sigma_{Mt}^{cr}+\sigma_{Ft}} \right) \end{aligned}$$

Stiffnesses Next, the three stiffnesses are solved analytically. The initial stiffness K_0, which controls the elastic behavior of the material over the macroscopic region $0 \leq E_{xx} < E_{xx,1}$, reads:

$$\begin{aligned} K_0^{3D} &= \left. \frac{\partial \Sigma_{xx}}{\partial E_{xx}} \right|_{\Sigma_{yy}=0} \qquad\qquad\qquad\qquad\qquad (2.50) \\[3mm] &= \left\{ \begin{array}{c} (K_M+K_F)+\frac{4}{3}(G_M+G_F) \\ 2(K_M+K_F)-\frac{4}{3}(G_M+G_F) \end{array} \right\}^T \left\{ \begin{array}{c} 1 \\ \frac{\partial E_{yy}}{\partial E_{xx}} \end{array} \right\} \end{aligned}$$

where

$$\frac{\partial E_{yy}}{\partial E_{xx}} = \frac{-\left(K_M + K_F\right) + \frac{2}{3}\left(G_M + G_F\right)}{2\left(K_M + K_F\right) + \frac{2}{3}\left(G_M + G_F\right)} \tag{2.51}$$

The first post-cracking stiffness which controls the plastic behavior before the kinking $(E_{xx,1} \le E_{xx} < E_{xx,2A})$ reads:

$$
\begin{aligned}
K_1^{3D} &= \left.\frac{\partial \Sigma_{xx}}{\partial E_{xx}}\right|_{\Sigma_{yy}=0,\ f_M^{UN}=0} \\[2mm]
&= \left\{ \begin{array}{c} \left(K_M + K_F\right) + \frac{4}{3}\left(G_M + G_F\right) \\ 2\left(K_M + K_F\right) - \frac{4}{3}\left(G_M + G_F\right) \\ -3\alpha_M^{UN} K_M - \sqrt{\frac{8}{3}} G_M \end{array} \right\}^T \left\{ \begin{array}{c} 1 \\ \frac{\partial E_{yy}}{\partial E_{xx}} \\ \frac{\partial \lambda_M^{UN}}{\partial E_{xx}} \end{array} \right\}
\end{aligned} \tag{2.52}
$$

where

$$\left\{ \begin{array}{c} \frac{\partial E_{yy}}{\partial E_{xx}} \\ \frac{\partial \lambda_M^{UN}}{\partial E_{xx}} \end{array} \right\} = [\mathcal{M}_1]^{-1} \left\{ \begin{array}{c} -\left(K_M + K_F\right) + \frac{2}{3}\left(G_M + G_F\right) \\ -3\alpha_M^{UN} K_M - \sqrt{\frac{8}{3}} G_M \end{array} \right\} \tag{2.53}$$

$$[\mathcal{M}_1] = \left[\begin{array}{cc} \left\langle \begin{array}{c} 2\left(K_M + K_F\right) \\ +\frac{2}{3}\left(G_M + G_F\right) \end{array} \right\rangle & -3\alpha_M^{UN} K_M + \sqrt{\frac{2}{3}} G_M \\[4mm] 6\alpha_M^{UN} K_M - \sqrt{\frac{8}{3}} G_M & \left\langle \begin{array}{c} -9\left(\alpha_M^{UN}\right)^2\left(K_M + K_F\right) \\ -2\left(G_M + G_F\right) \end{array} \right\rangle \end{array} \right] \tag{2.54}$$

The second post-cracking stiffness which relates to the kinking behavior of the material $(E_{xx,2A} \le E_{xx} < E_{xx,2B})$ reads:

$$
\begin{aligned}
K_{2A}^{3D} &= \left.\frac{\partial \Sigma_{xx}}{\partial E_{xx}}\right|_{\Sigma_{yy}=0,\ f_M^{UN}=0,\ f_F^{TC}=0} \\[2mm]
&= \left\{ \begin{array}{c} \left(K_M + K_F\right) + \frac{4}{3}\left(G_M + G_F\right) \\ 2\left(K_M + K_F\right) - \frac{4}{3}\left(G_M + G_F\right) \\ -3\alpha_M^{UN} K_M - \sqrt{\frac{8}{3}} G_M \\ -3K_F \end{array} \right\}^T \left\{ \begin{array}{c} 1 \\ \frac{\partial E_{yy}}{\partial E_{xx}} \\ \frac{\partial \lambda_M^{UN}}{\partial E_{xx}} \\ \frac{\partial \lambda_F^{TC}}{\partial E_{xx}} \end{array} \right\}
\end{aligned} \tag{2.55}
$$

40

where

$$\left\{ \begin{array}{c} \frac{\partial E_{yy}}{\partial E_{xx}} \\ \frac{\partial \lambda_M^{UN}}{\partial E_{xx}} \\ \frac{\partial \lambda_F^{TC}}{\partial E_{xx}} \end{array} \right\} = [\mathcal{M}_2]^{-1} \left\{ \begin{array}{c} -(K_M + K_F) + \frac{2}{3}(G_M + G_F) \\ -3\alpha_M^{UN} K_M - \sqrt{\frac{8}{3}} G_M \\ -3K_F \end{array} \right\} \tag{2.56}$$

$$[\mathcal{M}_2] = \begin{bmatrix} \left\langle \begin{array}{c} 2(K_M + K_F) \\ +\frac{2}{3}(G_M + G_F) \end{array} \right\rangle & -3\alpha_M^{UN} K_M + \sqrt{\frac{2}{3}} G_M & -3K_F \\[2ex] 6\alpha_M^{UN} K_M - \sqrt{\frac{8}{3}} G_M & \left\langle \begin{array}{c} -9\left(\alpha_M^{UN}\right)^2 (K_M + K_F) \\ -2(G_M + G_F) \end{array} \right\rangle & -9\alpha_M^{UN} K_I \\[2ex] 6K_F & 9\alpha_M^{UN} K_I & -9(K_F + K_I) \end{bmatrix} \tag{2.57}$$

For uniaxial loading, the stress-strain curve can be constructed analytically using the stress-strain points and stiffnesses just derived.

Determination of the 3-D Coupling Modulus

In order for the 3-D model results to be consistent with the 1-D model results, the following conditions need to be satisfied:

- The four stress-strain points determined here before must be on the stress-strain curve of the 1-D hardened UHPC model:

$$\begin{array}{l} \left(E_{xx,1}, \ \Sigma_{xx,1}^-\right) = \left(E_1, \ \Sigma_1^-\right); \\[1ex] \left(E_{xx,1}, \ \Sigma_{xx,1}^+\right) = \left(E_1, \ \Sigma_1^+\right) \end{array} \tag{2.58}$$

$$\left. \begin{array}{l} (E_{xx,2A}, \ \Sigma_{xx,2A}) \\[1ex] (E_{xx,2B}, \ \Sigma_{xx,2}) \end{array} \right\} \in \ (E, \Sigma) \ \text{of 1-D model} \tag{2.59}$$

- Except for the kinking region, the initial stiffness and the first cracking stiffness of the 3-D model must coincide with those of the 1-D model:

$$K_0^{3D} = K_0 \tag{2.60}$$

$$K_1^{3D} = K_1 \tag{2.61}$$
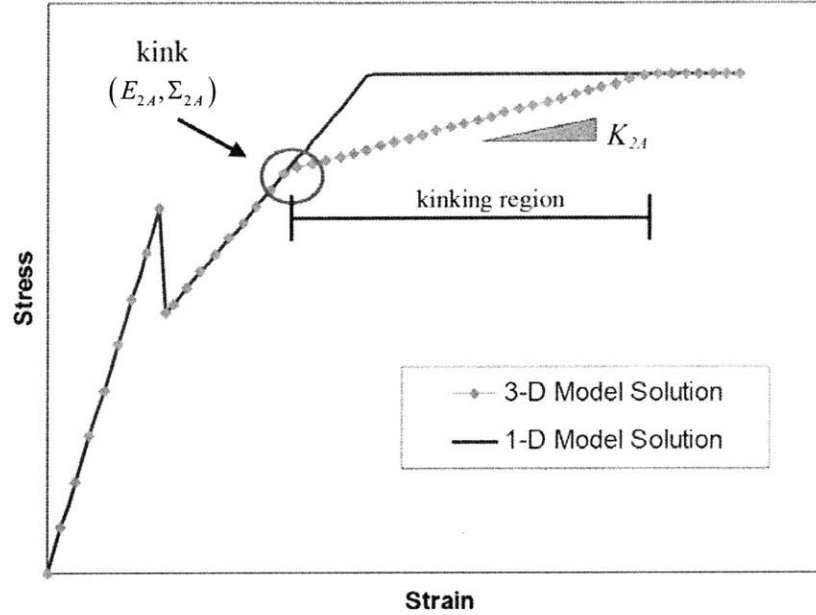
Figure 2-8: Comparison of the 1-D and 3-D model output for uniaxial tensile loading [7].

Since the quantities in (2.58) and (2.60) relate only to the elastic properties, the results of the 3-D model naturally coincide with those of the 1-D model. However, in the plastic region, we need to tune the 3-D model results to the 1-D model results. This tuning is achieved by solving (2.61) in order to obtain the 3-D coupling modulus M^{3D}. By substituting (2.52) and (2.1) into (2.61) and assuming that the Poisson's ratios of the different phases are equal ($\nu_M = \nu_F = \nu_I = \nu$), Chuang derived the following expression [7]:

$$M^{3D} = \beta M + (\beta - 1) \frac{C_M C_F}{C_M + C_F} \tag{2.62}$$

where

$$\beta = \frac{\left(\alpha_M^{UN} + \sqrt{2/3}\right)^2 (1 - \nu)(1 + \nu)}{3\left(\alpha_M^{UN}\right)^2 (1 + \nu) + (1 - 2\nu)} \tag{2.63}$$

Figure 2-8 compares the uniaxial stress-strain output from the 1-D and the 3-D model.

The 3-D UHPC material model was implemented in a commercial finite element program, CESAR-LCPC, which makes it possible to simulate the nonlinear response of UHPC structures. Furthermore, the model was validated for 2-D and 3-D structures [7] [18].

2.4 Determination of Hardened Model Parameters

The two-phase UHPC model captures the overall composite behavior, at the macroscopic scale, with a brittle-plastic matrix phase and an elasto-plastic fiber phase. Here, each phase is considered as a *macroscopic representation* of the stiffness and the yield strength that are added to obtain the stiffness and the strength of the overall UHPC composite. Due to the macroscopic nature of the material model, all 3-D model parameters can be determined from the macroscopic response of a UHPC material. The determination procedure of the model parameters is achieved in the following way:

- Macroscopic material properties: The results of a tensile test and a compressive test are used to identify the macroscopic stress-strain points of the idealized macroscopic stress-strain response.

- Assumptions for the 3-D model parameters: Three simplifying assumptions are introduced to reduce the number of model parameters of the isotropic UHPC material behavior.

- Determination of the 3-D model parameters: The 10 independent 3-D model parameters are determined from the macroscopic stress-strain points.

2.4.1 Macroscopic Material Properties

UHPC materials can vary with the type of fibers a supplier chooses to use. The manufacturer of Ductal^{TM} (Lafarge) produces two types of UHPC material: one is Ductal^{TM}-Steel Fiber, and the other Ductal^{TM}-Organic Fiber. Ductal^{TM}-Steel Fiber was used in the test girders of the Federal Highway Administration [FHWA] [7] and for the bridge girders optimized by MIT for the FHWA [9]. The macroscopic material properties are obtained from a compression and a tension test supplied by the manufacturer, which can be found in Reference [7]. One of the tensile test results is shown in Figure 2-9. The macroscopic material properties of Ductal^{TM}-Steel Fiber that were extracted from this curve are summarized in Table 2.2. A simplified stress-strain curve for the entire stress range is illustrated in Figure 2-10, with corresponding strains presented in Table 2.3.
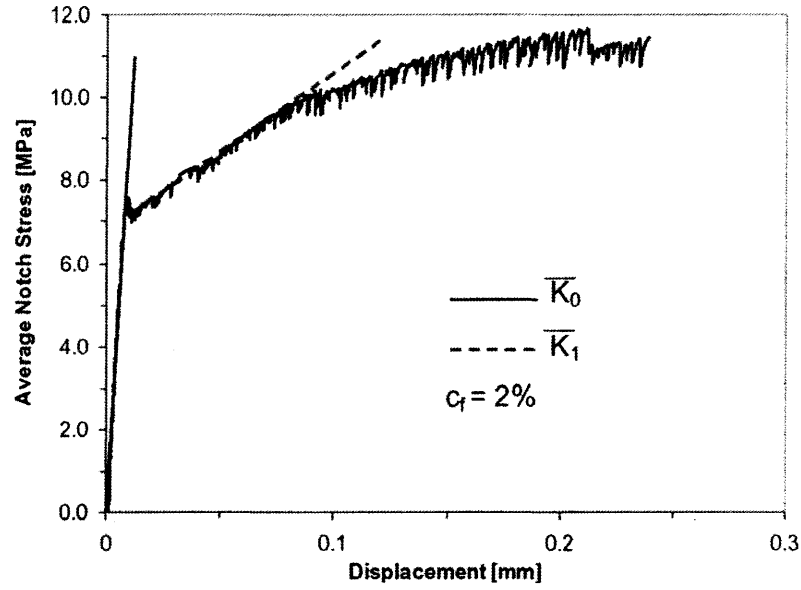
Figure 2-9: Average notch stress-displacement curve for Ductal^{TM}-Steel Fiber [7].

		Notation	Ductal^{TM}-SF
Macroscopic		K_0	53.9 GPa
Stiffness		K_1	1.6 GPa ($\approx$ 3 % of K_0)
Macroscopic	**Tension**	$\Sigma_{t,1}^-$	7.6 MPa
Strength		$\Sigma_{t,1}^+$	6.9 MPa
		$\Sigma_{t,2}$	11.5 MPa
	Compression	$\Sigma_{c,1}^-$	190 MPa
		$\Sigma_{c,1}^+$	173 MPa
		$\Sigma_{c,2}$	183 MPa

Table 2.2: Macroscopic material properties of UHPC material and typical values for Ductal^{TM}-Steel Fiber [18].

	Tension	Compression
Initial Strain Limit	$E_{t,1} = 1.41 \times 10^{-4}$	$E_{c,1} = 3.40 \times 10^{-4}$
Yield Strain Limit	$E_{t,2} = 3.02 \times 10^{-3}$	$E_{c,2} = 1.40 \times 10^{-2}$

Table 2.3: Macroscopic strain limits in the simplified stress-strain curve for Ductal^{TM}-Steel Fiber

44
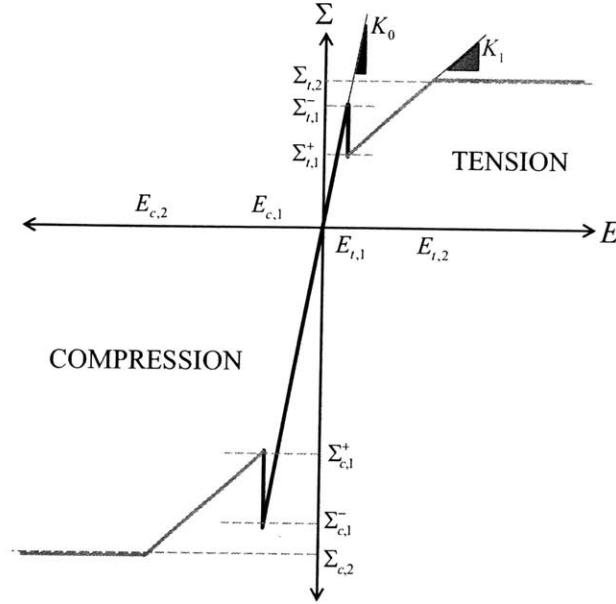
Figure 2-10: Simplified stress-strain curve of UHPC in uniaxial tension and compression.

2.4.2 Review of the Assumptions for the 3-D Model Parameters

The isotropic UHPC material behavior is completely described by *15 material properties*: 6 elastic properties (C_M, ν_M, C_F, ν_F, M^{3-D}, and ν_I) and 9 strength properties (σ_{Mt}, σ_{Mc}, σ_{Mb}, σ_{Mt}^{cr}, σ_{Mc}^{cr}, σ_{Mb}^{cr}, σ_{Ft}, σ_{Fc}, and σ_{Fb}). In order to further reduce the number of model parameters, three assumptions are introduced:

1. The Poisson's ratio is the same in the matrix, the fiber, and the matrix-fiber coupling, which makes ν_F and ν_I dependent parameters.

2. The post-cracking matrix strengths are reduced by the same factor, γ^{cr} defined by (2.19), which makes σ_{Mc}^{cr} and σ_{Mb}^{cr} dependent parameters.

3. The loading function related to the biaxial compressive strength of the fiber is disregarded, which makes σ_{Fb} unnecessary.

These assumptions reduce the number of model parameters to *10 independent model parameters* which can be obtained from the macroscopic stress-stain relationship. These model parameters are summarized in Table 2.4.

2.4.3 Determination of the 3-D Model Parameters

Using (2.4) and (2.5), the *six* model parameters related to the tensile behavior of UHPC (C_M, C_F, M, σ_{Mt}, σ_{Mt}^{cr} and σ_{Ft}) are derived from the results of a tensile test.

In order to close the determination of the 3-D model parameters, we need to obtain the *four* additional model parameters related to the compressive behavior and the Poisson's ratio of UHPC. The two model parameters related to the compressive behavior of UHPC (σ_{Mc} and σ_{Fc}) are derived from the results of a uniaxial compression test using the following equations:

$$
\begin{aligned}
\Sigma_{c,1}^{-} &= \left(1 + \frac{C_F}{C_M}\right)\sigma_{Mc} \simeq \sigma_{Mc} \\
\Sigma_{c,1}^{+} &= \Sigma_{c,1}^{-} - \frac{C_M}{C_M+M}\left(\sigma_{Mc} - \sigma_{Mc}^{cr}\right) \simeq \sigma_{Mc}^{cr} = \gamma^{cr}\sigma_{Mc} \\
\Sigma_{c,2} &= \sigma_{Fc} + \sigma_{Mc}^{cr} = \sigma_{Fc} + \gamma^{cr}\sigma_{Mc}
\end{aligned}
\tag{2.64}
$$

These equations have a form similar to the tensile strength relations in (2.2) and (2.5). The composite matrix biaxial strength (σ_{Mb}) can be determined from an additional test, a biaxial compression test on an unreinforced cementitious specimen. More simply, it can be estimated from known biaxial strength factors for unreinforced concrete as follows [11]:

$$
\sigma_{Mb} \approx 1.2\sigma_{Mc}
\tag{2.65}
$$

Finally, the composite Poisson's ratio (ν) can also be estimated from standard Poisson's ratios of cementitious materials:

$$
\nu = \nu_M \approx 0.17
\tag{2.66}
$$

In summary, the 3-D model parameters is obtained from a single tensile test and a single compression test. Typical values for Ductal^{TM}-Steel Fiber are summarized in Table 2.4. These input model parameters are used throughout this report.

2.5 Chapter Summary

This chapter reviews the two-phase macroscopic model for the stress-strain behavior of hardened UHPC material. A typical tensile response of hardened UHPC can be simplified in four regions: an elastic behavior, a brittle strength drop, a post-cracking behavior, and a composite

		Notation	Ductal^{TM}-SF
Elastic		C_M	53.9 GPa
Parameter		C_F	0.0 GPa
		M	1.65 GPa
		ν	0.17
Strength	**Matrix**	σ_{Mt} $(= f_t + k_M)$	7.6 MPa
Parameter		σ_{Mt}^{cr} $(= k_M)$	6.9 MPa
		σ_{Mc}	190 MPa
		σ_{Mb}	220 MPa
	Fiber	σ_{Ft} $(= f_y)$	4.6 MPa
		σ_{Fc}	10 MPa

Table 2.4: Input material parameters of the 3D UHPC model and typical values Ductal^{TM}-Steel Fiber [18].

yielding. The 1-D model parameters properly capture the simplified UHPC material behavior by introducing separately a composite matrix and a composite fiber phase. The 1-D hardened UHPC model is easily extended to 3-D, by replacing the scalar quantities in the governing equations by their tensorial counterparts. The 3-D macroscopic model is constructed around three main components: the 3-D constitutive relations, plasticity of the 3-D model, and consistency with the 1-D model. The hardened 3-D UHPC model has the following interesting properties:

- The macroscopic nature of the two-phase model allows us to capture typical feature of UHPC material behavior, with six material parameters of clear physical significance. The stress drop modeled by this model allows the representation of progressive cracking with increased loading. This makes it easy to fit the six material parameters of the model to experimental test results.

- The two phase modeling of fibers and matrix allows a quantification of their individual behaviors and their interaction. The cracking in UHPC is represented as permanent plastic strains in the composite matrix, which allows one to evaluate the risk of cracking.

47

Chapter 3

HYDRATION KINETICS MODEL FOR ORDINARY CONCRETE

The focus of the research presented here is the modeling of UHPC at early ages. Like for all cement-based materials, the particular behavior of UHPC at early ages stems from the hydration of cement, which is a highly exothermic and thermally activated reaction. The hydration reaction leads to heat generation inducing thermal shrinkage during the cooling process. Moreover, chemical shrinkage occurs because the volume of hydration products is less than the original volume of cement and water. Concrete cracking at early ages is mainly caused by both thermal and chemical shrinkage, which induce a severe state of stress beyond the material strength developed. In this chapter, we review a hydration kinetics model for ordinary concrete, which we extend in the sequel to UHPC materials.

3.1 Hydration of Cement

Ordinary Portland cement consists of various clinker phases, which react with water during hydration. Most dominant clinker phases are[1] tricalcium silicates (C_3S), dicalcium silicates (C_2S), tricalcium aluminates (C_3A) and tetracalcium aluminum ferrites (C_4AF). A typical mineralogical composition and mass ratios of clinker phases in Portland cements are given in

---

[1]The notation of cement chemists is used; $C = CaO$; $S = SiO_2$; $A = Al_2O_3$; $F = Fe_2O_3$; $\bar{S} = SO_3$; $H = H_2O$.

48

Name of Compound	Oxide Composition	Abbreviation	Mass Ratio [%]
Tricalcium Silicates (Alite)	$3CaO \cdot SiO_2$	C_3S	50-70
Dicalcium Silicates (Belite)	$2CaO \cdot SiO_2$	C_2S	15-30
Tricalcium Aluminates (Aluminates)	$3CaO \cdot Al_2O_3$	C_3A	5-10
Tetracalcium Aluminum Ferrites (Ferrites)	$4CaO \cdot Al_2O_3 \cdot Fe_2O_3$	C_4AF	5-15

Table 3.1: Main Compounds of Portland Cement [17].

Table 3.1. We describe briefly the hydration of silicates and aluminates, because the main hydrates, which can be broadly classified as calcium silicate hydrates (C-S-H) and calcium aluminate hydrates (C-A-H), form the most important part of the microstructure of a cement paste. This section briefly reviews the simplified stoichiometric reactions for the hydration of the four dominant compounds in Portland cement as suggested by Tennis and Jennings [23].

3.1.1 Silicate Hydration

The main products of the cement hydration are from the hydration of silicates, and they define the quantity of calcium silicate hydrates (C-S-H) formed. The hydration reaction of C$_3$S and C$_2$S can be written as follows:

$$2C_3S + 10.6H \rightarrow C_{3.4}S_2H_8 + 2.6CH \tag{3.1}$$

$$2C_2S + 8.6H \rightarrow C_{3.4}S_2H_8 + 0.6CH \tag{3.2}$$
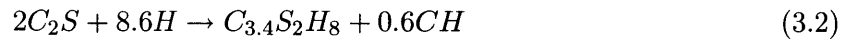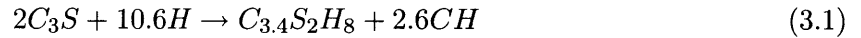
In both cases, the products of the hydration are composed of calcium silicate hydrates (C-S-H) and calcium hydroxide (CH). C-S-H constitutes approximately 50-70 % of the hydration product volume, and its physical properties are of interest in connection with setting and hardening properties of cement. CH, which is also called Portlandite, constitutes typically 20-25 % of the hydration product volume [10].

3.1.2 Aluminate Hydration

In the presence of sulfate (SO_4^{2-}) and water, C_3A forms Ettringite (AFt phase):

$$C_3A + 3C\bar{S}H_2 + 26H \rightarrow C_6A\bar{S}_3H_{32} \tag{3.3}$$
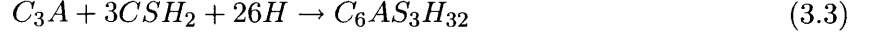
After the sulfate (SO_4^{2-}) is consumed, C_3A and Ettringite (AFt phase) become monosulfoaluminates (AFm phase):

$$2C_3A + 3C_6\bar{S}_3H_{32} + 4H \rightarrow 3C_6A\bar{S}H_{12} \tag{3.4}$$

After all the Ettringite (AFt) is consumed, the rest of C_3A continues to hydrate as follows:

$$C_3A + CH + 12H \rightarrow C_4AH_{13} \tag{3.5}$$

Many investigations have shown that the hydration of C_4AF is very similar to that of C_3A. As in the case of C_3A, the first crystalline products to form in the absence and presence of the sulfate (SO_4^{-2}) are AFm phase and AFt phase, respectively, and the AFt phase is later replaced by AFm phase. Eventually, the product of the ferrite reaction is a hydrogarnet $(C_3(A, F) H_6)$ described by the following equation:

$$C_4AF + 2CH + 10H \rightarrow 2C_3(A, F)H_6 \tag{3.6}$$
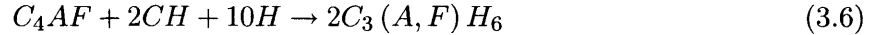
3.2 Macroscopic Modeling of Hydration Reaction for Ordinary Concrete

As the hydration reaction progresses, the material stiffness increases, and the evolving stiffness leads to the development of stresses in the material. The hydration reaction also affects the strength of material, which influences the crack threshold at early age. Hence, there is a competition between the stress development due to the evolving stiffness and the crack threshold development due to strength growth. In order to capture the effects of thermal and chemical phenomena related to hydration reaction on the mechanical properties, a thermodynamic framework is necessary for the modeling. This section reviews the thermo-chemo-mechanical

modeling of the hydration reaction proposed by Ulm and Coussy [25] [26].

3.2.1 Simplification of Hydration Reaction Modeling

Given the complexity of the hydration of cement as presented in Section 3.1, it is useful to simplify the different process in a first engineering approach. Ulm and Coussy suggest the *diffusion of water* through the layers of hydrates as the dominant mechanism of the hydration kinetics[2]. For the reaction to occur, water diffuses through the layers of hydrates. Once water meets the unhydrated cement, new hydrates are formed instantaneously compared to the time scale of the diffusion process. Figure 3-1 illustrates this hydration reaction process, and the hydration reaction can be simplified as follows:

$$Free \ Water \ \rightarrow \ Combined \ Water \tag{3.7}$$
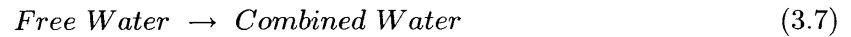
where the reactant phase corresponds to the free water and the product phase to the water combined in the hydrates. Furthermore, as a measure of the reaction extent, a hydration degree (ξ) is introduced and it is defined by the following equation:

$$\xi(t) = \frac{m(t)}{m_\infty} \tag{3.8}$$

where m_∞ is the asymptotic value of combined water mass, and $m(t)$ is the combined water mass at time t. At the beginning of the reaction, the hydration degree is zero. As the hydration progresses, it increases. Eventually, the hydration degree becomes one when the reaction is complete. The hydration degree is controlled by the chemical affinity A, which represents the thermodynamic imbalance between the chemical potentials of reactant phase and product phase.

---

[2] Kinetics is the branch of chemistry that is concerned with the rates of change in the concentration of reactants in a chemical reaction.
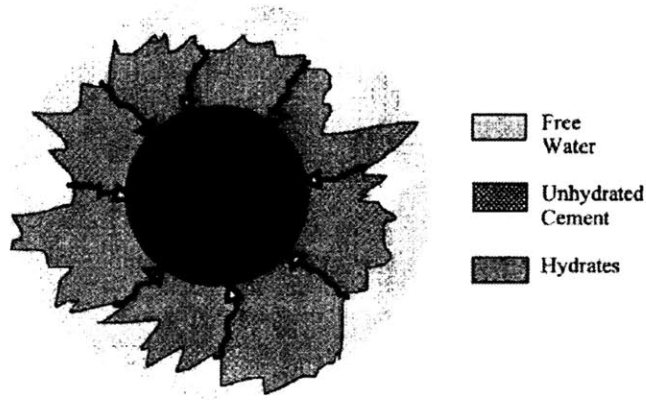
Figure 3-1: Diffusion of water through layers of hydrates [25].

3.2.2 Thermodynamic Framework for Ordinary Concrete at Early Ages

Like the hardened 3-D UHPC model, the starting point of the hydration kinetics model is the Clausius-Duhem inequality[3] [24]:

$$\varphi dt = \mathbf{\Sigma} \colon d\mathbf{E} - SdT - d\Psi \geq 0 \tag{3.9}$$

where φdt stands for the dissipation; $\mathbf{\Sigma}$ and $\mathbf{E}$ are the 2nd order macroscopic stress tensor and macroscopic strain tensor, respectively; S and T stand for the entropy and absolute temperature, respectively; and Ψ is the free energy.   Assuming the elementary system to be closed, the hydration degree, $\xi(t)$, can be considered as an internal state variable.   For concrete at early ages, there are three state variables, $\mathbf{E}$, T and ξ, which describe the energy state of the system. In the framework of physical linearization, the free energy is limited to a 2nd order expansion with respect to external state variables, $\mathbf{E}$ and T, and it reads:

$$
\begin{aligned}
\Psi &= \Psi(\varepsilon, T, \xi) \\
&= \Psi_0 + \Psi_2 + \Psi_1
\end{aligned}
\tag{3.10}
$$

---

[3]The Clausius-Duhem inequality states that the external energy supplied in form of work is not entirely stored in the system in form of elastic energy that can be recovered later on; but dissipated into heat form.

52

where Ψ_0 is the free energy relating to the initial state of stress, entropy, and chemical affinity; Ψ_2 relates to the elastic potential energy which is a second-order tensor expansion with respect to strain, absolute temperature and hydration degree; and Ψ_1 is the free energy associated with the coupling of phenomena of different origins:

$$
\begin{aligned}
\Psi_0 &= \boldsymbol{\Sigma}_0 \colon \mathbf{E} - S_0 \, (T - T_0) - A_0 \xi \\
\Psi_2 &= \tfrac{1}{2} \mathbf{E} \colon \mathbb{C}\,(\xi) \colon \mathbf{E} - \tfrac{1}{2} \tfrac{C}{T_0} \, (T - T_0)^2 + \tfrac{1}{2} \kappa \xi^2 \\
\Psi_1 &= -\mathbb{C}\,(\xi) \colon \mathbf{E} \colon \boldsymbol{\alpha} \, (T - T_0) - \mathbb{C}\,(\xi) \colon \mathbf{E} \colon \boldsymbol{\beta} \xi + \tfrac{L}{T_0} \xi \, (T - T_0)
\end{aligned}
\tag{3.11}
$$

where subscript "0" means initial state of each driving force; $\mathbb{C}\,(\xi)$ is the 4th order stiffness tensors of the aging concrete; C is the volume heat capacity; κ is a coefficient relating to the hydration kinetics; $\boldsymbol{\alpha}$ is the 2nd order thermal dilatation coefficient tensor; $\boldsymbol{\beta}$ is the 2nd order chemical dilatation coefficient tensor; and L is the latent heat of the hydration reaction. Here, for the sake of simplicity, the thermal and chemical dilatation coefficient tensors ($\boldsymbol{\alpha}$ and $\boldsymbol{\beta}$) are constant, and the volume heat capacity, the hydration kinetics coefficient and the latent heat (C, κ and L) are also considered to be constant. Use of (3.10) in (3.9) yields the state equations, which read in an incremental form:

$$
\left\{
\begin{array}{c}
d\boldsymbol{\Sigma} \\
dS \\
dA
\end{array}
\right\}
=
\left[
\begin{array}{ccc}
\mathbb{C}\,(\xi) & -\mathbb{C}\,(\xi) \colon \boldsymbol{\alpha} & -\mathbb{C}\,(\xi) \colon \boldsymbol{\beta} \\
\mathbb{C}\,(\xi) \colon \boldsymbol{\alpha} & \dfrac{C}{T_0} & -\dfrac{L}{T_0} \\
\mathbb{C}\,(\xi) \colon \boldsymbol{\beta} & -\dfrac{L}{T_0} & -\kappa
\end{array}
\right]
\colon
\left\{
\begin{array}{c}
d\mathbf{E} \\
dT \\
d\xi
\end{array}
\right\}
\tag{3.12}
$$

where the hypothesis of infinitesimal deformation is applied so that each driving force can be expressed by only the terms of the same order of magnitude as strain. In this derivation, the strains due to elastic, thermal, and chemical change are infinitesimal:

$$
\begin{aligned}
&tr\boldsymbol{\varepsilon} \ll 1 \\
&tr\boldsymbol{\varepsilon}^t = tr\,(\boldsymbol{\alpha}\,(T - T_0)) \ll 1 \\
&tr\boldsymbol{\varepsilon}^c = tr\,(\boldsymbol{\beta}\xi) \ll 1
\end{aligned}
\tag{3.13}
$$

where $\boldsymbol{\varepsilon}^t$ and $\boldsymbol{\varepsilon}^c$ denote the strains due to thermal change and chemical change, respectively.

It is generally found that the thermal changes and chemical changes affect the mechanical
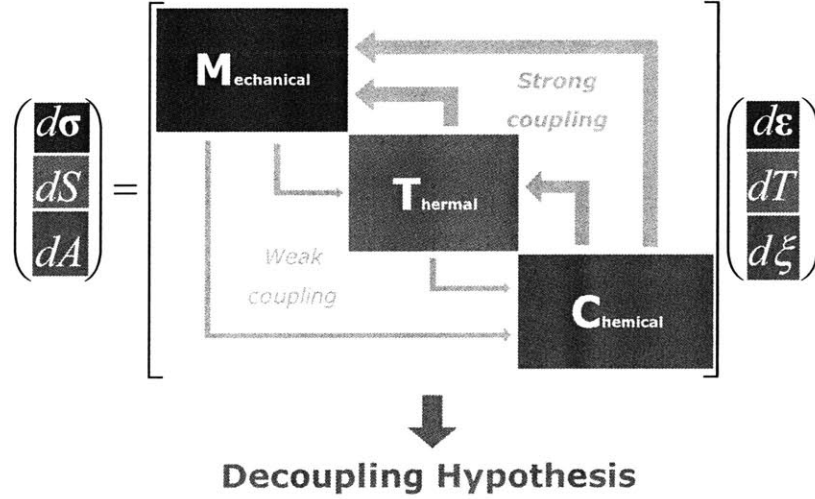
Figure 3-2: Thermo-chemo-mechanical coupling in early-age ordinary concrete and introduction of decoupling hypothesis.

problem, producing stresses and strains. It is also generally found that the chemical changes affect the thermal problem, producing heat. This means that the coupling terms in the upper off-diagonal region in (3.12) are of non-negligible order. However, it is also found for concrete materials that the mechanical change has little effect on the thermal and the chemical problem. In addition, it is found for concrete materials that thermal change has little effect on the chemical problem. As a consequence, there are weak coupling terms in the lower off-diagonal region in (3.12). Thus, to simplify the formulation, a partial decoupling hypothesis is applied by considering only the strong couplings and by neglecting the weak couplings (Figure 3-2). This decoupling hypothesis allows us to obtain the following partially decoupled constitutive relations:

$$
\left\{
\begin{array}{c}
d\Sigma \\
dS \\
dA
\end{array}
\right\}
=
\left[
\begin{array}{ccc}
\mathbb{C}\left(\xi\right) & -\mathbb{C}\left(\xi\right):\boldsymbol{\alpha} & -\mathbb{C}\left(\xi\right):\boldsymbol{\beta} \\
0 & \frac{C}{T_0} & -\frac{L}{T_0} \\
0 & 0 & -\kappa
\end{array}
\right]
:
\left\{
\begin{array}{c}
d\mathbf{E} \\
dT \\
d\xi
\end{array}
\right\}
\qquad (3.14)
$$

The equation for the affinity (A) enters the hydration kinetics law, and the equation for entropy (S) enters the heat equation. For the mechanical problem, the equation for the stress (Σ) enters the equilibrium equation. The next subsections are devoted to the details of each problem.

Hydration Kinetics

From the partially decoupled constitutive relations (3.14), the affinity is given by:

$$dA = -\kappa d\xi \tag{3.15}$$

If we integrate both sides of the equation, it is readily found that the affinity which depends on the hydration degree:

$$A = A(\xi) \tag{3.16}$$

The form of $A(\xi)$ specifies the reaction order. It is the driving force of the reaction kinetics. This reaction kinetics is specified by a kinetics law, which for a thermally activated chemical reaction reads:

$$
\begin{aligned}
\frac{d\xi}{dt} &= \frac{A(\xi)}{\tau^*(T_0)} exp\left[-\frac{E_a}{R}\left(\frac{1}{T}-\frac{1}{T_0}\right)\right] \\
&= \frac{A(\xi)}{\tau(T_0)} exp\left[-\frac{E_a}{RT}\right]
\end{aligned}
\tag{3.17}
$$

where

$$\tau(T_0) = \tau^*(T_0) exp\left[-\frac{E_a}{RT}\right] \tag{3.18}$$

Here, τ^* and τ are the characteristic reaction times[4]; E_a is the activation energy of the hydration reaction[5]; and R is the universal gas constant. The value of E_a/R can be found in cement chemistry handbooks [13]. Once known, the chemical affinity, $A(\xi)$, can be obtained from experiments which allow us to access the hydration reaction rate, $d\xi/dt$, and the characteristic reaction time, τ. The experiments can be one of adiabatic calorimetric experiments or isothermal strength evolution tests as detailed below.

---

[4]The characteristic time (τ^* or τ) depends typically on the type of cement.

[5]The activation energy over the universal gas constant (E_a/R) is a constant for most cement and is known to be roughly $4,000\ K$.

Heat Equation

From the partially decoupled constitutive relations (3.14), the equation for entropy can be written as follows:

$$dS = \frac{C}{T_0} dT - \frac{L}{T_0} d\xi \qquad (3.19)$$

This entropy expression enters the 2nd law of thermodynamics of the closed system reading:

$$T_0 \frac{dS}{dt} - \varphi = -div\mathbf{q} \qquad (3.20)$$

where φ is the dissipation rate, $div\mathbf{q}$ is the external rate of heat supply to the elementary system provided by conduction, and $\mathbf{q}$ is the heat flux vector. For the heat condition, a linear law is adopted reading:

$$\mathbf{q} = -\mathbf{K} \cdot \nabla T = -K \nabla T \qquad (3.21)$$

where $\mathbf{K} = K\mathbf{1}$ is the thermal conductivity tensor in the isotropic case. The thermal conductivity, K, might depend on the hydration degree, but it is assumed to be constant in this model.

Assuming that the latent heat due to deformation and the heat due to chemical dissipation are negligible with respect to the latent hydration heat L, substituting (3.19) and (3.21) into (3.20) yields the following heat equation:

$$C \frac{dT}{dt} = K \nabla^2 T + L \frac{d\xi}{dt} \qquad (3.22)$$

where the left side of the equation, $C \, dT/dt$, means change in energy stored within the system, the first term on the right side, $K \nabla^2 T$, is the net heat rate provided from the outside by conduction, and the term, $L \, d\xi/dt$, is the heat generated by hydration. Thus, this heat equation states that the stored energy change due to the temperature variation is equal to the sum of the external heat supply due to thermal conductivity and the latent heat of the hydration reaction.

The heat equation needs to be completed by thermal boundary conditions, which prescribe

either the temperature or the heat flux through the boundary, $\partial\Omega$:

$$
\begin{aligned}
T &= T^d & \text{on} \quad &\partial\Omega_T \\
\mathbf{q} \cdot \mathbf{n} &= q^d & \text{on} \quad &\partial\Omega_q \\
\mathbf{q} \cdot \mathbf{n} &= \lambda\left(T - T_{ext}\right) & \text{on} \quad &\partial\Omega_\lambda
\end{aligned}
\tag{3.23}
$$

$$
\begin{aligned}
\partial\Omega_T \cup \partial\Omega_q \cup \partial\Omega_\lambda &= \partial\Omega \\
\partial\Omega_T \cap \partial\Omega_q = \partial\Omega_q \cap \partial\Omega_\lambda &= \partial\Omega_\lambda \cap \partial\Omega_T = 0
\end{aligned}
\tag{3.24}
$$

where $\mathbf{n}$ is the normal unit vector toward the outside of $\partial\Omega_q$ or $\partial\Omega_\lambda$; T^d and q^d are the prescribed temperature and the heat flux, respectively; λ is the exchange coefficient[6]; and T_{ext} is the external temperature. Solving simultaneously the heat equation (3.22) and the hydration kinetics law (3.17) for the boundary conditions (3.23) allows one to determine a materials or structural system.

Equilibrium Equation

From (3.14), the constitutive equation for stress reads:

$$
d\boldsymbol{\Sigma} = \mathbb{C}\left(\xi\right) : d\mathbf{E} - \mathbb{C}\left(\xi\right) : \boldsymbol{\alpha}dT - \mathbb{C}\left(\xi\right) : \boldsymbol{\beta}d\xi
\tag{3.25}
$$

Three effects relative to early-age concrete behavior are considered in (3.25):

- The aging elasticity, $\mathbb{C}\left(\xi\right)$, representing the increase of the stiffness as a function of the hydration degree;

- The thermal stresses, $-\mathbb{C}\left(\xi\right) : \boldsymbol{\alpha}dT$, related to restrained thermal dilatation;

- The chemical stresses, $-\mathbb{C}\left(\xi\right) : \boldsymbol{\beta}d\xi$, related to restrained autogenous shrinkage.

The general 3-D constitutive model involves 39 ($= 21 + 2 \times 9$) parameters associated with the stiffness tensor $\mathbb{C}\left(\xi\right)$, the thermal dilatation coefficient tensor $\boldsymbol{\alpha}$, and the chemical dilatation

---

[6]The exchange coefficients for various external conditions can be found in Reference [27].

tensor $\boldsymbol{\beta}$. In the isotropic case, the stiffness tensor can be described by two unique scalar values:

$$\mathbb{C}\left(\xi\right) = 3K\left(\xi\right)\mathbb{K} + 2G\left(\xi\right)\mathbb{J} \tag{3.26}$$

where $K\left(\xi\right)$ is the aging bulk modulus, and $G\left(\xi\right)$ is the aging shear modulus of concrete. The aging bulk modulus and the aging shear modulus are related to the aging Young's modulus of the concrete, $E\left(\xi\right)$, by:

$$
\begin{aligned}
K\left(\xi\right) &= \frac{E(\xi)}{3(1-2\nu)} \\
G\left(\xi\right) &= \frac{E(\xi)}{2(1+\nu)}
\end{aligned}
\tag{3.27}
$$

where ν is the Poisson's ratios of the concrete. The Poisson's ratio is assumed to be constant in the modeling. Isotropy of the material also implies:

$$\boldsymbol{\alpha} = \alpha\mathbf{1}; \quad \boldsymbol{\beta} = \beta\mathbf{1} \tag{3.28}$$

where α and β are the thermal and the chemical dilatation coefficient, respectively. Equation (3.25) can be restated in an isotropic format:

$$d\boldsymbol{\Sigma} = d\Sigma^v\mathbf{1} + d\boldsymbol{\Sigma}^d \tag{3.29}$$

where $d\Sigma^v = \frac{1}{3}tr\left(d\boldsymbol{\Sigma}\right)$ is the volumetric stress increment; and $d\boldsymbol{\Sigma}^d$ is the deviatoric stress increment. The volumetric stress-strains are represented by:

$$d\Sigma^v = 3K\left(\xi\right)\left(dE^v - \alpha dT - \beta d\xi\right) \tag{3.30}$$

where $dE^v = \frac{1}{3}tr\left(d\mathbf{E}\right)$ is the volumetric strain increment. Similarly, the deviatoric stress-strain relations are given by:

$$d\boldsymbol{\Sigma}^d = 2G\left(\xi\right)d\mathbf{E}^d \tag{3.31}$$

where $d\mathbf{E}^d = d\mathbf{E} - dE^v\mathbf{1}$ is deviatoric strain increment.

The constitutive relations are complete by applying the results of the hydration kinetics and the heat equation, i.e. the time history of the temperature and the hydration degree in the system. With this constitutive relation , the stress equilibrium equation is solved in order to

find statically admissible stress fields:

$$div\mathbf{\Sigma} + \rho\mathbf{f} = 0$$

where ρ is the mass density; and $\mathbf{f}$ is the volume force density.

3.3 Macroscopic Investigation of Hydration Kinetics for Ordinary Concrete

As shown in Section 3.2.2, the hydration kinetics is the starting point of modeling ordinary concrete at early ages. Thus, the determination of the chemical affinity function, $A(\xi)$, plays an important role in the modeling. In order to determine experimentally the chemical affinity expressed in (3.17), the evolution of the hydration degree, $\xi(t)$, and the time history of temperature, $T(\xi)$, must be measured. Here, two generally accepted experiments are reviewed; adiabatic calorimetry experiment and isothermal strength evolution.

3.3.1 Adiabatic Calorimetric Experiment

The adiabatic calorimetric experiment is a standard method for accessing hydration kinetics. It is generally admitted that the increase rate of adiabatic temperature is proportional to the hydration reaction rate as follows:

$$\frac{d\xi}{dt} \propto \frac{dT^{ad}}{dt} \tag{3.32}$$

where T^{ad} is the adiabatic temperature. Writing the heat equation (3.22) for adiabatic conditions ($div\mathbf{q} = 0$) yields after integration:

$$\xi(t) = \frac{T^{ad}(t) - T_0^{ad}}{L/C} \tag{3.33}$$

where $L/C = T_\infty^{ad} - T_0^{ad}$ is the adiabatic temperature rise; and T_0^{ad} and T_∞^{ad} are the initial and the final temperatures in the experiment. Then, writing (3.33) in the kinetic law (3.17) yields:

$$
\begin{aligned}
\frac{d\xi}{dt} &= \frac{1}{T_\infty^{ad} - T_0} \frac{dT^{ad}}{dt} \\
&= \frac{A(\xi)}{\tau(T_0^{ad})} exp\left[-\frac{E_a}{RT^{ad}(t)}\right]
\end{aligned}
\tag{3.34}
$$

Eventually, the normalized chemical affinity, $\tilde{A}(\xi)$, is identified from the adiabatic calorimetric experiment:

$$
\begin{aligned}
\tilde{A}(\xi) &= \frac{A(\xi)}{\tau(T_0^{ad})} \\
&= exp\left[\frac{E_a}{RT^{ad}(t)}\right] \frac{1}{T_\infty^{ad} - T_0^{ad}} \frac{dT^{ad}}{dt}
\end{aligned}
\tag{3.35}
$$

Ulm and Coussy [26] suggested that $\tilde{A}(\xi)$ was an intrinsic kinetic function; i.e. on that does not depends on boundary conditions.

3.3.2 Isothermal Strength Evolution

The strength growth is another manifestation of the hydration reaction. It is generally admitted that the increase rate of isothermal strength growth is proportional to the hydration rate:

$$
\frac{d\xi}{dt} \propto \frac{df^{iso}}{dt}
\tag{3.36}
$$

where f^{iso} is the isothermal strength value. Similarly to (3.33), the hydration degree is determined from strength measurements:

$$
\xi(t) = \frac{f^{iso}(t) - f_0}{f_\infty^{ad} - f_0}
\tag{3.37}
$$

where f_0^{iso} (≤ 0) is a reference strength value for $\xi = 0$, which relates to the percolation threshold; and f_∞^{ad} is the asymptotic strength at complete hydration. Then, using (3.37) in (3.17)

60

yields a second means to a access the hydration rate from:

$$
\begin{aligned}
\frac{d\xi}{dt} &= \frac{1}{f^{iso}_{\infty} - f_0} \frac{df^{iso}}{dt} \\
&= \frac{A(\xi)}{\tau\left(T^{iso}_0\right)} exp\left[-\frac{E_a}{RT^{iso}_0}\right]
\end{aligned}
\tag{3.38}
$$

Eventually, the normalized chemical affinity, $\tilde{A}(\xi)$, is identified from the isothermal strength evolution test:

$$
\begin{aligned}
\tilde{A}(\xi) &= \frac{A(\xi)}{\tau\left(T^{iso}_0\right)} \\
&= exp\left[\frac{E_a}{RT^{iso}_0}\right] \frac{1}{f^{iso}_{\infty} - f_0} \frac{df^{iso}}{dt}
\end{aligned}
\tag{3.39}
$$

3.4 Chapter Summary

In this chapter, we reviewed a hydration kinetics model for ordinary concrete, which allows the modeling of thermo-chemo-mechanical couplings of concrete at early ages at the macro-level of material description. The main points to be noted are:

- The diffusion of free water through the layers of hydrates is considered as the dominant mechanism of the hydration with respect to the kinetics. The model for ordinary concrete at early ages accounts explicitly for the hydration reaction at the macroscopic scale through the hydration degree ξ.

- By means of some simplifying decoupling hypothesis, it is possible to obtain partially decoupled constitutive relations which are easy to handle: hydration kinetics, heat equation and stress constitutive equation.

- In this model, the normalized affinity $\tilde{A}$ considered to be an intrinsic kinetic function, which characterizes the macroscopic hydration kinetics of concrete. This function can be determined from standard material tests, such as calorimetric tests or material strength evolution tests.

Part II

MATERIAL MODELING

Chapter 4

EARLY-AGE UHPC MATERIAL MODEL

This Chapter is dedicated to the development of a new material model for early-age UHPC, which combines the hardened UHPC model reviewed in Chapter 2 and the hydration kinetics model reviewed in Chapter 3. We start by considering the additional features we consider in the modeling of early-age UHPC behavior. The model is then developed in a consistent thermodynamic framework, and consistent decoupling hypothesis are introduced to obtain an appropriate engineering model for the prediction of temperature, stresses and strains in early-age UHPC.

4.1 Evolving UHPC Material Model

Unlike hardened UHPC, the properties of UHPC at early ages are not constant, but evolve as the hydration progresses. In terms of the 1-D Think model of UHPC, displayed in Figure 4-1 (a), the strength and stiffness properties relating to the matrix phase now depend on the hydration degree:

$$C_M \to C_M\left(\xi\right)$$
$$f_t \to f_t\left(\xi\right) \tag{4.1}$$
$$k_M \to k_M\left(\xi\right)$$
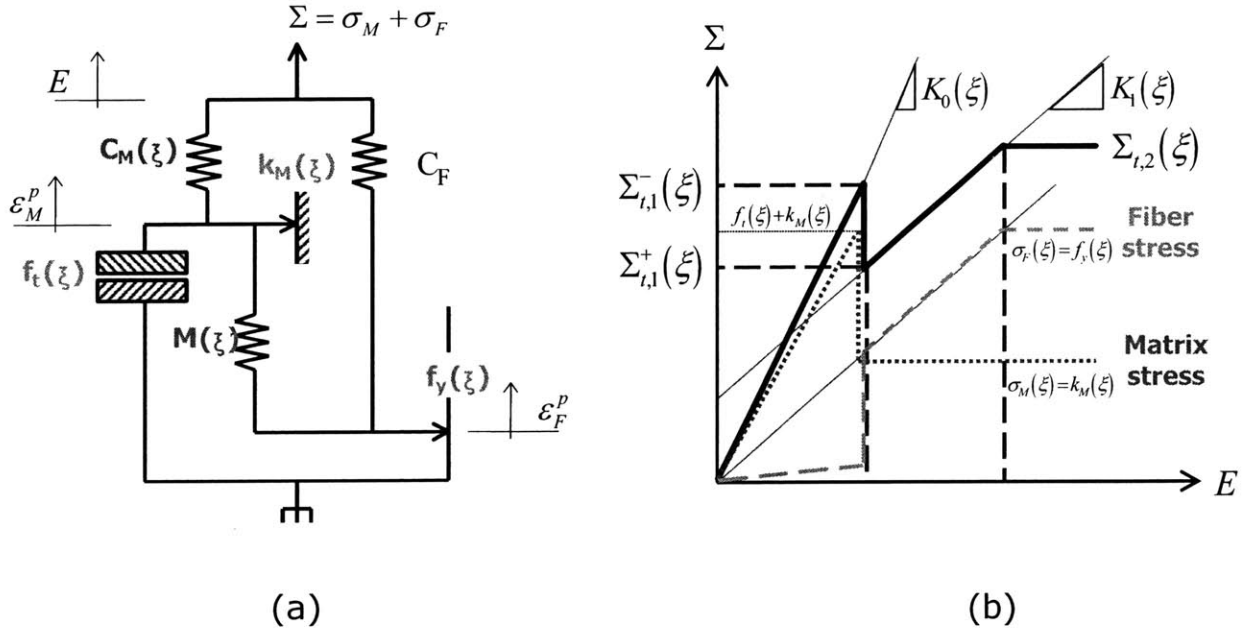
Figure 4-1: (a) 1-D Think Model of a two-phase matrix-fiber composite material for UHPC at early-ages, (b) Stress-strain response for UHPC at early ages.

Furthermore, since the composite fiber phase in the 1-D model represents the plastic pullout behavior of the fibers during composite yielding (see Section 2.2), it is readily understood that this pullout behavior also depends on the hydration state of the matrix phase:

$$f_y \to f_y(\xi) \tag{4.2}$$

Similarly, the coupling modulus M, which links the irreversible matrix behavior (plastic strain ε_M^p) with the irreversible reinforcing fiber behavior (plastic strain ε_F^p), is also affected by the hydration state of the matrix phase. This is expressed by considering the coupling modulus M as a function of the hydration degree:

$$M \to M(\xi) \tag{4.3}$$

These modifications regarding the stiffness and strength parameters of the 1-D UHPC model are depicted in Figure 4-1 (a).

Like in the case of the hardened UHPC model, the following relations between macroscopic material properties and model parameters are obtained (see Figure 4-1 (b)):

$$K_0\left(\xi\right) \simeq C_M\left(\xi\right)$$
$$K_1\left(\xi\right) \simeq \frac{C_M(\xi)M(\xi)}{C_M(\xi)+M(\xi)} \tag{4.4}$$

$$\Sigma_{t,1}^-\left(\xi\right) \simeq f_t\left(\xi\right) + k_M\left(\xi\right) \quad \text{with} \quad E_1^- = \frac{f_t(\xi)+k_M(\xi)}{C_M(\xi)}$$
$$\Sigma_{t,1}^+\left(\xi\right) \simeq k_M\left(\xi\right) \qquad\qquad \text{with} \quad E_1^+ = \frac{f_t(\xi)+k_M(\xi)}{C_M(\xi)} \tag{4.5}$$
$$\Sigma_{t,2}\left(\xi\right) = f_y\left(\xi\right) + k_M\left(\xi\right) \quad \text{with} \quad E_2 \simeq \frac{k_M(\xi)M(\xi)+f_y(\xi)[C_M(\xi)+M(\xi)]}{C_M(\xi)M(\xi)}$$

The mechanical properties (compressive strength, tensile strength, and modulus of elasticity) all increase as functions of the hydration degree. The stiffness and strength properties are zero prior to the percolation of the solid matrix phase, and evolve to their asymptotic values which correspond to the values of the hardened UHPC material. In between these two asymptotes, an interpolation is necessary. Unfortunately, there has been little research on the evolution of strength and stiffness for UHPC. In a first approach, we will adopt interpolation laws developed for ordinary concrete to UHPC, namely Laube's law for strength growth and Byfors' law for stiffness.

4.1.1 Evolution of Strength

It is often found, for ordinary concrete materials [3], that the tensile strength at early ages grows faster than the compressive strength. However, Bernard et al. [4] showed that this effect was due to the presence of large aggregates activating friction in compression (but not in tension). Since UHPC have no large aggregates, it is appropriate, therefore, to adopt one single evolution law for both tensile and compressive strength. As a first engineering approximation for the strength parameters in the UHPC model we adopt a linear relationship known as Laube's Law [14]. If a strength is denoted by $f\left(\xi\right)$, Laube's law has the following form:

$$f\left(\xi\right) = f_\infty k_f\left(\xi\right) \tag{4.6}$$
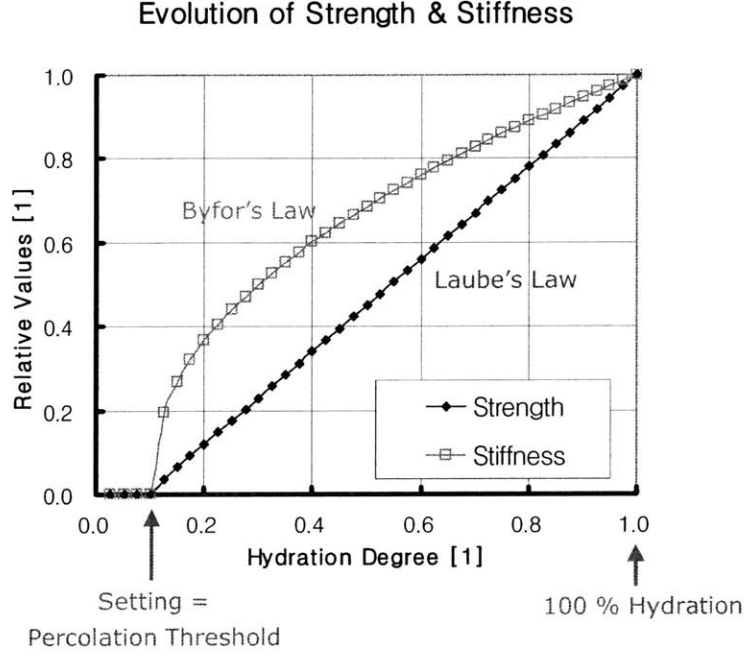
Figure 4-2: Evolution of strength and stiffness adopted in the modeling of UHPC at early-ages.

where f_∞ is the strength of the hardened material, and $k_f(\xi)$ is the aging factor for strength. The aging factor reads:

$$k_f(\xi) = \begin{cases} \frac{\xi_0}{10}\xi & \text{if} \quad \xi \leq \xi_0 \\ \frac{1-\frac{\xi_0}{10}}{1-\xi_0}(\xi - \xi_0) + \frac{\xi_0}{10} & \text{if} \quad \xi > \xi_0 \end{cases} \qquad (4.7)$$

where ξ_0 stands for the percolation threshold. Solid diamonds in Figure 4-2 illustrate Laube's law which we adopt for the strength growth of UHPC at early ages. Significant strength starts to develop only after setting[1].

4.1.2 Evolution of Stiffness

It is generally agreed that Young's modulus increases faster than the compressive and tensile strength [3]. This is due to the change of morphology of the hydration products. This

---

[1] It should be noted that the non-zero value of the strength below the percolation threshold is introduced for stability reason only.

difference between stiffness and strength development is a manifestation of early-age cracking sensitivity, because the generated stress depends on the Young's modulus, whereas the resistance to cracking depends on the tensile strength.

Inspired by developments for ordinary concrete, a nonlinear relationship known as Byfors' law [6] is adopted for the stiffness growth of the UHPC model. If a stiffness is denoted by $C(\xi)$, Byfors' law has the following form:

$$C(\xi) = C_\infty k_c(\xi) \tag{4.8}$$

where C_∞ is the Young's modulus of the hardened material, and $k_c(\xi)$ is the aging factor for the stiffness. The aging factor reads:

$$k_c(\xi) = \frac{1 + 1.37\,[R_{c\infty}]^{2.204}}{1 + 1.37\,[R_c(\xi)]^{2.204}} \left[\frac{R_c(\xi)}{R_{c\infty}}\right]^{2.675} \tag{4.9}$$

where $R_{c\infty}$ is the compressive strength of the hardened material [unit: MPa], and $R_c(\xi)$ is the compressive strength of the aging material as a function of the hydration degree ξ. A bilinear relation is introduced for $R_c(\xi)$ as follows:

$$R_c(\xi) = \begin{cases} \xi R_{c0} & \text{if } \xi \leq \xi_0 \\ \frac{R_{c\infty} - R_{c0}}{1 - \xi_0}(\xi - \xi_0) + R_{c0} & \text{if } \xi > \xi_0 \end{cases} \tag{4.10}$$

where ξ_0 is the threshold of the hardened material and $R_{c0} = \frac{1}{10}\xi_0 R_{c\infty}$. Hollow squares in Figure 4-2 illustrate the adopted evolution law for the stiffness of UHPC at early ages. It is worthwhile to note that significant mechanical properties start to develop only after setting.

4.2 Thermodynamic Framework for UHPC at Early Ages

In the previous section, we introduced some ad-hoc modification to the hardened UHPC material model. At this stage of the development, a closer look on the thermodynamic consistency of the model is in order.

4.2.1 Free Energy and State Equations

Like for the hardened 3-D UHPC (see Section 2.3.1) and the hydration kinetics model (see Section 3.2.2), the starting point of our modeling is the Clausius-Duhem inequality [24]:

$$\varphi dt = \boldsymbol{\Sigma} : d\mathbf{E} - SdT - d\Psi \geq 0 \tag{4.11}$$

where φdt stands for the dissipation; $\boldsymbol{\Sigma}$ and $\mathbf{E}$ are the 2nd order macroscopic stress tensor and macroscopic strain tensor, respectively; S and T stand for the entropy and absolute temperature, respectively; and Ψ is the free energy. Like in the early-age model for ordinary concrete (see Chapter 3), assuming the elementary system as closed, the hydration degree, $\xi(t)$, is considered as an internal state variables [25] [26]. For UHPC at early ages, however, there are five state variables, $\mathbf{E}$, ε_M^p, ε_F^p, T and ξ, which describe the energy state of the system. The free energy is assumed of the form:

$$
\begin{aligned}
\Psi &= \Psi\left(\mathbf{E} - \varepsilon_M^p, \mathbf{E} - \varepsilon_F^p, \varepsilon_M^p - \varepsilon_F^p, T, \xi\right) \\
&= \Psi_0 + \Psi_2 + \Psi_1
\end{aligned} \tag{4.12}
$$

where:

$$\Psi_0 = \boldsymbol{\sigma}_{M,0} : \left(\mathbf{E} - \varepsilon_M^p\right) + \boldsymbol{\sigma}_{F,0} : \left(\mathbf{E} - \varepsilon_F^p\right) - S_0\left(T - T_0\right) - A_0\xi \tag{4.13}$$

$$\Psi_2 = \tfrac{1}{2}\left[\mathbf{E} - \varepsilon_M^p\right] : \mathbb{C}_M\left(\xi\right) : \left[\mathbf{E} - \varepsilon_M^p\right] + \tfrac{1}{2}\left[\mathbf{E} - \varepsilon_F^p\right] : \mathbb{C}_F\left(\xi\right) : \left[\mathbf{E} - \varepsilon_F^p\right]$$
$$+ \tfrac{1}{2}\left[\varepsilon_M^p - \varepsilon_F^p\right] : \mathbb{M}\left(\xi\right) : \left[\varepsilon_M^p - \varepsilon_F^p\right] - \tfrac{1}{2}\tfrac{C}{T_0}\left(T - T_0\right)^2 - \tfrac{1}{2}\kappa\xi^2$$

$$\Psi_1 = -\mathbb{C}_M\left(\xi\right) : \left[\mathbf{E} - \varepsilon_M^p\right] : \boldsymbol{\alpha}_M\left(T - T_0\right) - \mathbb{C}_F\left(\xi\right) : \left[\mathbf{E} - \varepsilon_F^p\right] : \boldsymbol{\alpha}_F\left(T - T_0\right)$$
$$-\mathbb{C}_M\left(\xi\right) : \left[\mathbf{E} - \varepsilon_M^p\right] : \boldsymbol{\beta}_M\xi - \mathbb{C}_F\left(\xi\right) : \left[\mathbf{E} - \varepsilon_F^p\right] : \boldsymbol{\beta}_F\xi + \tfrac{L}{T_0}\xi\left(T - T_0\right)$$

In (4.13), subscript "0" means initial state of each driving force; $\boldsymbol{\sigma}_M$ and $\boldsymbol{\sigma}_F$ stand for the stress of the composite matrix and the composite fiber, respectively[2]; $\mathbb{C}_M\left(\xi\right)$, $\mathbb{C}_F\left(\xi\right)$ and $\mathbb{M}\left(\xi\right)$ are the 4th order stiffness tensors of the composite matrix, the composite fiber, and the matrix-fiber

---

[2] The sum of the matrix stress and the fiber stress is always equal to the macroscopic stress, which holds as well for the initial state of stress:
$$\boldsymbol{\Sigma}_0 = \boldsymbol{\sigma}_{M,0} + \boldsymbol{\sigma}_{F,0}$$

coupling; C is the volume heat capacity; κ is a coefficient relating to the hydration kinetics; α_M and α_F are the 2nd order thermal dilatation coefficient tensors of the composite matrix and the composite fiber; β_M and β_F are the 2nd order chemical dilatation coefficient tensors of the composite matrix and the composite fiber; and L is the latent heat of the hydration reaction. In a first-order engineering approach, the thermal and chemical dilatation coefficient tensors (α_M, α_F, β_M and β_F) are considered to be constant, and the volume heat capacity, the hydration kinetics coefficient and the latent heat (C, κ and L) as well. Use of (4.12) in (4.11) yields the Clausius-Duhem inequality in the form:

$$\varphi dt = \sigma_M : d\varepsilon_M^p + \sigma_F : d\varepsilon_F^p + Ad\xi \geq 0 \tag{4.14}$$

together with the state equations:

$$
\begin{aligned}
\mathbf{\Sigma} &= \frac{\partial \Psi}{\partial \mathbf{E}} \\
&= \mathbf{\Sigma}_0 + \mathbb{C}_M\left(\xi\right) : \left[\mathbf{E} - \varepsilon_M^p\right] + \mathbb{C}_F : \left[\mathbf{E} - \varepsilon_F^p\right] \\
&\quad - \left[\mathbb{C}_M\left(\xi\right) : \alpha_M + \mathbb{C}_F : \alpha_F\right]\left(T - T_0\right) \\
&\quad - \left[\mathbb{C}_M\left(\xi\right) : \beta_M + \mathbb{C}_F : \beta_F\right]\xi
\end{aligned}
\tag{4.15}
$$

$$
\begin{aligned}
\sigma_M &= -\frac{\partial \Psi}{\partial \varepsilon_M^p} \\
&= \sigma_{M,0} + \mathbb{C}_M\left(\xi\right) : \left[\mathbf{E} - \varepsilon_M^p\right] - \mathbb{M}\left(\xi\right) : \left[\varepsilon_M^p - \varepsilon_F^p\right] \\
&\quad - \mathbb{C}_M\left(\xi\right) : \alpha_M\left(T - T_0\right) - \mathbb{C}_M\left(\xi\right) : \beta_M\xi
\end{aligned}
\tag{4.16}
$$

$$
\begin{aligned}
\sigma_F &= -\frac{\partial \Psi}{\partial \varepsilon_F^p} \\
&= \sigma_{F,0} + \mathbb{C}_F : \left[\mathbf{E} - \varepsilon_F^p\right] + \mathbb{M}\left(\xi\right) : \left[\varepsilon_M^p - \varepsilon_F^p\right] \\
&\quad - \mathbb{C}_F : \alpha_F\left(T - T_0\right) - \mathbb{C}_F : \beta_F\xi
\end{aligned}
\tag{4.17}
$$

69

$$S = -\frac{\partial \Psi}{\partial T} \tag{4.18}$$

$$= S_0 + \frac{C}{T_0}(T - T_0) - \frac{L}{T_0}\xi$$

$$+ \mathbb{C}_M(\xi) : \left[\mathbf{E} - \varepsilon_M^p\right] : \alpha_M + \mathbb{C}_F : \left[\mathbf{E} - \varepsilon_F^p\right] : \alpha_F$$

$$A = -\frac{\partial \Psi}{\partial \xi} \tag{4.19}$$

$$= S_0 - \kappa\xi - \frac{L}{T_0}(T - T_0)$$

$$+ \mathbb{C}_M(\xi) : \left[\mathbf{E} - \varepsilon_M^p\right] : \beta_M + \mathbb{C}_F : \left[\mathbf{E} - \varepsilon_F^p\right] : \beta_F$$

From (4.14) to (4.19), we identify σ_M, σ_F and A as the thermodynamic driving forces associated with the dissipation of the energy caused by $d\varepsilon_M^p$, $d\varepsilon_F^p$ and $d\xi$, respectively.

4.2.2 Maxwell Symmetries and Decoupling Hypothesis

One key feature of the thermodynamic approach is that it allows one to account and work out the couplings (or thermodynamic cross-effects) between phenomena of different origin through the Maxwell symmetries that come from the choice of the free energy expression (4.13). These are:

- The coupling between the different stress quantities (Σ, σ_M and σ_F) which characterize the UHPC material model (see Section 2.3.1):

$$\mathbb{C}_M(\xi) = -\frac{\partial \Sigma}{\partial \varepsilon_M^p} = \frac{\partial \sigma_M}{\partial \mathbf{E}}$$

$$\mathbb{C}_F = -\frac{\partial \Sigma}{\partial \varepsilon_F^p} = \frac{\partial \sigma_F}{\partial \mathbf{E}} \tag{4.20}$$

$$\mathbb{M}(\xi) = \frac{\partial \sigma_M}{\partial \varepsilon_F^p} = \frac{\partial \sigma_F}{\partial \varepsilon_M^p}$$

- The coupling between the stresses (Σ, σ_M and σ_F) and the entropy (S) which relate to thermal dilatation and latent deformation heat effects:

$$\alpha_M \mathbb{C}_M(\xi) + \alpha_F \mathbb{C}_F = -\frac{\partial \Sigma}{\partial T} = \frac{\partial S}{\partial E}$$

$$\alpha_M \mathbb{C}_M(\xi) = -\frac{\partial \sigma_M}{\partial T} = -\frac{\partial S}{\partial \varepsilon_M^p} \tag{4.21}$$

$$\alpha_F \mathbb{C}_F = -\frac{\partial \sigma_F}{\partial T} = -\frac{\partial S}{\partial \varepsilon_F^p}$$

- The coupling between the stresses (Σ, σ_M and σ_F) and the chemical affinity (A) which relate to chemical dilatation (or shrinkage) and stress induced phase change phenomena:

$$\beta_M \mathbb{C}_M\left(\xi\right) + \beta_F \mathbb{C}_F = -\frac{\partial \Sigma}{\partial \xi} = \frac{\partial A}{\partial \mathbf{E}}$$
$$\beta_M \mathbb{C}_M\left(\xi\right) = -\frac{\partial \sigma_M}{\partial \xi} = -\frac{\partial A}{\partial \varepsilon_M^p}$$
$$\beta_F \mathbb{C}_F = -\frac{\partial \sigma_F}{\partial \xi} = -\frac{\partial A}{\partial \varepsilon_F^p}$$

(4.22)

- The coupling between the entropy (S) and the chemical affinity (A) which relate to the latent heat of hydration and temperature induced phase change phenomena:

$$\frac{L}{T_0} = -\frac{\partial A}{\partial T} = -\frac{\partial S}{\partial \xi}$$

(4.23)

Using these notations, we obtain the following system of equations:

$$\left\{\begin{array}{c} d\Sigma \\ d\sigma_M \\ d\sigma_F \\ dS \\ dA \end{array}\right\} = [\mathcal{K}_1] : \left\{\begin{array}{c} d\mathbf{E} - d\varepsilon_M^p \\ d\mathbf{E} - d\varepsilon_F^p \\ dT \\ d\xi \end{array}\right\}$$

(4.24)

where:

$$[\mathcal{K}_1] = \begin{bmatrix} \mathbb{C}_M\left(\xi\right) & \mathbb{C}_F & \left\langle\begin{array}{c} -\mathbb{C}_M\left(\xi\right):\alpha_M \\ -\mathbb{C}_F:\alpha_F \end{array}\right\rangle & \left\langle\begin{array}{c} -\mathbb{C}_M\left(\xi\right):\beta_M \\ -\mathbb{C}_F:\beta_F \end{array}\right\rangle \\ \mathbb{C}_M\left(\xi\right)+M\left(\xi\right) & -\mathbb{M}\left(\xi\right) & -\mathbb{C}_M\left(\xi\right):\alpha_M & -\mathbb{C}_M\left(\xi\right):\beta_M \\ -\mathbb{M}\left(\xi\right) & \mathbb{C}_F+\mathbb{M}\left(\xi\right) & -\mathbb{C}_F:\alpha_F & -\mathbb{C}_F:\beta_F \\ \mathbb{C}_M\left(\xi\right):\alpha_M & \mathbb{C}_F:\alpha_F & C/T_0 & -L/T_0 \\ \mathbb{C}_M\left(\xi\right):\beta_M & \mathbb{C}_F:\beta_F & -L/T_0 & \kappa \end{bmatrix}$$

(4.25)

We note that these relations are such that at any time,

$$d\Sigma = d\sigma_M + d\sigma_F$$

(4.26)
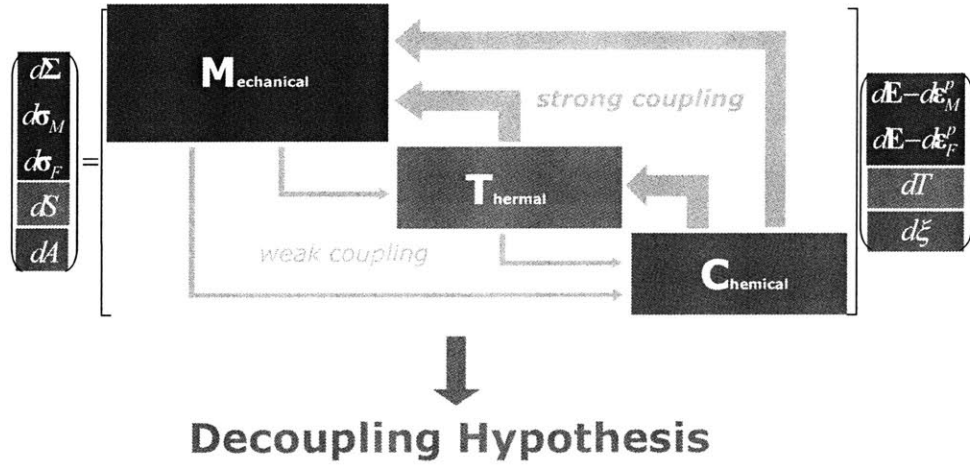
Figure 4-3: Thermo-chemo-mechanical coupling in early-age UHPC and introduction of decoupling hypothesis.

Like for ordinary concrete, some of these couplings are rather weak, while others are strong. In a first engineering approach, we consider only the strong coupling terms, which are situated in the upper off-diagonal region in (4.24). Thermal and chemical changes produce stresses or strains, and the chemical changes produces heat. On the other hand, the coupling terms in the lower off-diagonal region in (4.24) are considered to be weak, because, for concrete materials, the mechanical change has little effect on the thermal and the chemical problem, and the thermal change has little effect on the chemical problem in precipitation reactions. Figure 4-3 illustrates how the decoupling hypothesis is applied to the constitutive relations. Introducing the decoupling hypothesis in (4.24) allows us to obtain the following partially decoupled constitutive relations:

$$
\left\{
\begin{array}{c}
d\Sigma \\
d\sigma_M \\
d\sigma_F \\
dS \\
dA
\end{array}
\right\} = [\mathcal{K}_2] :
\left\{
\begin{array}{c}
d\mathbf{E} - d\varepsilon_M^p \\
d\mathbf{E} - d\varepsilon_F^p \\
dT \\
d\xi
\end{array}
\right\}
\qquad (4.27)
$$

72

where:

$$[\mathcal{K}_2] = \begin{bmatrix} \mathbb{C}_M\left(\xi\right) & \mathbb{C}_F & \left\langle \begin{matrix} -\mathbb{C}_M\left(\xi\right):\alpha_M \\ -\mathbb{C}_F:\alpha_F \} \end{matrix} \right\rangle & \left\langle \begin{matrix} -\mathbb{C}_M\left(\xi\right):\beta_M \\ -\mathbb{C}_F:\beta_F \end{matrix} \right\rangle \\ \mathbb{C}_M\left(\xi\right)+\mathbb{M}\left(\xi\right) & -\mathbb{M}\left(\xi\right) & -\mathbb{C}_M\left(\xi\right):\alpha_M & -\mathbb{C}_M\left(\xi\right):\beta_M \\ -\mathbb{M}\left(\xi\right) & \mathbb{C}_F+\mathbb{M}\left(\xi\right) & -\mathbb{C}_F:\alpha_F & -\mathbb{C}_F:\beta_F \\ 0 & 0 & C/T_0 & -L/T_0 \\ 0 & 0 & 0 & \kappa \end{bmatrix} \tag{4.28}$$

Thus, the equation for affinity A, which enters the hydration kinetics law, depends only on the hydration degree. The equation for entropy S, which enters the heat equation for the thermal problem, depends only on temperature and hydration degree. Only the equations for the stresses (Σ, σ_M and σ_F) depend on all state variables. This will turn out to be the key to the evaluation of the risk of early-age UHPC cracking.

4.2.3 Hydration Kinetics and Heat

Thanks to the decoupling hypothesis, the kinetics of the hydration and the equation of the entropy for the modeling of UHPC early ages have the same form as the ones for ordinary concrete, i.e. (3.15) and (3.19) in Section 3.2.2:

$$dA = -\kappa d\xi \quad \Rightarrow \quad A = A\left(\xi\right) \tag{4.29}$$

$$dS = \frac{C}{T_0}dT - \frac{L}{T_0}d\xi \tag{4.30}$$

Thus, all derivations relating to the thermal and chemical problem for ordinary concrete can be equally applied to the modeling of UHPC at early ages. For instance, the hydration kinetics law reads:

$$\frac{d\xi}{dt} = \frac{A\left(\xi\right)}{\tau\left(T_0\right)}exp\left[-\frac{E_a}{RT}\right] \tag{4.31}$$

and the heat equation reads:

$$C\frac{dT}{dt} = k\nabla^2 T + L\frac{d\xi}{dt} \tag{4.32}$$

In order to complete the macroscopic modeling for UHPC at early ages, we need to perform

73

an experiment through which the hydration kinetics can be accessed as discussed in Section 3.3. Additionally, for the heat equation, thermal boundary conditions need to be defined during the curing process. With these input data, solving simultaneously the hydration kinetics law (4.31) and the heat equation (4.32) yields the time history of temperature and hydration degree in any material or structural system.

4.2.4 The 3-D Early-Age Constitutive Relations

From the partially decoupled constitutive relations (3.14), the constitutive equations for early-age UHPC can be written as follows:

$$
\left\{
\begin{array}{c}
d\mathbf{\Sigma} \\
d\boldsymbol{\sigma}_M \\
d\boldsymbol{\sigma}_F
\end{array}
\right\} = [\mathcal{K}_3] :
\left\{
\begin{array}{c}
d\mathbf{E} - d\boldsymbol{\varepsilon}_M^p \\
d\mathbf{E} - d\boldsymbol{\varepsilon}_F^p \\
dT \\
d\xi
\end{array}
\right\}
\tag{4.33}
$$

where:

$$
[\mathcal{K}_3] =
\begin{bmatrix}
\mathbb{C}_M\left(\xi\right) & \mathbb{C}_F & \left\langle \begin{array}{c} -\mathbb{C}_M\left(\xi\right):\boldsymbol{\alpha}_M \\ -\mathbb{C}_F:\boldsymbol{\alpha}_F \end{array} \right\rangle & \left\langle \begin{array}{c} -\mathbb{C}_M\left(\xi\right):\boldsymbol{\beta}_M \\ -\mathbb{C}_F:\boldsymbol{\beta}_F \end{array} \right\rangle \\
\mathbb{C}_M\left(\xi\right)+\mathbb{M}\left(\xi\right) & -\mathbb{M}\left(\xi\right) & -\mathbb{C}_M\left(\xi\right):\boldsymbol{\alpha}_M & -\mathbb{C}_M\left(\xi\right):\boldsymbol{\beta}_M \\
-\mathbb{M}\left(\xi\right) & \mathbb{C}_F+\mathbb{M}\left(\xi\right) & -\mathbb{C}_F:\boldsymbol{\alpha}_F & -\mathbb{C}_F:\boldsymbol{\beta}_F
\end{bmatrix}
\tag{4.34}
$$

Compared to the hardened UHPC model (see Section 2.3.1), three effects are introduced in (4.33):

- The aging elasticity, $\mathbb{C}_M\left(\xi\right)$ and $\mathbb{M}\left(\xi\right)$, representing the increase of the stiffness as a function of the hydration degree;

- The thermal stresses, $-\mathbb{C}_M\left(\xi\right) : \boldsymbol{\alpha}_M dT - \mathbb{C}_F\left(\xi\right) : \boldsymbol{\alpha}_F dT$, related to restrained thermal dilatation in both matrix and fiber phase;

- The chemical stresses, $-\mathbb{C}_M\left(\xi\right) : \boldsymbol{\beta}_M d\xi - \mathbb{C}_F\left(\xi\right) : \boldsymbol{\beta}_F d\xi$, related to restrained chemical swelling or shrinkage in the composite phases.

74

The general 3-D constitutive model involves 99 (= 3 × 21 + 4 × 9) parameters associated with the evolving stiffness tensors ($\mathbb{C}_M(\xi)$, $\mathbb{C}_F$ and $\mathbb{M}(\xi)$), the thermal dilatation coefficient tensors ($\boldsymbol{\alpha}_M$ and $\boldsymbol{\alpha}_F$), and the chemical dilatation tensor ($\boldsymbol{\beta}_M$ and $\boldsymbol{\beta}_F$). In the isotropic case, the stiffness tensors can be reduced to:

$$\mathbb{C}_M(\xi) = 3K_M(\xi)\mathbb{K} + 2G_M(\xi)\mathbb{J}$$
$$\mathbb{C}_F = 3K_F\mathbb{K} + 2G_F\mathbb{J} \qquad (4.35)$$
$$\mathbb{M}(\xi) = 3K_I(\xi)\mathbb{K} + 2G_I(\xi)\mathbb{J}$$

where $K_M(\xi)$, K_F and $K_I(\xi)$ are the bulk moduli of the composite matrix, the composite fiber and the matrix-fiber coupling, respectively; $G_M(\xi)$, G_F and $G_I(\xi)$ are the evolving shear moduli of the composite matrix, the composite fiber and the matrix-fiber coupling, respectively. The bulk moduli and the shear moduli are related to the elastic moduli of the composite matrix, $C_M(\xi)$, the composite fiber, C_F, and matrix-fiber coupling, $M(\xi)$, by:

$$K_M(\xi) = \frac{C_M(\xi)}{3(1-2\nu_M)}; \quad G_M(\xi) = \frac{C_M(\xi)}{2(1+\nu_M)};$$
$$K_F = \frac{C_F}{3(1-2\nu_F)}; \qquad G_F = \frac{C_F}{2(1+\nu_F)}; \qquad (4.36)$$
$$K_I(\xi) = \frac{M^{3D}(\xi)}{3(1-2\nu_I)}; \qquad G_I = \frac{M^{3D}(\xi)}{2(1+\nu_I)}$$

where ν_M, ν_F and ν_I are the Poisson's ratios of the the composite matrix, the composite fiber and the matrix-fiber coupling, respectively; and $M^{3D}(\xi)$ is the 3-D counterpart[3] of $M(\xi)$ in the 1-D model (see Figure 4-1). The Poisson's ratios are assumed to be constant in the model. Moreover, the isotropy of the material implies:

$$\boldsymbol{\alpha}_M = \alpha_M \mathbf{1}; \quad \boldsymbol{\alpha}_F = \alpha_F \mathbf{1};$$
$$\boldsymbol{\beta}_M = \beta_M \mathbf{1}; \quad \boldsymbol{\beta}_F = \beta_F \mathbf{1} \qquad (4.37)$$

where α_M and β_M are the thermal and the chemical dilatation coefficient of the composite matrix, respectively; and α_F and β_F are the thermal and the chemical dilatation coefficient of the composite fiber, respectively.

---

[3]Unlike the composite matrix stiffness and the composite fiber stiffness, the 3-D coupling stiffness tensor $\mathbb{M}(\xi)$ is not directly related to its 1-D counter part M. The 3-D coupling stiffness tensor must be formulated in such a way that the 3-D model gives the same macroscopic uniaxial response as the 1-D model, as explained in Section 2.3.3.

Equation (2.8) can be restated in the isotropic form:

$$d\mathbf{\Sigma} = d\Sigma^v \mathbf{1} + d\mathbf{\Sigma}^d$$

$$d\boldsymbol{\sigma}_M = d\sigma_M^v \mathbf{1} + d\mathbf{s}_M \tag{4.38}$$

$$d\boldsymbol{\sigma}_F = d\sigma_F^v \mathbf{1} + d\mathbf{s}_F$$

where $d\Sigma^v = \frac{1}{3}tr\,(d\mathbf{\Sigma})$, $d\sigma_M^v = \frac{1}{3}tr\,(d\boldsymbol{\sigma}_M)$ and $d\sigma_F^v = \frac{1}{3}tr\,(d\boldsymbol{\sigma}_F)$ are the volumetric stress increments; $d\mathbf{\Sigma}^d$, $d\mathbf{s}_M$ and $d\mathbf{s}_F$ are the deviatoric stress increments. The volumetric incremental stress-strain relations are represented by:

$$\left\{ \begin{array}{c} d\Sigma^v \\ d\sigma_M^v \\ d\sigma_F^v \end{array} \right\} = 3\,[\mathcal{K}_4] \left\{ \begin{array}{c} dE^v - d\epsilon_M^p \\ dE^v - d\epsilon_F^p \\ dT \\ d\xi \end{array} \right\} \tag{4.39}$$

where:

$$[\mathcal{K}_4] = \left[\begin{array}{cccc} K_M\,(\xi) & K_F & \left\langle \begin{array}{c} -K_M\,(\xi)\,\alpha_M \\ -K_F\alpha_F \end{array} \right\rangle & \left\langle \begin{array}{c} -K_M\,(\xi)\,\beta_M \\ -K_F\beta_F \end{array} \right\rangle \\ K_M\,(\xi) + K_I\,(\xi) & -K_I\,(\xi) & -K_M\,(\xi)\,\alpha_M & -K_M\,(\xi)\,\beta_M \\ -K_I\,(\xi) & K_F + K_I\,(\xi) & -K_F\alpha_F & -K_F\beta_F \end{array} \right] \tag{4.40}$$

In (4.40), $dE^v = \frac{1}{3}tr\,(d\mathbf{E})$, $d\epsilon_M^p = \frac{1}{3}tr\,(d\boldsymbol{\varepsilon}_M^p)$ and $d\epsilon_F^p = \frac{1}{3}tr\,(d\boldsymbol{\varepsilon}_F^p)$ are volumetric strain increments. Similarly, the deviatoric incremental stress-strain relations are given by:

$$\left\{ \begin{array}{c} d\mathbf{\Sigma}^d \\ d\mathbf{s}_M \\ d\mathbf{s}_F \end{array} \right\} = 2 \left[\begin{array}{cccc} G_M\,(\xi) & G_F & 0 & 0 \\ G_M\,(\xi) + G_I\,(\xi) & -G_I\,(\xi) & 0 & 0 \\ -G_I\,(\xi) & G_F + G_I\,(\xi) & 0 & 0 \end{array} \right] : \left\{ \begin{array}{c} d\mathbf{E}^d - d\mathbf{e}_M^p \\ d\mathbf{E}^d - d\mathbf{e}_F^p \\ dT \\ d\xi \end{array} \right\} \tag{4.41}$$

where $d\mathbf{E}^d = d\mathbf{E} - dE^v \mathbf{1}$, $d\mathbf{e}_M^p = d\boldsymbol{\varepsilon}_M^p - d\epsilon_M^p \mathbf{1}$ and $d\mathbf{e}_F^p = d\boldsymbol{\varepsilon}_F^p - d\epsilon_F^p \mathbf{1}$ are deviatoric strain increments.

The constitutive relations (4.39) and (4.41) require as input the time history of the temperature and the hydration degree in the system. With this constitutive relations, the stress equilibrium equation is solved in order to find statically admissible stress fields:

$$div\mathbf{\Sigma} + \rho\mathbf{f} = \mathbf{0} \qquad (4.42)$$

4.2.5 Plasticity of the 3-D Early-Age Model

In order to establish the plastic behavior of the 3-D early-age UHPC model, 3-D loading functions and flow rules need to be constructed.

The 3-D Early-Age Strength Domain

The 3-D strength domain for UHPC at early ages is very similar to that of the hardened UHPC model. In fact, the only difference is that the strength properties of UHPC are now a function of the hydration degree: the 3-D strength domain evolves. Like in the hardened UHPC model (see Section 2.3.2), the early-age UHPC strength domain is also characterized by 6 macroscopic strength values ($\Sigma_{t,1}^{-}(\xi)$, $\Sigma_{c,1}^{-}(\xi)$, $\Sigma_{b,1}^{-}(\xi)$, $\Sigma_{t,2}(\xi)$, $\Sigma_{c,2}(\xi)$ and $\Sigma_{b,2}(\xi)$), which now evolve as the hydration progresses. The evolution of the strength properties are assumed to follow Laube's law explained in Section 4.1.1.

From a modeling point of view, the strength domain $\mathcal{D}_E$ of UHPC, which is described by the 3-D loading function F, is governed by the individual behaviors of the composite matrix and the composite fiber (2.15):

$$\mathbf{\Sigma}(\xi) \in \mathcal{D}_E \quad \Leftrightarrow \quad F = max\left[F_M, \ F_F\right] \leq 0 \quad \Leftrightarrow \quad \left\langle \begin{array}{ccc} \boldsymbol{\sigma}_M(\xi) \in \mathcal{D}_M & \Leftrightarrow & F_M(\boldsymbol{\sigma}_M, \xi) \leq 0 \\ \boldsymbol{\sigma}_F(\xi) \in \mathcal{D}_F & \Leftrightarrow & F_F(\boldsymbol{\sigma}_F, \xi) \leq 0 \end{array} \right\rangle$$
$$(4.43)$$

where the 3-D loading functions (F_M and F_F) are dependent on the hydration degree. More precisely, the 3-D loading function of the composite matrix, F_M, is captured by three higher initial limits ($\sigma_{Mt}(\xi)$, $\sigma_{Mc}(\xi)$ and $\sigma_{Mb}(\xi)$) and three lower yield limits ($\sigma_{Mt}^{cr}(\xi)$, $\sigma_{Mc}^{cr}(\xi)$ and $\sigma_{Mb}^{cr}(\xi)$). For early-age UHPC, we can describe the strength domain of the composite matrix

as follows:

$$\sigma_M(\xi) \in \mathcal{D}_M \quad \Leftrightarrow$$

$$F_M(\sigma_M, \xi) = \left\langle \begin{array}{ll} F_M^0 = max \left[f_M^{TC,0}, \ f_M^{UN,0}, \ f_M^{BI,0} \right] & \text{before cracking} \\ F_M^{cr} = max \left[f_M^{TC,cr}, \ f_M^{UN,cr}, \ f_M^{BI,cr} \right] & \text{after cracking} \end{array} \right\rangle \leq 0 \qquad (4.44)$$

where

$$f_M^{TC,0} = I_{1,M}(\xi) - \sigma_{Mt}(\xi) \leq 0$$

$$f_M^{UN,0} = \alpha_M^{UN}(\xi) I_{1,M}(\xi) + |\mathbf{s}_M(\xi)| - c_M^{UN,0}(\xi) \leq 0 \qquad (4.45)$$

$$f_M^{BI,0} = \alpha_M^{BI}(\xi) I_{1,M}(\xi) + |\mathbf{s}_M(\xi)| - c_M^{BI,0}(\xi) \leq 0$$

$$f_M^{TC,cr} = I_{1,M}(\xi) - \sigma_{Mt}^{cr}(\xi) \leq 0$$

$$f_M^{UN,cr} = \alpha_M^{UN}(\xi) I_{1,M}(\xi) + |\mathbf{s}_M(\xi)| - c_M^{UN,cr}(\xi) \leq 0 \qquad (4.46)$$

$$f_M^{BI,cr} = \alpha_M^{BI}(\xi) I_{1,M}(\xi) + |\mathbf{s}_M(\xi)| - c_M^{BI,cr}(\xi) \leq 0$$

where the friction coefficients (α_i) and the cohesion (c_i) is still defined by (2.18) and (2.21); except for their dependence on the hydration degree.

Furthermore, the 3-D loading function of the composite fiber, F_F, is captured by three characteristic values, i.e. $\sigma_{Ft}(\xi)$, $\sigma_{Fc}(\xi)$ and $\sigma_{Fb}(\xi)$. For early-age UHPC, the strength domain of the composite fiber is described as follows:

$$\sigma_F(\xi) \in \mathcal{D}_F \quad \Leftrightarrow \quad F_F(\sigma_F, \xi) = max \left[f_F^{TC}, \ f_F^{DP} \right] \leq 0 \qquad (4.47)$$

where

$$f_F^{TC} = I_{1,F}(\xi) - \sigma_{Ft}(\xi) \leq 0$$

$$f_F^{DP} = \alpha_F^{UN}(\xi) I(\xi)_{1,F} + |\mathbf{s}_F(\xi)| - c_F^{DP}(\xi) \leq 0 \qquad (4.48)$$

The 3-D Early-Age Plastic Flow Rule

The composite matrix and composite fiber are both governed by the following Kuhn-Tucker conditions:

$$F_M(\sigma_M, \xi) \leq 0; \quad d\lambda_M \geq 0; \quad F_M(\sigma_M, \xi) d\lambda_M = 0 \qquad (4.49)$$

$$F_F(\sigma_F, \xi) \leq 0; \quad d\lambda_F \geq 0; \quad F_F(\sigma_F, \xi) d\lambda_F = 0 \qquad (4.50)$$

78

where $d\lambda_M$ and $d\lambda_F$ are the plastic multipliers that represent the intensity of the plastic flow in the composite matrix and the composite fiber, respectively. Like in the hardened 3-D UHPC model, an associated plastic flow rule is adopted for the 3-D early-age UHPC model. Hence, using (2.29), the permanent deformations of the composite matrix and the composite fiber read:

$$d\varepsilon_M^p = \sum_i d\lambda_{M,i} \frac{\partial F_{M,i}\left(\boldsymbol{\sigma}_M, \xi\right)}{\partial \boldsymbol{\sigma}_M} \tag{4.51}$$
$$= d\lambda_M^{TC}\mathbf{1} + d\lambda_M^{UN}\left[\alpha_M^{UN}\mathbf{1} + \mathbf{N}_{\mathbf{s}_M}\left(\xi\right)\right] + d\lambda_M^{BI}\left[\alpha_M^{BI}\mathbf{1} + \mathbf{N}_{\mathbf{s}_M}\left(\xi\right)\right]$$

$$d\varepsilon_F^p = \sum_i d\lambda_{F,i}\left(\xi\right) \frac{\partial F_{F,i}\left(\boldsymbol{\sigma}_F, \xi\right)}{\partial \boldsymbol{\sigma}_F} \tag{4.52}$$
$$= d\lambda_F^{TC}\mathbf{1} + d\lambda_F^{DP}\left[\alpha_F^{UN}\mathbf{1} + \mathbf{N}_{\mathbf{s}_F}\left(\xi\right)\right]$$

where the loading functions of the composite matrix are still defined in Table 2.1; $\mathbf{N}_{\mathbf{s}_M} = \frac{\mathbf{s}_M}{|\mathbf{s}_M|}$ and $\mathbf{N}_{\mathbf{s}_F} = \frac{\mathbf{s}_F}{|\mathbf{s}_F|}$ are the normalized deviatoric stress tensor of the composite matrix and the composite fiber, respectively.

4.2.6   Consistency with the 1-D Model

In a last step of our constitutive developments, we need to ensure the consistency of the 3-D model with the 1-D model response. By introducing the same Poisson's ratio for all components $(\nu_M = \nu_F = \nu_I \equiv \nu)$ in the 3-D model and assuming the Poisson's ratio does not change during hydration, the consistency with the 1-D model is ensured by the following 3-D coupling modulus:

$$M^{3D}\left(\xi\right) = \beta\left(\xi\right) M\left(\xi\right) + \left[\beta\left(\xi\right) - 1\right]\frac{C_M\left(\xi\right) C_F}{C_M\left(\xi\right) + C_F} \tag{4.53}$$

where

$$\beta\left(\xi\right) = \frac{\left[\alpha_M^{UN}\left(\xi\right) + \sqrt{2/3}\right]^2\left(1 - \nu\right)\left(1 + \nu\right)}{3\left[\alpha_M^{UN}\left(\xi\right)\right]^2\left(1 + \nu\right) + \left(1 - 2\nu\right)} \tag{4.54}$$

Like other stiffness values, the evolution of the coupling modulus is assumed to follow Byfors' Law (see Section 4.1.2).

Based on the reasoning explored in Section 2.3.3, a uniaxial stress-strain output from the

3-D early-age UHPC model can now be obtained with the hydration degree as parameter. The noteworthy four stress-strain points in the $E_{xx} - \Sigma_{xx}$ curve are functions of the hydration degree:

$$\left(E_{xx,1}\left(\xi\right),\ \Sigma_{xx,1}^{-}\left(\xi\right)\right) = \left.\left(E_{xx},\ \Sigma_{xx}\right)\right|_{\Sigma_{xx}(\xi)=\sigma_{Mt}(\xi),\ \Sigma_{yy}(\xi)=0} \tag{4.55}$$

$$\left(E_{xx,1}\left(\xi\right),\ \Sigma_{xx,1}^{+}\left(\xi\right)\right) = \left(\left.E_{xx}\right|_{\Sigma_{xx}(\xi)=\sigma_{Mt}(\xi),\ \Sigma_{yy}(\xi)=0},\ \left.\Sigma_{xx}\right|_{\Sigma_{xx}=\sigma_{Mt}^{cr}(\xi)}\right) \tag{4.56}$$

$$\left(E_{xx,2A}\left(\xi\right),\ \Sigma_{xx,2A}\left(\xi\right)\right) = \left.\left(E_{xx},\ \Sigma_{xx}\right)\right|_{\Sigma_{yy}(\xi)=0,\ f_M^{UN,cr}(\xi)=0,\ f_F^{TC}(\xi)=0} \tag{4.57}$$

$$
\begin{aligned}
\left(E_{xx,2B}\left(\xi\right),\ \Sigma_{xx,2}\left(\xi\right)\right) &= \left.\left(E_{xx},\ \Sigma_{xx}\right)\right|_{\substack{\Sigma_{yy}=0,\ f_M^{TC,cr}(\xi)=0,\\ f_M^{UN,cr}(\xi)=0,\ f_F^{TC}(\xi)=0}} \\[2mm]
&= \left(\left.E_{xx}\right|_{\substack{\Sigma_{yy}(\xi)=0,\ f_M^{TC,cr}(\xi)=0,\\ f_M^{UN,cr}(\xi)=0,\ f_F^{TC}(\xi)=0}},\ \left.\Sigma_{xx}\right|_{\Sigma_{xx}(\xi)=\sigma_{Mt}^{cr}(\xi)+\sigma_{Ft}(\xi)}\right)
\end{aligned} \tag{4.58}
$$

Following the procedure used to derive (2.38)-(2.49) for hardened UHPC, the above equations lead to an analytical solution for the four points. Similarly, the evolving stiffness is obtained analytically:

$$K_0\left(\xi\right) = \left.\frac{\partial\Sigma_{xx}}{\partial E_{xx}}\right|_{\Sigma_{yy}(\xi)=0} \tag{4.59}$$

$$K_1\left(\xi\right) = \left.\frac{\partial\Sigma_{xx}}{\partial E_{xx}}\right|_{\Sigma_{yy}(\xi)=0,\ f_M^{UN}(\xi)=0} \tag{4.60}$$

$$K_{2A}\left(\xi\right) = \left.\frac{\partial\Sigma_{xx}}{\partial E_{xx}}\right|_{\Sigma_{yy}(\xi)=0,\ f_M^{UN}(\xi)=0,\ f_F^{TC}(\xi)=0} \tag{4.61}$$

These three stiffness values for the early-age UHPC model can be computed using a similar approach as the one employed to derive (2.50)-(2.57) for the hardened UHPC model.

Figure 4-4 displays the analytical solutions for different hydration degrees[4]. We can clearly see the evolution of the stiffness and strength as the hydration progresses. These analytical results will be used later on for verification purposes of the model implementation in a finite element environment.

---

[4]The material properties of Ductal^{TM}-Steel Fiber are used for the model parameters of the hardened UHPC material, as listed in Table 2.4. In order to see the evolution of the material properties, four cases of hydration degree are considered, i.e. $\xi = 0.25, 0.5, 0.75$ and 1.0.
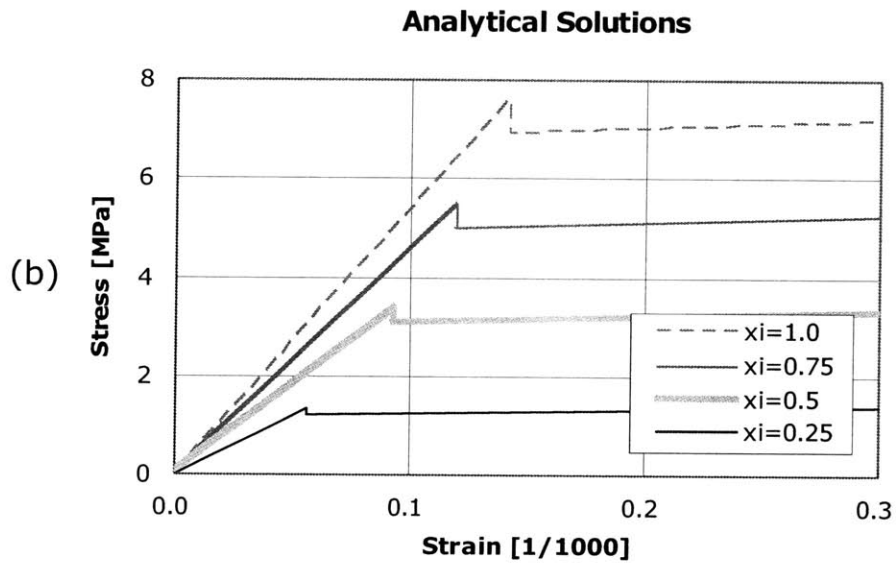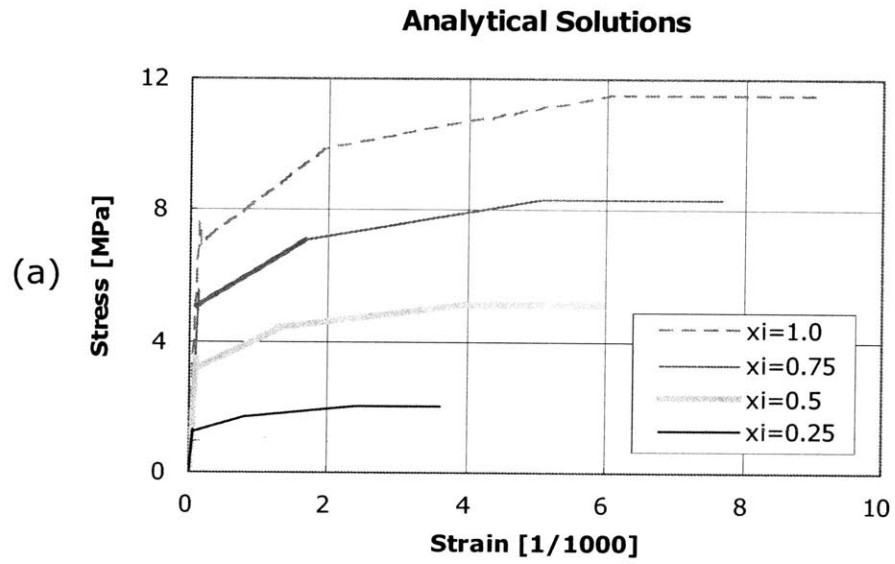
Figure 4-4: Uniaxial stress-strain behavior obtained from the analytical solution: (a) Entire stress-strain curve, (b) Focus on first cracking behavior.

4.3 Chapter Summary

The thermo-chemo-mechanical coupling model of UHPC is the combination of the two-phase mechanical model of hardened UHPC and the thermo-chemo-mechanical coupling model for ordinary early-age concrete. The coupling of these two model is achieved by considering the evolution of the strength and stiffness properties in the two-phase UHPC material model. As a first engineering approach, a linear evolution law [Laube's law] is adopted for strength, and stiffness is assumed to follow a nonlinear evolution law [Byfors' law]. The couplings [thermodynamic cross-effects] between phenomena of different origin are investigated through the Maxwell symmetries that come from the choice of the free energy expression. Like in the ordinary concrete constitutive relations, it is assumed that the thermodynamic imbalance induced by stress, temperature and plastic evolutions are negligible for the hydration reaction. Finally, The 3-D macroscopic model for UHPC at early ages is constructed in three steps:

- Determination of the 3-D constitutive relations: The 3-D stress-strain relations are obtained using thermodynamic approach.

- Determination of strength domain and plastic deformation of the 3-D model: The 3-D strength limits evolve as the hydration progresses. Thus, the 3-D loading functions depend on the hydration degree. Like for the hardened UHPC model, an associated plastic flow rule is adopted.

- Consistency of the 3-D model with the 1-D model: The 3-D model is designed to give consistent results with the 1-D model; and this over the entire hydration process.

Chapter 5

FINITE ELEMENT

IMPLEMENTATION

The finite element implementation of the early-age UHPC model represents the link between material modeling and structural application. With the finite element implementation of the early-age UHPC model, one can simulate structural behavior composed of UHPC at early ages. In this Chapter, the finite element formulation and the realization of the model is discussed. While the thermo-chemical model does not differ much from the one available for ordinary concrete, and is implemented in several finite element programs, the contribution of this research is formulation and implementation of the thermo-chemo-mechanical model. This chapter presents details on the finite element implementation of the early-age UHPC model in a commercial finite element program, CESAR-LCPC. Moreover, in order to verify the newly implemented module, uniaxial responses of an early-age UHPC element are compared with the analytical solutions developed in Chapter 4.

5.1 Finite Element Formulation

Thanks to the decoupling hypothesis, the simulations can be carried out in a two-step manner. First, the thermo-chemical problem is solved. The results are used as input in the thermo-chemo-mechanical problem to determine deflection, stress, etc.

5.1.1 Principle of Virtual Displacements

The mechanical finite element analysis problem for early-age UHPC can be stated as follows:

$$
Given \begin{cases} \text{Geometry of Body} \\ \text{Force Boundary Condition: } \mathbf{f}^d \text{ and } \mathbf{T}^d \\ \text{Displacement Boundary Condition: } \boldsymbol{\xi}^d \\ \text{Material Stress-strain Law} \\ \text{Temperature and Hydration Degree History: } T\left(\mathbf{x},t\right) \text{ and } \xi\left(\mathbf{x},t\right) \end{cases}
$$

$$
Calculate \begin{cases} \text{Displacements: } \boldsymbol{\xi} \\ \text{The Corresponding Strains: } \mathbf{E}, \varepsilon_M^p \text{ and } \varepsilon_F^p \\ \text{The Corresponding Stress: } \boldsymbol{\Sigma}, \boldsymbol{\sigma}_M \text{ and } \boldsymbol{\sigma}_F \end{cases}
$$

where $\mathbf{f}$ is the volume force density; $\mathbf{T}$ is the surface force density; $\boldsymbol{\xi}$ is the displacement; the superscript "d" indicate the prescribed quantities; and $\boldsymbol{\Sigma}$ and $\mathbf{E}$ are the macroscopic stress and strain tensor, respectively[1]. In order to close the above boundary value problem, the following three conditions must be satisfied:

- Stress Equilibrium:

$$
div\boldsymbol{\Sigma} + \rho\mathbf{f} = \mathbf{0} \tag{5.1}
$$

where ρ is the mass density. In the case of the UHPC model, it should be noted that only the macroscopic stress $\boldsymbol{\Sigma}$ enters the stress equilibrium equation. By contrast, the values of the stresses in the individual components ($\boldsymbol{\sigma}_M$ and $\boldsymbol{\sigma}_F$) are dictated by their state equations (4.33).

- Geometrical Compatibility (strain-displacement relation):

$$
\mathbf{E} = \frac{1}{2}\left(grad\boldsymbol{\xi} + grad\boldsymbol{\xi}^T\right) \tag{5.2}
$$

---

[1]Dimensions of the quantities are followings:

$$
[\mathbf{f}] = FM^{-1} = LT^{-2}; \quad [\mathbf{T}] = FL^{-2} = ML^{-1}T^{-2}
$$

This equation can be obtained from the infinitesimal deformation assumption.

- Material Law (constitutive relation and plastic evolution law):

$$\mathbf{\Sigma} = \mathbf{\Sigma}\left(\mathbf{E}, \ ...\right) \tag{5.3}$$

For the early-age UHPC, the constitutive relation is given by (4.33), and the plastic evolution law by (4.43).

The basis of the displacement-based finite element solution is the principle of virtual displacements. This principle states that the total internal virtual work be equal to the total external virtual work, for any compatible small virtual displacements imposed on the system. The principle reads [2]:

$$
\begin{aligned}
\bar{\mathcal{W}}_{int} &= \int_{\Omega} \bar{\mathbf{E}} : \mathbf{\Sigma} d\Omega \\
&= \int_{\Omega} \bar{\boldsymbol{\xi}} \cdot \rho \mathbf{f} d\Omega + \int_{\partial\Omega} \bar{\boldsymbol{\xi}} \cdot \mathbf{T} da = \bar{\mathcal{W}}_{ext}
\end{aligned}
\tag{5.4}
$$

where $\bar{\mathcal{W}}_{int}$ and $\bar{\mathcal{W}}_{ext}$ are the internal and external virtual work, respectively; $\bar{\boldsymbol{\xi}}$ is the virtual displacement; and $\bar{\mathbf{E}}$ is the corresponding virtual strain (the over-bar denoting virtual quantities). The equation in the first row represents the virtual work of the internal stress, and the equation in the second row expresses the virtual work done by the external forces (volume and surface forces).

5.1.2 Finite Element Equations

Finite element analysis requires the spacial discretization of the system to be analyzed. The entire system is approximated as an assemblage of discrete finite elements inter-connected at nodal points on the element boundaries. For an element k, the displacement field $\boldsymbol{\xi}^k\left(\mathbf{x}\right)$ is assumed to be a function of the *unknown global displacements at the nodes* $\{U\}$:

$$\boldsymbol{\xi}^k\left(\mathbf{x}\right) = \left[N^k\right]\{U\} \tag{5.5}$$

where $\left[N^k\right]$ is the displacement interpolation matrix for the element k, and the superscript "k" denotes the element number[2]. The choice of element and the construction of the corresponding entries in $\left[N^k\right]$ constitute the basic steps of a finite element solution. From the assumption of the displacement field in (5.5), the corresponding macroscopic strain for the element k is expressed by:

$$\mathbf{E}^k\left(\mathbf{x}\right) = \left[B^k\right]\left\{U\right\}\tag{5.6}$$

where $\left[B^k\left(\mathbf{x}\right)\right]$ is the strain-displacement matrix[3] for the element k.

For the use of the principle of virtual displacements, the same assumptions are applied to the virtual displacements and the macroscopic strains for element k:

$$\bar{\xi}^k = \left[N^k\right]\left\{\bar{U}\right\}\tag{5.7}$$

$$\bar{\mathbf{E}}^k = \left[B^k\right]\left\{\bar{U}\right\}\tag{5.8}$$

---

[2]Here, we express symmetric 2nd and 4th order tensors in matrix form. For example, the 2nd order strain tensor (3×3) is expressed in a 6×1 vector form:

$$\mathbf{E} = \begin{bmatrix} E_{xx} & E_{xy} & E_{xz} \\ E_{xy} & E_{yy} & E_{yz} \\ E_{xz} & E_{yz} & E_{zz} \end{bmatrix} \rightarrow \mathbf{E} = \begin{bmatrix} E_{xx} & E_{yy} & E_{zz} & E_{xy} & E_{xz} & E_{yz} \end{bmatrix}^T$$

By adopting this notation, we can express the following quantities in matrix form:

$$\xi \Rightarrow n \times 1; \quad \left[N^k\right] \Rightarrow n \times m; \quad \left\{U\right\} \Rightarrow m \times 1$$

where n is the dimension of the problem, and m is the total number of degree of freedom of the considered element.

[3]The strain-displacement matrix for the element k is given by:

$$\left[B^k\left(\mathbf{x}\right)\right] = \frac{\left[N^k\left(\mathbf{x}\right)\right]}{d\mathbf{x}}$$

By adopting the condensed matrix notation for symmetric tensors, we express the following quantities in matrix form:

$$\mathbf{E} \Rightarrow 2n \times 1; \quad \left[B^k\right] \Rightarrow 2n \times m$$

where n is the dimension of the problem, and m is the total number of degree of freedom of the considered element.

Substitution of the previous relations into (5.4) yields:

$$\bar{\mathcal{W}}_{int} = \sum_k \int_{\Omega^k} \{\bar{U}\}^T \left[B^k\right]^T \Sigma^k d\Omega^k \tag{5.9}$$

$$= \sum_k \int_{\Omega^k} \{\bar{U}\}^T \left[N^k\right]^T \rho \mathbf{f}^k d\Omega^k + \sum_k \int_{\partial\Omega^k} \{\bar{U}\}^T \left[N^k\right]^T \mathbf{T}^k d\left(\partial\Omega^k\right) = \bar{\mathcal{W}}_{ext}$$

By introducing new notations for internal and external forces at the nodes ($\{F_{int}\}$ and $\{F_{ext}\}$), this equation can be simplified as follows:

$$\bar{\mathcal{W}}_{int} = \{\bar{U}\}^T \{F_{int}\} = \{\bar{U}\}^T \{F_{ext}\} = \bar{\mathcal{W}}_{ext} \tag{5.10}$$

where

$$\begin{aligned} \{F_{int}\} &= \sum_k \int_{\Omega^k} \left[B^k\right]^T \Sigma^k d\Omega^k \\ \{F_{ext}\} &= \sum_k \int_{\Omega^k} \left[N^k\right]^T \rho \mathbf{f}^k d\Omega^k + \sum_k \int_{\partial\Omega^k} \left[N^k\right]^T \mathbf{T}^k d\left(\partial\Omega^k\right) \end{aligned} \tag{5.11}$$

Since (5.10) must hold for any value of the virtual displacement $\{\bar{U}\}^T$, we obtain:

$$\{R\} = \{F_{ext}\} - \{F_{int}\} = \mathbf{0} \tag{5.12}$$

where $\{R\}$ is the residual force vector for the global force equilibrium.

For a nonlinear material law, an iteration procedure is required to solve the above equation until the residual force vector is close to zero. In this study, the Newton-Raphson method is adopted:

$$\begin{aligned} \left\{F_{int}^{(i)}\right\} &= \left\{F_{int}^{(i-1)}\right\} + \frac{\partial\left\{F_{int}^{(i-1)}\right\}}{\partial\left\{U^{(i)}\right\}} \left\{\Delta U^{(i)}\right\} \\ &= \left\{F_{int}^{(i-1)}\right\} + \left\langle \sum_k \int_{\Omega^k} \left[B^k\right]^T \left(\frac{\partial\Sigma}{\partial\mathbf{E}}\right)^{k,(i)} \left[B^k\right] d\Omega^k \right\rangle \left\{\Delta U^{(i)}\right\} \\ &= \left\{F_{int}^{(i-1)}\right\} + \left[K^{(i)}\left(\xi\right)\right] \left\{\Delta U^{(i)}\right\} \end{aligned} \tag{5.13}$$

where (i) is the number of the iteration step in the Newton-Raphson method; $\Delta U^{(i)} = U^{(i)} - U^{(i-1)}$ is the corresponding incremental residual displacement; and $\left[K^{(i)}\left(\xi\right)\right]$ is the correspond-

ing stiffness matrix of the element assemblage which is now a function of the eventually spatially varying hydration degree. From (5.12) and (5.13), the unknown incremental residual displacements $\left\{\Delta U^{(i)}\right\}$ are calculated at each iteration using the residual force vector $\left\{R^{(i-1)}\right\}$:

$$\left[K^{(i)}\left(\xi\right)\right]\left\{\Delta U^{(i)}\right\} = \{F_{ext}\} - \left\{F_{int}^{(i-1)}\right\} = \left\{R^{(i-1)}\right\} \tag{5.14}$$

Based on this iteration scheme, the *unknown displacement* $\{U\}$ can be obtained for a nonlinear material law.

The iteration procedure, however, is not necessary for elastic behavior. From (4.33), $\left(\frac{\partial \Sigma}{\partial E}\right)^{k,(i)}$ is equal to the sum of the 4th order stiffness tensors for the composite matrix and the composite fiber:

$$\left(\frac{\partial \Sigma}{\partial E}\right)^{k,(i)} = \mathbb{C}_M^k\left(\xi^k\right) + \mathbb{C}_F^k \tag{5.15}$$

Thus, $\left\{\Delta U^{(i)}\right\}$ can be easily obtained for elastic behavior from (5.14), using the following explicit equation of $\left[K^{(i)}\left(\xi\right)\right]$:

$$\left[K^{(i)}\left(\xi\right)\right] = \sum_k \int_{\Omega^k} \left[B^k\right]^T \left\langle \mathbb{C}_M^k\left(\xi^k\right) + \mathbb{C}_F^k \right\rangle \left[B^k\left(\mathbf{x}\right)\right] d\Omega^k \tag{5.16}$$

Following the previously described iteration scheme, the unknown displacement $\{U\} = \left\{\Delta U^{(1)}\right\}$ is obtained at the first iteration step for elastic behavior[4].

Solving the finite element equation for plastic behavior requires some special care to obtain the stiffness matrix $\left[K^{(i)}\left(\xi\right)\right]$ and the internal nodal force at nodes $\left\{F_{int}^{(i)}\right\}$. First, it is not as straightforward to obtain $\left[K^{(i)}\left(\xi\right)\right]$ for plastic behavior as it is for linear elastic behavior, because it requires to calculate a tangent operator between two consecutive iterative stress states. Generally, there are two ways to obtain $\left(\frac{\partial \Sigma}{\partial E}\right)^{k,(i)}$: one is to use the initial tangent operator, i.e. (5.15), and the other is to use consistent tangent operators [22]. In this study the former method is used for simplicity of the formulation. Furthermore, in order to calculate the

---

[4] At the first iteratation step ($i = 1$), the internal force at the nodes is zero:

$$\left\{F_{int}^{(0)}\right\} = \mathbf{0}$$

internal force $\left\{F_{int}^{(i)}\right\}$ at nodes according to (5.11), the plastically admissible macroscopic stress $\Sigma^{k,(i)}$ is required. These stresses are calculated in an iterative fashion from the infinitesimal state equation (4.33) written in an incremental form:

$$
\begin{aligned}
\Sigma^{k,(i)} \;=\; & \Sigma^{k,(i-1)} \\
& +\mathbb{C}_M^k\left(\xi^k\right) : \left[\Delta\mathbf{E}^{k,(i)} - \Delta\varepsilon_M^{p,k,(i)}\right] + \mathbb{C}_F^k : \left[\Delta\mathbf{E}^{k,(i)} - \Delta\varepsilon_F^{p,k,(i)}\right] \\
& - \left[\mathbb{C}_M^k\left(\xi^k\right) : \alpha_M^k + \mathbb{C}_F^k : \alpha_F^k\right]\Delta T^k - \left[\mathbb{C}_M^k\left(\xi^k\right) : \beta_M^k + \mathbb{C}_F^k : \beta_F^k\right]\Delta\xi^k
\end{aligned}
\tag{5.17}
$$

where $\Delta\mathbf{E}^{k,(i)} = \left[B^k\right]\left\{\Delta U^{(i)}\right\}$; ΔT^k and $\Delta\xi^k$ are obtained at each time step from the thermo-chemical finite element analysis; and $\Delta\varepsilon_M^{p,k,(i-1)}$ and $\Delta\varepsilon_M^{p,k,(i-1)}$ can be obtained from a return mapping algorithm. This return mapping algorithm is discussed in the following section.

5.1.3 Return Mapping Algorithm

An implicit backward Euler difference scheme is adopted as the return mapping algorithm in order to obtain the plastically admissible macroscopic stress Σ for a given set of material parameters and strain history. The return mapping algorithm applies the state and evolution equations of the constitutive model in a spatially discretized form through an iterative procedure [22]. With this procedure, the two-phase and multi-loading surface problem of early-age UHPC reduces to the standard problem of finding the closest distance of the trial stress state to the elastic domain. Within a finite element procedure, this algorithm discretizes the constitutive models at the level of the integration points.

The implementation of the 3-D early-age UHPC model requires us to consider simultaneously the five different loading surfaces[5] given by (4.44) and (4.47). The return mapping algorithm presented in this section applies to the general 3-D case. However, this method is

---

[5] Before cracking, the five loading functions are:

$$f_M^{TC,0},\ f_M^{UN,0}\ \text{and}\ f_M^{BI,0} \qquad \text{for the composite matrix}$$
$$f_F^{TC}\ \text{and}\ f_F^{DP} \qquad\qquad \text{for the composite fiber}$$

After cracking, those are:

$$f_M^{TC,cr},\ f_M^{UN,cr}\ \text{and}\ f_M^{BI,cr} \qquad \text{for the composite matrix}$$
$$f_F^{TC}\ \text{and}\ f_F^{DP} \qquad\qquad \text{for the composite fiber}$$

easily adapted for uniaxial, biaxial and plane stress condition; and Reference [7] provides details of these conditions.

Before entering the details of the return mapping algorithm, we summarize the quantities that are given as input for the algorithm. These are:

- The thermo-chemical state variables (T^k and ξ^k) and their incremental values (ΔT^k and $\Delta \xi^k$) which are obtained from the thermo-chemical finite element analysis at each time step, and each point in the structure.

- The incremental displacement $\Delta U^{(i)}$ which is obtained from the (modified) Newton-Raphson scheme:

$$\left[K^{(0)}\left(\xi\right) \right] \left\{ \Delta U^{(i)} \right\} = \{F_{ext}\} - \left\{ F_{int}^{(i-1)} \right\} = \left\{ R^{(i-1)} \right\} \qquad (5.18)$$

where $\left[K^{(0)}\left(\xi\right) \right]$ is the elastic stiffness matrix of the element assemblage calculated at the beginning of each time step (during the time step iterations the hydration does not evolve).

- The incremental macroscopic strain which is calculated from the given incremental residual displacement; analogous to (5.6):

$$\Delta \mathbf{E}^{k,(i)} = \left[B^k \right] \left\{ \Delta U^{(i)} \right\} \qquad (5.19)$$

Strictly speaking, all state variables of the system and the cracking variable have to include a superscript (i) for the iteration number of the Newton-Raphson scheme. Furthermore, another superscript k for elements has to be included. However, they are omitted for simplicity of the notation in this section. This is because the whole return mapping algorithm is carried out at the integration point of each element and for each iteration of the Newton-Raphson scheme, and notations are repetitive. The following simplified notation will be used:

$$\Delta T^k \Rightarrow \Delta T; \quad \Delta \xi^k \Rightarrow \Delta \xi; \quad \Delta \mathbf{E}^{k,(i)} \Rightarrow \Delta \mathbf{E}; \qquad (5.20)$$

$$\boldsymbol{\Sigma}^{k,(i-1)} \Rightarrow \boldsymbol{\Sigma}_{in}; \quad \boldsymbol{\sigma}_M^{k,(i-1)} \Rightarrow \boldsymbol{\sigma}_{M,in}; \quad \boldsymbol{\sigma}_F^{k,(i-1)} \Rightarrow \boldsymbol{\sigma}_{M,in};$$
$$\mathbf{E}^{k,(i-1)} \Rightarrow \mathbf{E}_{in}; \quad \varepsilon_M^{p,k,(i-1)} \Rightarrow \varepsilon_{M,in}^p; \quad \varepsilon_F^{p,k,(i-1)} \Rightarrow \varepsilon_{F,in}^p; \quad \chi^{k,(i-1)} \Rightarrow \chi_{in} \tag{5.21}$$

$$\boldsymbol{\Sigma}^{k,(i)} \Rightarrow \boldsymbol{\Sigma}_{out}; \quad \boldsymbol{\sigma}_M^{k,(i)} \Rightarrow \boldsymbol{\sigma}_{M,out}; \quad \boldsymbol{\sigma}_F^{k,(i)} \Rightarrow \boldsymbol{\sigma}_{M,out};$$
$$\mathbf{E}^{k,(i)} \Rightarrow \mathbf{E}_{out}; \quad \varepsilon_M^{p,k,(i)} \Rightarrow \varepsilon_{M,out}^p; \quad \varepsilon_F^{p,k,(i)} \Rightarrow \varepsilon_{F,out}^p; \quad \chi^{k,(i)} \Rightarrow \chi_{out} \tag{5.22}$$

where the subscript "in" indicates the input quantities, which correspond to a plastically admissible stress field of the previous Newton-Raphson iteration $(i-1)$ *before* considering the incremental macroscopic strain $\Delta\mathbf{E}$; and the the subscript "out" indicates the output quantities, which correspond to a plastically admissible stress field of the current Newton-Raphson iteration (i) *after* considering the incremental macroscopic strain $\Delta\mathbf{E}$.

The 3-D return mapping algorithm assumes that the rest of the thermodynamic state variables of the system ($\mathbf{E} - \varepsilon_M^p$ and $\mathbf{E} - \varepsilon_F^p$) and a cracking state variable (χ) are also known inputs of the return mapping algorithm:

$$\left(\mathbf{E} - \varepsilon_M^p, \ \mathbf{E} - \varepsilon_F^p, \ \chi\right)|_{in} = \left(\mathbf{E}_{in} - \varepsilon_{M,in}^p, \ \mathbf{E}_{in} - \varepsilon_{F,in}^p, \ \chi_{in}\right)$$

where the cracking state variable indicates the cracking condition in the composite matrix. It is defined as follows:

$$\chi_{in} = Y\left(\left|\varepsilon_M^p\right|\right) \tag{5.23}$$

where $\left|\varepsilon_M^p\right|$ is the magnitude of the plastic strain tensor of the composite matrix; and $Y(x_h)$ is the Heaviside function defined by:

$$Y(x_h) = \begin{cases} 0 & \text{if } x_h \le 0 \\ 1 & \text{if } x_h > 0 \end{cases} \tag{5.24}$$

Here, only two composite matrix cracking states are modeled: $\chi = 0$ if the composite matrix has not cracked, $\chi = 1$ if the composite matrix has cracked.

Given the incremental values of the thermodynamic state variables (ΔT and $\Delta \xi$), the return mapping algorithm provides the updated state variables and cracking variable:

$$\left(\mathbf{E} - \varepsilon_M^p, \ \mathbf{E} - \varepsilon_F^p, \ \chi\right)|_{out} = \left(\mathbf{E}_{out} - \varepsilon_{M,out}^p, \ \mathbf{E}_{out} - \varepsilon_{F,out}^p, \ \chi_{out}\right)$$

91

Thus, the 3-D early-age UHPC constitutive equations and plastic evolution equations are discretized with respect to iteration steps of the Newton-Raphson method. Based on these discretized constitutive relations, the return mapping algorithm can be broken down in the following four steps:

1. Compute trial values.

2. Check yield conditions. If $F \leq 0$, go to Step 4. Otherwise, proceed to Step 3.

3. Solve for the plastic strains. Then, go to Step 2.

4. Update the stresses.

The 3-D early-age UHPC model may require multiple iterations checking the yield conditions (Step 2) and solving the plastic strains (Step 3).

Step 1: Compute Trial Values.

We first assume that the imposed incremental macroscopic strain $\Delta \mathbf{E}$ affects the stresses elastically. Then, the trial stresses in the composite matrix and in the composite fiber are calculated from (4.38)-(4.41) in an incremental fashion:

$$
\begin{aligned}
\boldsymbol{\sigma}_{M,tr} &= \boldsymbol{\sigma}_{M,in} + 3K_M \left[\Delta E^v - \alpha_M \Delta T - \beta_M \Delta \xi\right] \mathbf{1} + 2G_M \Delta \mathbf{E}^d \\
\boldsymbol{\sigma}_{F,tr} &= \boldsymbol{\sigma}_{F,in} + 3K_F \left[\Delta E^v - \alpha_F \Delta T - \beta_F \Delta \xi\right] \mathbf{1} + 2G_F \Delta \mathbf{E}^d
\end{aligned}
\tag{5.25}
$$

The trial stresses ($\boldsymbol{\sigma}_{M,tr}$ and $\boldsymbol{\sigma}_{F,tr}$) are *not* guaranteed to be plastically admissible. These trial stresses are calculated from the stresses of the previous step ($\boldsymbol{\sigma}_{M,in}$ and $\boldsymbol{\sigma}_{F,in}$) for given incremental values of the thermodynamic state variables (ΔT and $\Delta \xi$) and the incremental macroscopic strain ($\Delta \mathbf{E}$).

As a first step, these elastically assumed trial stresses are temporarily considered as the updated solutions:

$$
\boldsymbol{\sigma}_{M,up} = \boldsymbol{\sigma}_{M,tr}; \quad \boldsymbol{\sigma}_{F,up} = \boldsymbol{\sigma}_{F,tr}
\tag{5.26}
$$

where the subscript "up" indicates the updated quantities. Based on this elastic assumption,

the plastic flow is frozen:

$$\Delta\lambda_i = 0;$$
$$\Delta\varepsilon_{M,up}^p = \mathbf{0}; \quad \Delta\varepsilon_{F,up}^p = \mathbf{0}; \quad \chi_{up} = \chi_{in}$$

(5.27)

where $\Delta\lambda_i = \Delta\lambda_{M,up}^{TC}$, $\Delta\lambda_{M,up}^{UN}$, $\Delta\lambda_{M,up}^{BI}$, $\Delta\lambda_{F,up}^{TC}$ and $\Delta\lambda_{F,up}^{DP}$; and $\mathbf{0}$ is a 3×3 matrix with only zero elements.

Step 2. Check Yield Conditions

In order to find plastically admissible stress fields, the five loading functions are considered according to the cracking condition of the composite matrix. For the 3-D model, a violated loading surface pointer c_v is introduced[6]:

$$
\begin{aligned}
c_v \quad = \quad & 2Y\left[f_M^{TC}\left(\sigma_{M,up}, \chi_{up}\right)\right] + 3Y\left[f_M^{UN}\left(\sigma_{M,up}, \chi_{up}\right)\right] \\
& + 4Y\left[f_M^{BI}\left(\sigma_{M,up}, \chi_{up}\right)\right] + 10Y\left[f_F^{TC}\left(\sigma_{F,up}\right)\right] + 20Y\left[f_F^{DP}\left(\sigma_{M,up}\right)\right]
\end{aligned}
$$

(5.28)

where the loading function for the composite matrix is based on the updated cracking state $F_M = F_M\left(\chi_{up}\right)$:

$$
\begin{aligned}
F_M\left(\chi_{up} = 0\right) &= F_M^0 \\
F_M\left(\chi_{up} = 1\right) &= F_M^{cr}
\end{aligned}
$$

(5.29)

These loading functions are defined by (4.44).

Since the 3-D early-age UHPC model has five loading functions, there are 24 possible plasticity cases representing different permutations of the loading functions. Table 5.1 summarizes all the possible cases in the model. Twenty-three of the cases require a plastic projection.

If there are no violated loading functions, i.e. $c_v = 0$, the updated stresses are plastically admissible. With the corresponding plastic multiplier ($\Delta\lambda_i \geq 0$), the final stresses are deter-

---

[6]Here, the terminology "violated" is used for the following case:

$$f_i > 0$$

where f_i is a loading function. This is because plastically admissible stresses always satisfy:

$$f_i \leq 0$$

No. of Violated Loading Functions	Violated Loading Functions		Value of Violated Surface Pointer $[c_v]$
	Matrix	Fiber	
0	-	-	0
1	f_M^{TC}	-	2
	f_M^{UN}	-	3
	f_M^{BI}	-	4
	-	f_F^{TC}	10
	-	f_F^{DP}	20
2	f_M^{TC}, f_M^{UN}	-	5
	f_M^{UN}, f_M^{BI}	-	7
	-	f_F^{TC}, f_F^{DP}	30
	f_M^{TC}	f_F^{TC}	12
	f_M^{TC}	f_F^{DP}	22
	f_M^{UN}	f_F^{TC}	13
	f_M^{UN}	f_F^{DP}	23
	f_M^{BI}	f_F^{TC}	14
	f_M^{BI}	f_F^{DP}	24
3	f_M^{TC}	f_F^{TC}, f_F^{DP}	32
	f_M^{UN}	f_F^{TC}, f_F^{DP}	33
	f_M^{BI}	f_F^{TC}, f_F^{DP}	34
	f_M^{TC}, f_M^{UN}	f_F^{TC}	15
	f_M^{TC}, f_M^{UN}	f_F^{DP}	25
	f_M^{UN}, f_M^{BI}	f_F^{TC}	17
	f_M^{UN}, f_M^{BI}	f_F^{DP}	27
4	f_M^{UN}, f_M^{BI}	f_F^{DP}, f_F^{DP}	35
	f_M^{UN}, f_M^{BI}	f_F^{DP}, f_F^{DP}	37

Table 5.1: Twenty-four possible plasticity cases representing different permutations of the loading functions [7].

mined in Step 4. Otherwise, a newly corrected incremental plastic strain is introduced in Step 3.

Step 3. Solve for the Plastic Strains

For the 23 possible plastic projection cases, the corresponding incremental plastic multipliers must be solved. The detailed procedures of the plastic projection scheme are extensively presented in Reference [7], and this report only summarizes the results of the triaxial loading case in Appendix A. With the solved set of the incremental plastic multipliers ($\Delta\lambda_M^{TC}$, $\Delta\lambda_M^{UN}$, $\Delta\lambda_M^{BI}$, $\Delta\lambda_F^{TC}$ and $\Delta\lambda_F^{DP}$), the incremental plastic strains ($\Delta\varepsilon_M^p$ and $\Delta\varepsilon_F^p$) can be calculated from the discretized forms of (2.30) and (2.31):

$$
\begin{aligned}
\Delta\varepsilon_{M,up}^p &= \Delta\lambda_{M,up}^{TC}\mathbf{1} + \Delta\lambda_{M,up}^{UN}\left[\alpha_M^{UN}\mathbf{1} + \mathbf{N}_{\mathbf{s},M}\right] + \Delta\lambda_{M,up}^{BI}\left[\alpha_M^{BI}\mathbf{1} + \mathbf{N}_{\mathbf{s},M,up}\right] \\
\Delta\varepsilon_{F,up}^p &= \Delta\lambda_{F,up}^{TC}\mathbf{1} + \Delta\lambda_{F,up}^{DP}\left[\alpha_F^{UN}\mathbf{1} + \mathbf{N}_{\mathbf{s},F,up}\right]
\end{aligned}
\tag{5.30}
$$

where $\mathbf{N}_{\mathbf{s},M,up} = \frac{\mathbf{s}_{M,up}}{|\mathbf{s}_{M,up}|}$ and $\mathbf{N}_{\mathbf{s},F,up} = \frac{\mathbf{s}_{F,up}}{|\mathbf{s}_{F,up}|}$ are the normalized deviatoric stress tensor of the composite matrix and the composite fiber, respectively.

As summarized in Table 5.1, the violated loading surface pointer c_v plays an important role in determining the plastic multipliers, $\Delta\lambda_i$. However, it should be noted that c_v denotes the yield surfaces that *might be* active. In other words, c_v does not dictate, only *suggests*, the projection scheme. Given any value of c_v, the correct plastic multiplier is the *smallest* among all possible plastic multipliers. In the finite element program, this concept is developed by first checking, given any value of c_v, the simplest cases which suggest multiple violated yield surfaces. It means that the correct plastic intensity must be found by searching first the cases of one violated loading function, then the cases of two violated loading functions, then the cases of three violated loading functions, and finally the cases of four violated loading functions.

After obtaining the incremental plastic strains from (5.30), the cracking state in the composite matrix is suggested by the plastic projection:

$$
\chi_{out} = 1 \quad \text{if} \quad \left|\Delta\varepsilon_{M,up}^p\right| \neq 0
\tag{5.31}
$$

and the composite stresses are updated from:

$$\boldsymbol{\sigma}_{M,up} = \boldsymbol{\sigma}_{M,tr} + \left[-3\left(K_M + K_I\right)\Delta\epsilon^p_{M,up} + 3K_I\Delta\epsilon^p_{F,up}\right]\mathbf{1} \tag{5.32}$$
$$-2\left(G_M + G_I\right)\Delta\mathbf{e}^p_{M,up} + 2G_I\Delta\mathbf{e}^p_{M,up}$$

$$\boldsymbol{\sigma}_{F,up} = \boldsymbol{\sigma}_{F,tr} + \left[3K_I\Delta\epsilon^p_{M,up} - 3\left(K_{F}+K_I\right)\Delta\epsilon^p_{F,up}\right]\mathbf{1} \tag{5.33}$$
$$+2G_I\Delta\mathbf{e}^p_{M,up} - 2\left(G_F + G_I\right)\Delta\mathbf{e}^p_{M,up}$$

Now, Step 2 must be repeated in order to check that the newly updated stress state does not violate the loading functions. If this is not the case, we proceed to Step 4.

Step 4. Update the Stresses

If there are no violated loading functions ($c_v = 0$) and the incremental plastic multipliers are correct ($\Delta\lambda_i \geq 0$), then the Kuhn-Tucker conditions (4.49) and (4.50) are satisfied. Then, the plastically admissible stresses and the corresponding strains are updated as follows:

$$\boldsymbol{\sigma}_{M,out} = \boldsymbol{\sigma}_{M,up}; \qquad \boldsymbol{\sigma}_{F,out} = \boldsymbol{\sigma}_{F,up};$$
$$\boldsymbol{\varepsilon}^p_{M,out} = \boldsymbol{\varepsilon}^p_{M,in} + \Delta\boldsymbol{\varepsilon}^p_{M,up}; \quad \boldsymbol{\varepsilon}^p_{M,out} = \boldsymbol{\varepsilon}^p_{M,in} + \Delta\boldsymbol{\varepsilon}^p_{M,up} \tag{5.34}$$

where $\Delta\boldsymbol{\varepsilon}^p_{M,up}$ and $\Delta\boldsymbol{\varepsilon}^p_{F,up}$ are zero if there are no plastic projections in Step 3. Furthermore, the macroscopic stress and strain are updated as well:

$$\boldsymbol{\Sigma}_{out} = \boldsymbol{\sigma}_{M,out} + \boldsymbol{\sigma}_{F,out}$$
$$\mathbf{E}_{out} = \mathbf{E}_{in} + \Delta\mathbf{E} \tag{5.35}$$

and the cracking parameter is determined:

$$\chi_{out} = \chi_{up} \tag{5.36}$$
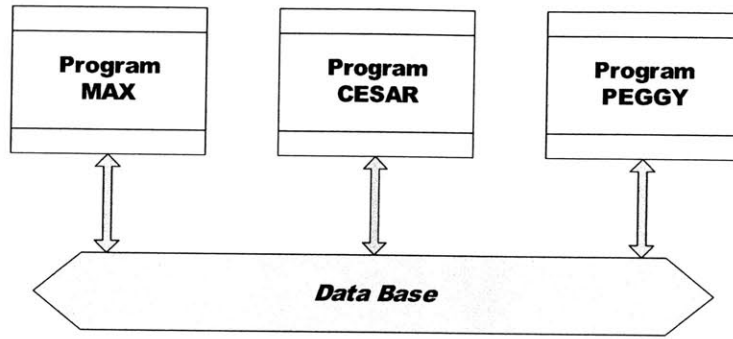
Figure 5-1: Overview of the CESAR-LCPC program structure.

5.2 The EAHC Finite Element Module

For the analysis of early-age UHPC structure, we implemented our model and algorithms in a finite element module, EAHC, embedded in a commercial finite element program, CESAR-LCPC. This section briefly presents the way by which our developments are implemented in CESAR-LCPC, in form of a simplified flow chart of an executable subroutine.

5.2.1 Overview of CESAR-LCPC

CESAR-LCPC is a FORTRAN based finite element program developed by the Laboratoire Central des Ponts et Chaussées [LCPC], Paris, France. CESAR-LCPC consists of three main programs: MAX which is the finite element pre-processor; CESAR which executes the finite element calculation as a main solver; and PEGGY which is the finite element post-processor. These three programs share a common date base which includes the geometry, material values, boundary conditions, load history, etc. Figure 5-1 shows an overview of the CESAR-LCPC program structure.

The main solver, CESAR, is composed of numerous calculation modules to solve various problems with different material behaviors such as linear elastic problem, diffusion problem, thermo-chemo-mechanical problem, etc. A simple flow chart for CESAR is illustrated in Figure 5-2.

97
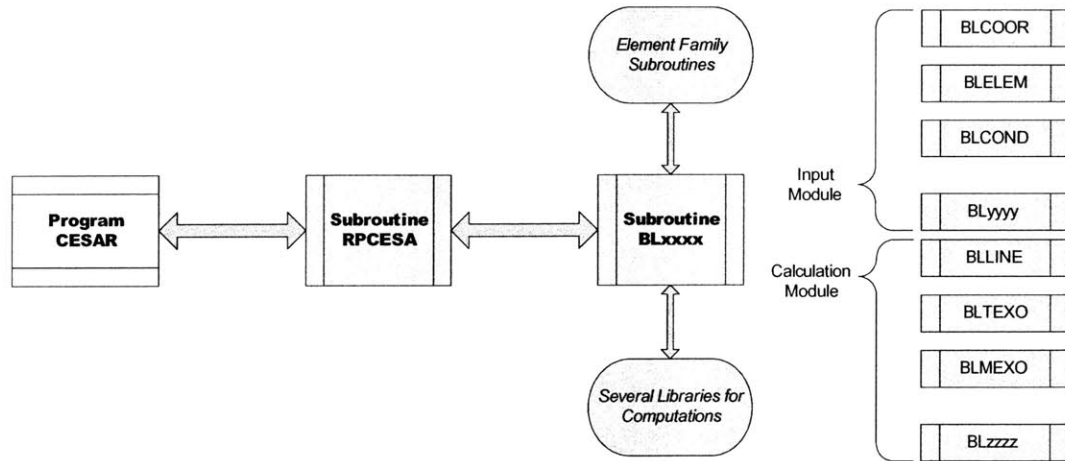
Figure 5-2: Overview of the subroutine structure of the main solver, program CESAR.

5.2.2 The EAHC Module

The finite element module, EAHC, is coded for the CESAR program in order to deal with the two-phase thermo-chemo-mechanical coupling behavior of UHPC at early ages. As discussed in Chapter 4, the implemented material model captures elastic, brittle and plastic behavior of early-age UHPC, with evolving stiffness and strength properties. In the CESAR program, there already exist a module MEXO, by which chemo-plastic problems can be solved in order to analyze the behavior of ordinary concrete at early ages. Moreover, a module HP2C, which can solve two-phase mechanical behavior of the hardened UHPC problem, has been embedded in the MEXO module by Chuang [7]. The coupling of these two pre-existing modules is carried out using the basic structure of the MEXO module. For each time step, the HP2C module is executed with evolving stiffness and strength properties. While coupling the two modules, minor modifications in MEXO and HP2C were introduced and several subroutines were developed. This newly modified module, EAHC, is named after *Early-Age ultra-High* performance *Concrete*.

Since the basic structure of MEXO is used for the new module, we need to explain briefly the subroutine BLMEXO, a calculation module shown in Figure 5-2. The most important subroutine in BLMEXO is EXMEXO, which is an executable subroutine whose structure is briefly reviewed with corresponding variables in Figure 5-3. The notations used in the figure

98

are consistent with the explanation in Section 5.1. In order to indicate the iteration number in the variables, a superscript $(IPAS)$ is used for time steps where external loadings change, and a subscript $(ITER)$ is used for the iterations of the global Newton-Raphson method. Furthermore, corresponding subroutines to the executions are presented in Figure 5-4. It is worthwhile to note that the return mapping algorithm is included in a subroutine "CPEAHC" where plastically admissible [correct] stress fields are obtained. The input data format for the EAHC module is presented in Appendix B.

5.2.3 Verification of the EAHC Module

The implementation of the early-age UHPC module is verified with respect to stability and consistency at the material level. As an example, this section shows the uniaxial response of an early-age UHPC element produced by the finite element module. The material properties of Ductal^{TM}-Steel Fiber are used for the model parameters of the hardened UHPC material, as listed in Table 2.4. In order to see the evolution of the material properties, four cases of hydration degree are considered, i.e. $\xi = 0.25$, 0.5, 0.75 and 1.0. As presented in Section 4.1, Byfors' evolution law is adopted for the stiffness properties and Laube's evolution law is used for strength properties.

The analytical solution for the uniaxial stress-strain behavior was presented in Section 4.2.6. It is used here for verificational purposes. Axi-symmetric 8-node quadrilateral elements are used for the simulations, and two types of meshes are employed for checking the consistency of the solution algorithm. Figure 5-5 shows the two types of mesh designs (a single element and fifty elements), their dimensions ($0.1 \ m \times 0.05 \ m$) and the employed boundary conditions. In order to obtain a stress-strain curve from the simulation, displacement driven test simulations were carried out. The simulation results in Figures (5-6)-(5-9) are compared with the analytical results from Figure 4-4 for the different hydration degrees. Both finite element simulation results show an excellent agreement with the analytical solutions, and they show very good convergence between different mesh densities.

EXMEXO

Read initial conditions relating to mechanics — $\mathbf{U}^0, \mathbf{R}^0$ *at nodes*

$\mathbf{\Sigma}^0, \mathbf{\sigma}_M^0, \mathbf{\varepsilon}_M^{p,0}, \mathbf{\varepsilon}_F^{p,0}, \Delta\mathbf{\sigma}_M^0, \chi^0$ *at integration points*

Calculate the interpolation functions

Read initial conditions relating to chemical reaction at nodes — $T^0, \Delta T^0, \xi^0, \Delta\xi^0$ *at nodes*

Calculate external nodal forces — $\mathbf{F}_{ext}^0$ *at nodes*

Convert stresses and strains at integration points into values at nodes — $\mathbf{\Sigma}^0, \mathbf{\varepsilon}_M^{p,0}$ *at nodes*

Save results into a file — $\mathbf{U}^0, \xi^0, \mathbf{\Sigma}^0, \mathbf{\varepsilon}_M^{p,0}$ *at nodes*

Cycle over time steps IPAS=0,NPAS → Return

Read IPASth conditions relating to chemical reaction at nodes — $T^{IPAS}, \Delta T^{IPAS}, \xi^{IPAS}, \Delta\xi^{IPAS}$ *at nodes*

Convert temperatures and hydration degrees at nodes into values at integration points — T^{IPAS}, ξ^{IPAS} *at integration points*

Calculate stresses relating to chemical reactions at integration points — $\Delta\mathbf{\Sigma}^{CT,IPAS}, \Delta\mathbf{\sigma}_M^{CT,IPAS}$ *at integration points*

Calculate the external nodal forces — $\mathbf{F}_{ext}^{IPAS}$ *at nodes*

Calculate the 0th-trial macroscopic stresses at integration points — $\mathbf{\Sigma}_0^{IPAS} = \mathbf{\Sigma}^{IPAS-1} + \Delta\mathbf{\Sigma}^{CT,IPAS}$ *at integration points*

Calculate the 0th-trial internal nodal forces w/o loading functions — $\mathbf{F}_{int,0}^{IPAS} = \int_{vl\,o\,f_i} \mathbf{B}^T\mathbf{\Sigma}_0^{IPAS}d\Omega$ *at nodes*

Calculate a tangent stiffness matrix considering hydration degrees — $\mathbf{K}^{IPAS} = \mathbf{C}_M\left(\xi^{IPAS}\right) + \mathbf{C}_F$

Calculate the 0th-trial residual nodal forces — $\mathbf{R}_0^{IPAS} = \mathbf{R}^{IPAS-1} + \left[\mathbf{F}_{ext}^{IPAS} - \mathbf{F}_{int,0}^{IPAS}\right]$ *at nodes*

Cycle over iterations ITER=1,NITER

Calculate incremental residual displacements at nodes — $\Delta\mathbf{U}_{ITER}^{IPAS} = \left[\mathbf{K}^{IPAS}\right]^{-1}\mathbf{R}_{ITER-1}^{IPAS}$ *at nodes*

Calculate incremental mechanical macroscopic stresses at intergration points by assuming linear elastic behavior — $\Delta\mathbf{\Sigma}_{ITER}^{ME,IPAS} = \mathbf{K}^{IPAS}\mathbf{B}\Delta\mathbf{U}_{ITER}^{IPAS}$ *at integration points*

Calculate ITERth-trial macroscopic stresses at integration points — $\mathbf{\Sigma}_{ITER}^{IPAS} = \mathbf{\Sigma}_{ITER-1}^{IPAS} + \Delta\mathbf{\Sigma}_{ITER}^{ME,IPAS}$ *at integration points*

Calculate displacements at nodes — $\mathbf{U}_{ITER}^{IPAS} = \mathbf{U}^{IPAS} + \Delta\mathbf{U}_{ITER}^{IPAS}$ *at nodes*

Calculate stresses corrected by loading functions — $\mathbf{\Sigma}_{ITER}^{IPAS}, \mathbf{\varepsilon}_{M,ITER}^{p,IPAS}, \mathbf{\varepsilon}_{F,ITER}^{p,IPAS}, \Delta\mathbf{\sigma}_M^{CT,IPAS}, \chi_{ITER}^{IPAS}$ *at integration points*

Calculate INTERth-trial internal nodal forces w/ loading functions — $\mathbf{F}_{ITER}^{int,IPAS} = \int_{vl\,f_i} \mathbf{B}^T\mathbf{\Sigma}_{ITER}^{IPAS}d\Omega$ *at nodes*

Calculate INTERth-trial residual forces — $\mathbf{R}_{ITER}^{IPAS} = \mathbf{F}_{ext}^{IPAS} - \mathbf{F}_{int,ITER}^{IPAS}$

Check convergence — NO / YES

Save results into a file

Figure 5-3: Flow chart of the subroutine EXMEXO and corresponding variables to be dealt with.

Figure 5-4: Flow chart of the subroutine EXMEXO and corresponding subroutines, where *italic letters* indicate newly developed subroutines for the EAHC module.

Figure 5-5: Mesh design and boundary conditions of the uniaxial tension test simulation using axisymmetric elements: (a) Single element, (b) Fifty elements.

Hydration Degree = 0.25

(a)

Hydration Degree = 0.25

(b)
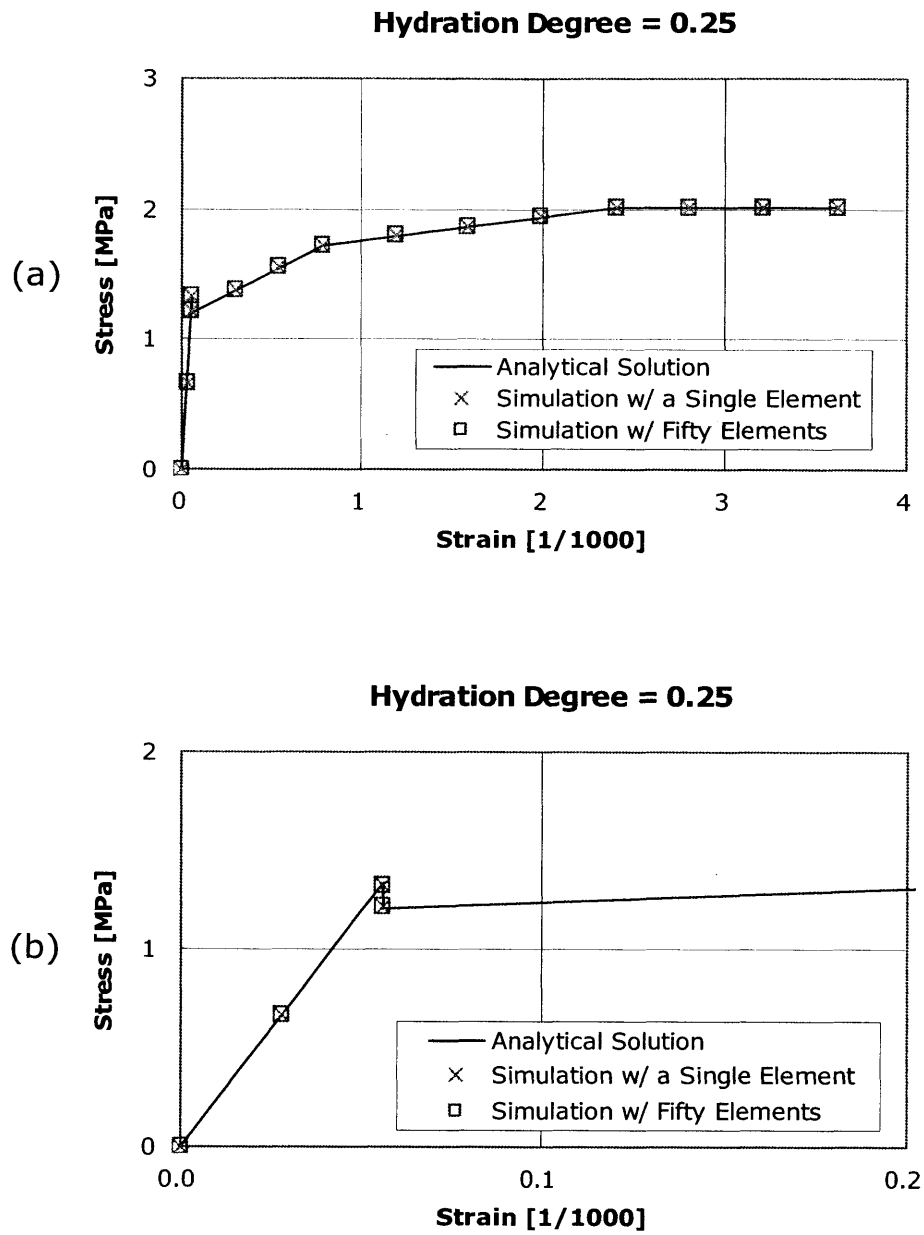
Figure 5-6: $\xi = 0.25$: uniaxial response of finite element simulations compared with the analytical simulations: (a) Entire stress-strain curve, (b) Focus on first cracking behavior.

103

Hydration Degree = 0.5

(a)

Hydration Degree = 0.5

(b)
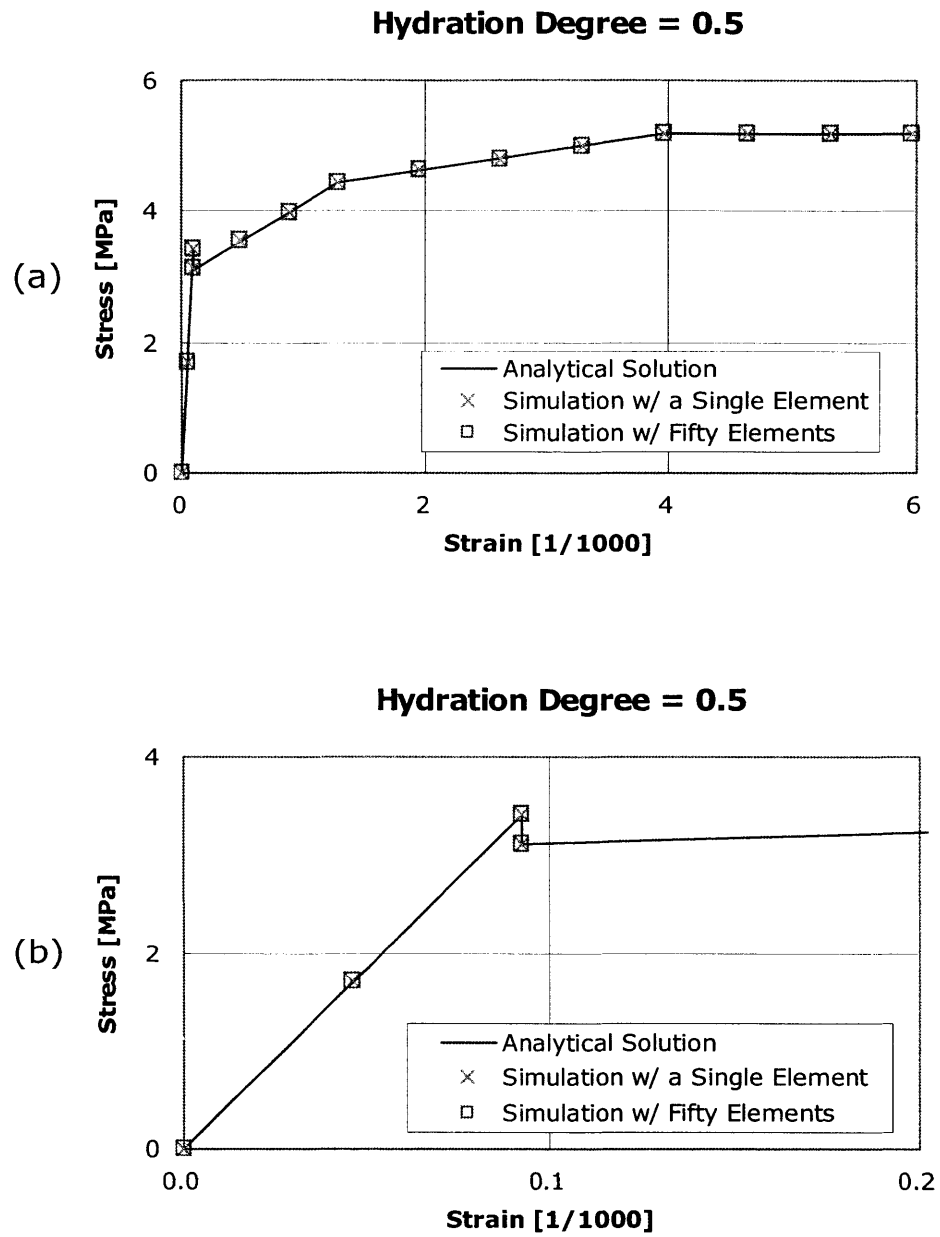
Figure 5-7: $\xi = 0.5$: uniaxial response of finite element simulations compared with the analytical simulations: (a) Entire stress-strain curve, (b) Focus on first cracking behavior.

104

Hydration Degree = 0.75

(a)

Hydration Degree = 0.75

(b)
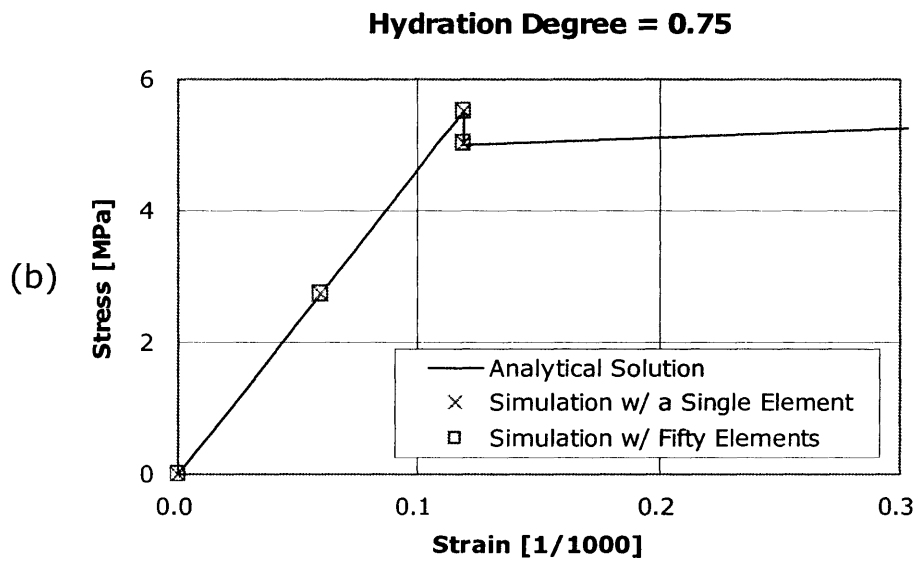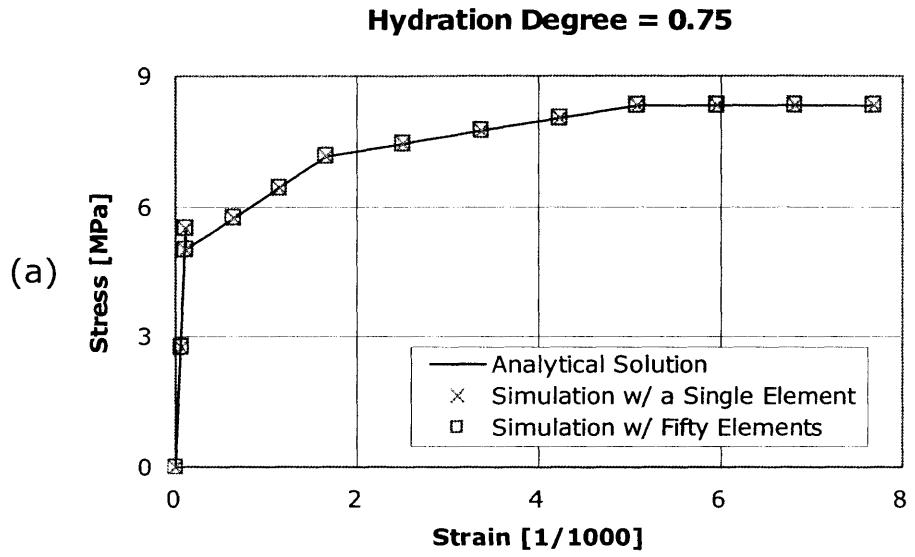
Figure 5-8: $\xi = 0.5$: uniaxial response of finite element simulations compared with the analytical simulations: (a) Entire stress-strain curve, (b) Focus on first cracking behavior.

Hydration Degree = 1.0

(a)

Hydration Degree = 1.0

(b)
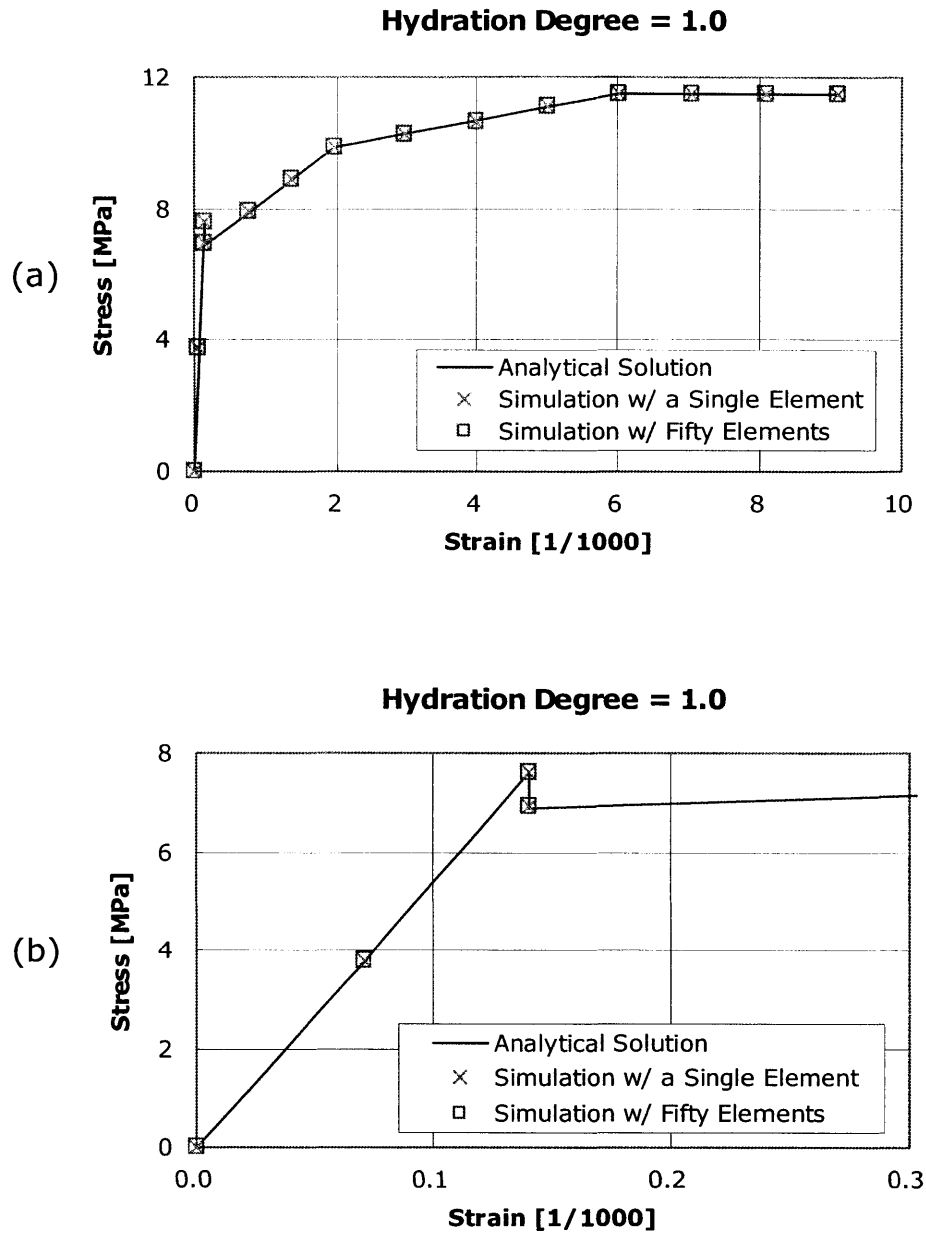
Figure 5-9: $\xi = 1.0$: uniaxial response of finite element simulations compared with the analytical simulations: (a) Entire stress-strain curve, (b) Focus on first cracking behavior.

5.3 Chapter Summary

This chapter describes the computational development of the early-age UHPC constitutive model into the EAHC finite element module. The module is embedded into a commercial finite element program, CESAR-LCPC. The EAHC module allows users to model early-age UHPC structures. Finite element formulation including finite element equations and the return mapping algorithm is presented in detail with flowcharts of executable subroutines and corresponding variables. Lastly, the proposed model is verified through simulations of uniaxial tension tests, showing an excellent agreement with the analytical solutions and very good convergence between different mesh densities.

Part III

ENGINEERING APPLICATION

Chapter 6

EARLY-AGE 3-D UHPC MODEL VALIDATION

During the recent manufacturing of a UHPC-girder, several cracks were observed in the deck and web of the girder. Several hypothesis for the origin of this cracking were discussed, raising questions whether the observed cracking was a consequence of the casting method, the prestress application or formwork removal procedure. In this Chapter, we try to address these questions by using the novel thermo-chemo-mechanical UHPC model. At the same time, the case study of the UHPC bridge girder will serve for validation of our model to ultimately answer the question, it is possible to predict and mitigate - by means of our advanced simulation tools - the risk of early-age UHPC cracking. What we present here as well, is the whole procedure of using our model, which includes the determination of the input parameters for both thermo-chemical and thermo-chemo-mechanical problem, boundary conditions, application of prestressing, and interpretation of simulation results.

6.1 Overview of Application

The bridge we study here is the prototype UHPC bridge which was developed at MIT for the Federal High-Way Administration [18]. The bridge was optimized by means of model-based simulation for relevant traffic loads and dead weight. This type of UHPC bridge has the potential to be used throughout the U.S. for the next generation of US-Highway Bridge

109
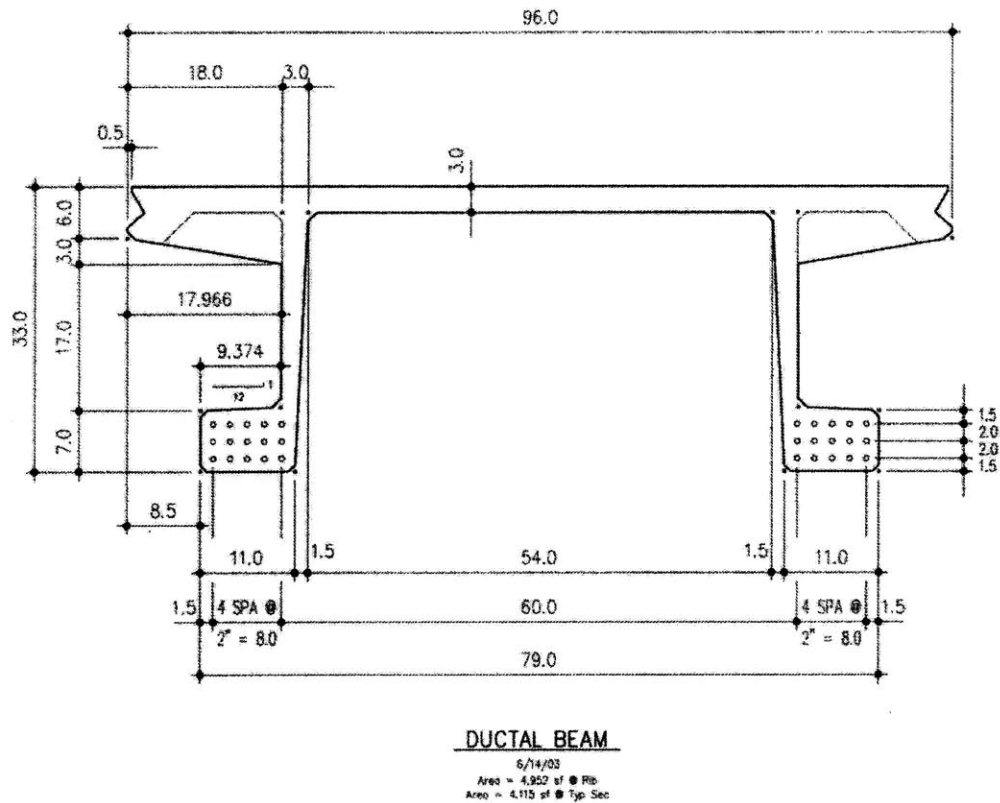
Figure 6-1: MIT optimized Ductal^{TM} bridge girder section (unit: *inch*) [20].

Girders. The section dimensions of the prestressed bridge girder are shown in Figure 6-1. The bridge is 21 *m* (70 *ft*) long, and 22 strands are employed for prestress through its bottom flange producing 2.4 *MN* (537 *kips*) of effective prestress. Figure 6-2 shows the configuration of the formwork, which is composed of three parts: an inner formwork, an outer formwork, and the bottom. This complex type of formwork was introduced in order to reduce autogenous shrinkage during the casting procedure, because the considered UHPC material is known to show considerable autogenous shrinkage. The bridge was cast by Prestress Service Inc. [PSi] with the collaboration of Federal Highway Administration [FHWA] and Lafarge North America. The construction was carried out over the period of October 11, 2003 to January 31, 2004.

When the bridge was moved out of its formwork, several cracks were observed in the deck and web of the girder. Especially, relatively large cracks normal to the longitudinal direction were observed (see Figure 6-3). The purpose of this engineering application is to validate the

110
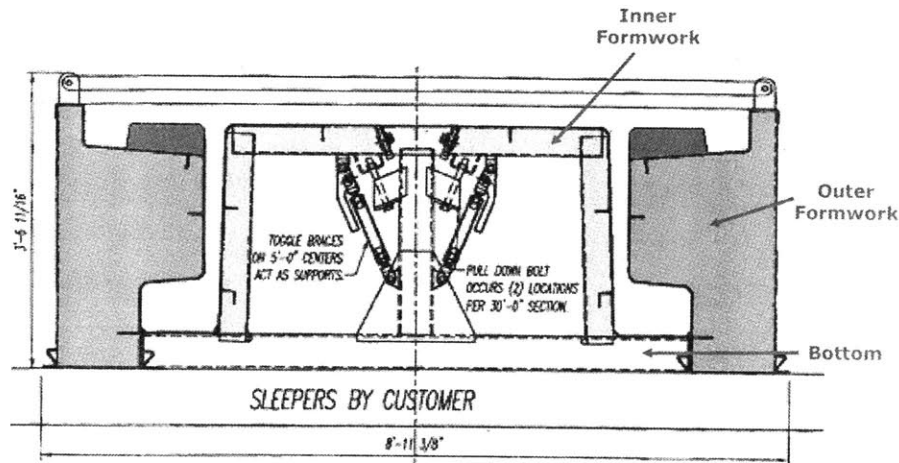
Figure 6-2: The configuration of formwork [9].

proposed early-age UHPC material model and to answer the following questions:

- Is it possible to predict the cracking with our new two-phase thermo-chemo-mechanical model?

- Is it possible to reduce the risk of early-age cracking?

Thanks to the decoupling hypothesis (see Section 4.2.2), the application of the early-age UHPC model can be carried out in a two-step manner. First, the thermo-chemical problem is solved, and the time histories of the temperature field and the hydration fields are obtained. These are input for the mechanical problem, for which we use the newly developed early-age UHPC model. Each of the two subproblem requires the determination of the input parameters, which includes material properties and boundary conditions. This case study also aims at illustrating how an engineer can use efficiently our new developments.

6.2 Thermo-Chemical Analysis

The thermo-chemical problem consists in solving simultaneously the hydration kinetic law (4.31) and the heat equation (4.32) for specific boundary condition; hence the following boundary value problem:
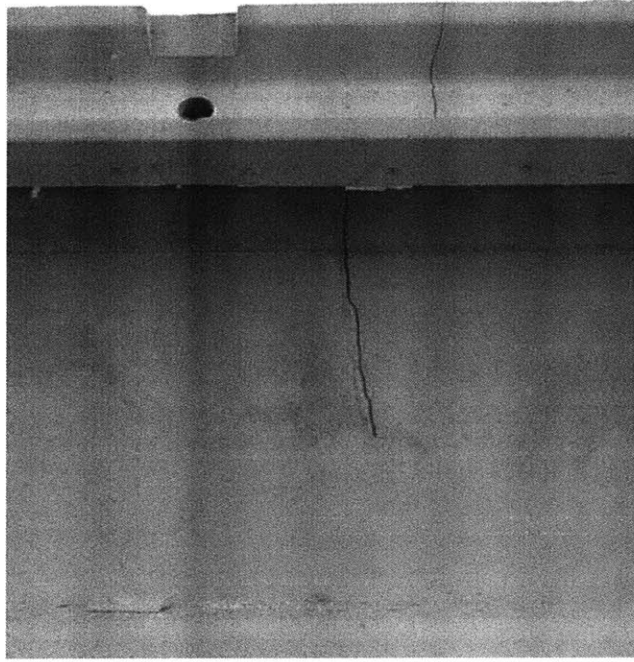
Figure 6-3: Cracking observed during casting, which runs from the deck to the neutral axis [9].

$$\frac{d\xi}{dt} = \tilde{A}(\xi)\,exp\left[-\frac{E_a}{RT}\right] \qquad \text{in } \Omega \tag{6.1}$$

$$C\frac{\partial T}{\partial t} = K\nabla^2 T + L\frac{d\xi}{dt} \qquad \text{in } \Omega \tag{6.2}$$

$$\mathbf{q}\cdot\mathbf{n} = \lambda\left(T - T_{ext}\right) \qquad \text{on } \partial\Omega$$

where $\mathbf{q}\cdot\mathbf{n}$ is the heat out-flux through the surfaces of the structure. These equations are implemented in CESAR-LCPC as module TEXO. Equations (6.1) and (6.2) require the determination of the following input parameters: volume heat capacity C, heat conductivity K, latent heat of hydration $L = C\left(T^{ad}_\infty - T^{ad}_0\right)$ (where $T^{ad}_\infty - T^{ad}_0$ is the adiabatic temperature rise; see Section 3.3.1), the hydration activation constant E_a/R; the normalized affinity function $\tilde{A}(\xi)$ (see Section 3.3); and finally the heat exchange coefficient λ of the formwork employed.

These model input parameters are obtained first, before discussing the simulation results: the time history of the temperature field $T(\mathbf{x}, t)$, and the hydration degree field $\xi(\mathbf{x}, t)$ in the

112
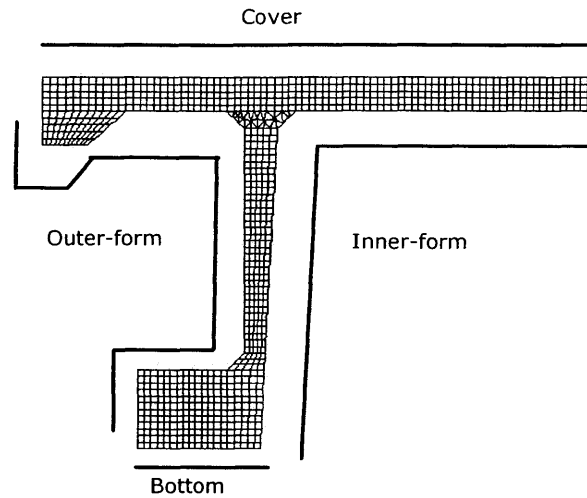
Figure 6-4: Mesh composed of *894* 2-D plain strain elements and *300* exchange elements denoted as black straight lines.

structure. The simulation results are then compared with temperature measurements carried out during casting on-site, providing a means to validate our input parameters.

6.2.1 Thermal Boundary Conditions

Figure 6-4 shows the mesh employed in the 2-D simulation of the bridge girder section. For symmetry reason, only half of the section is modeled, prescribing a zero heat-flux along the symmetry axis. The other surfaces are modeled by linear exchange elements defined by (6.2) (displayed in Figure 6-4 as black straight lines) which we use to simulate the loss of heat through the formworks. These exchange conditions allow us to simulate in detail the casting procedure.

At the site, the formworks were successively removed, and each formwork removal corresponds to a change of the thermal boundary conditions. At the beginning, both the inner formwork and the outer formwork were attached to the structure. The inner formwork was first removed 40 hours after casting, and the outer formwork was removed 50 hours after casting. This process is illustrated in Figure 6-5, displaying four phases which are considered in our simulations. Even though there is no difference in thermal boundary conditions before and

113
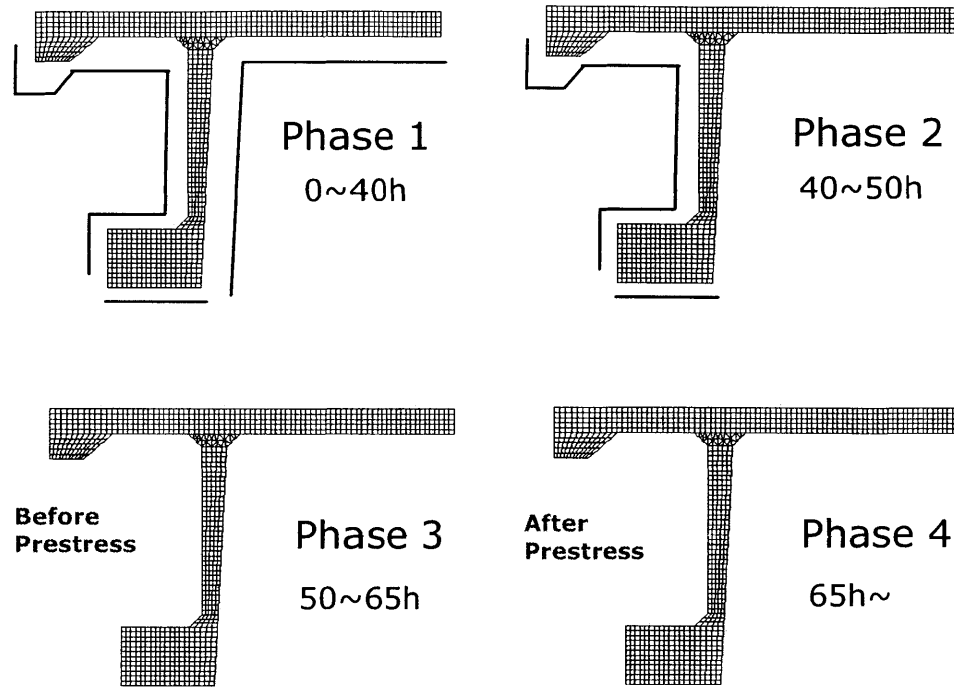
Figure 6-5: Progressive formwork removal inducing change in thermal boundary conditions.

after the application of the prestressing force, we separately considered these two phase because the prestressing corresponds to a change in mechanical boundary conditions. For each phase, different exchange coefficients were used for each part of the formwork, and they are summarized in Table 6.1. Using standard values of the literature [16], the exchange coefficient[1] was set to $\lambda = 14 \ kJ / \left(hr \times m^2 \times K \right)$ for the surface exposed to the air, and $\lambda = 10 \ kJ / \left(hr \times m^2 \times K \right)$ for surfaces with steel formwork. These exchange coefficient define the heat out-flux over the surface according to (6.2). The second input parameter required is the external temperature. This external temperature was measured during the casting process, and Figure 6-6 shows the simplified external temperature history we employed in simulations. Finally, after applying the prestressing force, the bridge girder was transported to an open field, and the formwork were removed for another bridge girder casting.

---

[1]It was reported that the bridge girder was placed in a tent during the casting process in order to prevent harsh external weather conditions [9]. Thus, this situation was considered as a non-ventillated condition for the exchange coefficient.

	Exchange Coefficient $\lambda \left[KJ/ \left(hr \times m^2 \times K \right) \right]$			
	Cover	Inner-form	Outer-form	Bottom
Phase 1	14	10	10	10
Phase 2	14	14	10	10
Phase 3	14	14	14	14
Phase 4	14	14	14	14

Table 6.1: Values of exchange coefficients for each phase.
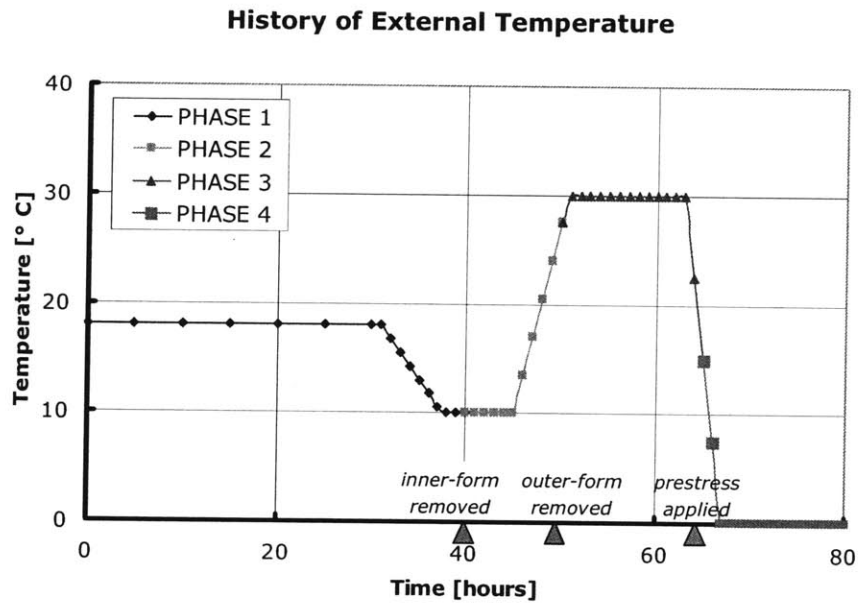
Figure 6-6: History of external temperature [9].

6.2.2 Thermal Properties and Adiabatic Temperature Curve

The second set of input parameters for the thermo-chemical problem includes the thermal properties and the normalized affinity of the UHPC material, here Ductal^{TM}.

Volume Heat Capacity

Since the volume heat capacity of steel $(C = 3,500 \ kJ/\left(m^3 \times K\right))$ is somewhat greater than the volume heat capacity of normal concrete $(C = 2,400 \ kJ/\left(m^3 \times K\right))$, it is reasonable to set the volume heat capacity of a steel fiber reinforced UHPC to a slightly greater value than that of ordinary concrete:

$$C = 2,700 \ kJ/\left(m^3 \times K\right) \tag{6.3}$$

Heat Conductivity

The heat conductivity of UHPC is estimated to be on the same order of that of ordinary concrete [16]:

$$K_{UHPC}^{unre} = 5 \ kJ/\left(hr \times m \times K\right) \tag{6.4}$$

This values is employed for the unreinforced deck and web of the girder. In return, the bottom flange is highly filled with prestressing cables that increase the heat conductivity, which is set to:

$$K_{UHPC}^{rein} = 8 \ kJ/\left(hr \times m \times K\right) \tag{6.5}$$

Adiabatic Temperature Curve

We have seen in Section 3.3 that the normalized affinity $\tilde{A}\left(\xi\right)$ can be equally accessed by either an adiabatic temperature curve or an isothermal strength evolution law. In the simulations, the adiabatic temperature curve $T^{ad}\left(t\right)$ is used as input to determine $\tilde{A}\left(\xi\right)$. However, the adiabatic temperature for Ductal^{TM} was not available, but fortunately the quasi-isothermal strength evolution was measured on-site, which we used to determine the normalized affinity from (see Section 3.3.2):

$$\tilde{A}\left(\xi\right) = exp\left[\frac{E_a}{RT^{iso}}\right]\frac{1}{f_\infty^{iso} - f_0}\frac{df^{iso}}{dt} \tag{6.6}$$

Here, $f^{iso}(t)$ is the compressive strength growth curve, which we determine by interpolating the compressive strength values measured on-site[2]. This fitting is displayed in Figure 6-7 (a), since the hydration degree can be determined from (see Section 3.3.2):

$$\xi(t) = \frac{f^{iso}(t) - f_0}{f_\infty^{iso} - f_0} \tag{6.7}$$

We can determine the normalized affinity curve, as displayed in Figure 6-7 (b). Finally, using the determined affinity curve in the heat equation (6.2) for adiabatic conditions, we obtain after integration the adiabatic temperature curve $T^{ad}(t) - T_0^{ad}$:

$$T^{ad}(t) - T_0^{ad} = \left(T_\infty^{ad} - T_0^{ad}\right) \int_0^t \tilde{A}(\xi) \, exp\left[-\frac{E_a}{RT^{ad}(s)}\right] ds \tag{6.8}$$

where:

$$\xi(t) = \frac{T^{ad}(t) - T_0}{T_\infty^{ad} - T_0} \tag{6.9}$$

The procedure requires some iteration, and the result is displayed in Figure 6-7 (c).

This iterative procedure requires as input the activation energy or more precisely a reference value for the dimensionless number $E_a/\left(RT^{iso}\right)$ in the strength rate - normalized affinity relation (6.6). Inspired from typical values for the activation energy for ordinary concrete E_a/R = $4,000 - 4,150$ K, we choose:

$$\frac{E_a}{RT^{iso}} = \frac{4000}{273} = \frac{4150}{283} = 14.7 \tag{6.10}$$

It should be noted that fixing the values of $E_a/\left(RT^{iso}\right)$ ensures that the normalized affinity curve obtained from the isothermal strength growth is the same irrespective of the temperature T^{iso}. This is constant with the fact that the normalized affinity curve is an intrinsic material property which is independent of thermal boundary conditions. On the other hand, the choice of the activation energy $(E_a/R = 4,000K$ or $E_a/R = 4,150K)$ has some effects on the rate of the adiabatic temperature rise. This is illustrated in Figure 6-8. While the normalized affinity curve $\tilde{A}(\xi)$ in the same (by construction, see Figure 6-8 (a)), a higher activation energy leads to

---

[2]It was reported that the compressive strength specimen were placed in the tent where the bridge girder was cast [9].

Evolution of Compressive Strength

(a)

Comparison of Affinities

(b)

Simulated Evolution of Adiabatic Temperature

(c)
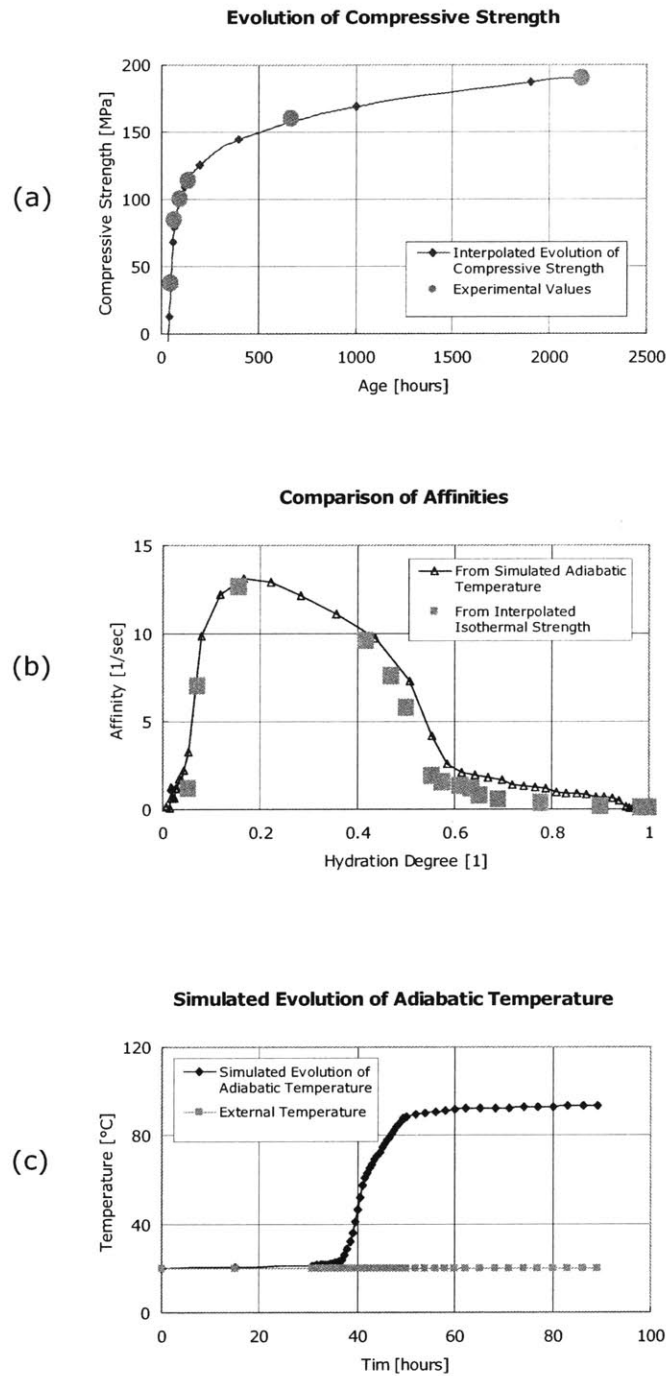
Figure 6-7: Procedure to obtain the simulated adiabatic temperature curve from the isothermal compressive strenght growth: (a) Evolution of the compressive strength, (b) Comparison of the affinities from simulated adiabatic temperature and interpolated quasi-isothermal compressive strength, (c) Determined evolution of the adiabatic temperature ($E_a/R = 4,000\ K$).

118

slower evolution of the adiabatic temperature rise (Figure 6-8 (b)), because a higher activation energy decreases the reaction rate (6.1). While the difference in between the two temperature curve is not enormous, it is not insignificant, thus high-lighting the necessity of an adiabatic temperature test for the UHPC material. Such an adiabatic temperature curve in combination with the isothermal strength growth determined on-site would provide more accurate values of the activation energy.

In the absence of this adiabatic temperature curve for Ductal^{TM}, we will consider both adiabatic temperature curves in the simulation. A first-order engineering validation of the here determined normalized affinity curve is obtained by comparing the simulated temperature history with temperature values measure on-site.

6.2.3 Simulation Results and Validation

Temperatures were measured at three points in the structure: the deck, the web and the bottom flange, as shown in Figure 6-9. Figure 6-10 shows the temperature history measured on site. The bottom flange showed a higher temperature than other measurement points because it has the characteristics of a massive concrete structure. The maximum temperature in the bottom flange is 52 $°C$. The maximum temperature for each location occurred in the time interval between 58 and 63 hours after casting. The temperature was measured on site until the prestressing force was applied.

The simulated temperature histories are displayed in Figure 6-11, obtained with an activation energy of $E_a/R = 4,000K$. As expected, the highest temperature rise occurs in the bottom flange with a maximum temperature of 51 $°C$, which compares very well with the measured value of 52 $°C$. This maximum temperature occurs in the time interval between 53 and 58 hours, which is close to the measured time of $58 - 63$ hours after casting. The slightly premature occurrence of the maximum temperature can be attributed to the choice of the activation energy of $E_a/R = 4,000K$. In fact, Figure 6-12 display a comparison of the measured temperatures and simulated results obtained respectively with $E_a/R = 4,000$ K (Figure 6-12 (a)) and $E_a/R = 4,150$ K (Figure 6-12 (b)). The simulations carried out with a higher activation energy predict more accurately the time occurrence of the maximum temperature. On the other hand, the maximum temperature in the bottom flange is slightly underestimated in

Comparison of Affinities

(a)

Simulated Evolution of Adiabatic Temperature

(b)
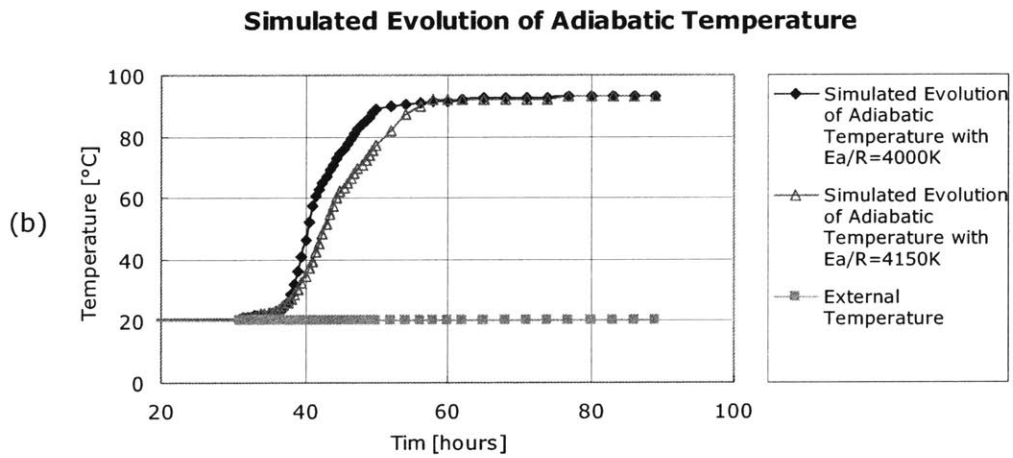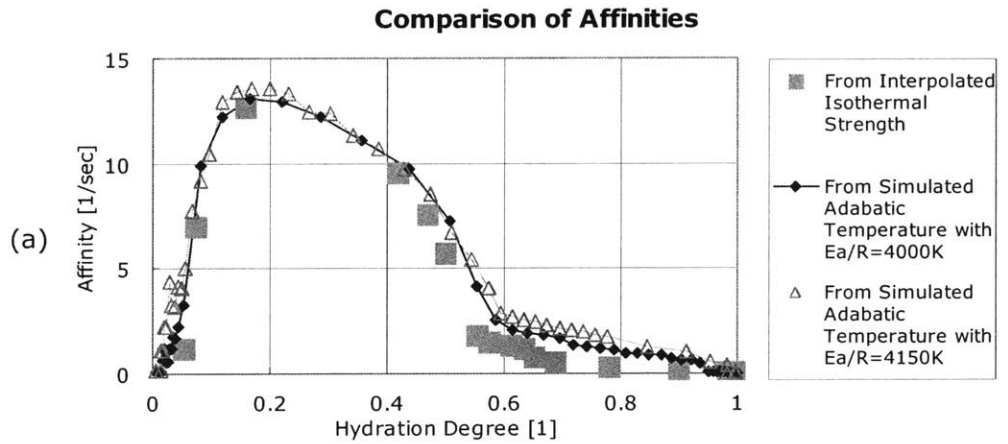
Figure 6-8: (a) Comparison of two affinities from simulated adiabatic temperature ($E_a/R = 4,000K$ and $4,150K$) and the extrapolated quasi-isothermal compressive strength, (b) Comparison of two simulated adiabatic temperature curves ($E_a/R = 4,000K$ and $4,150K$).
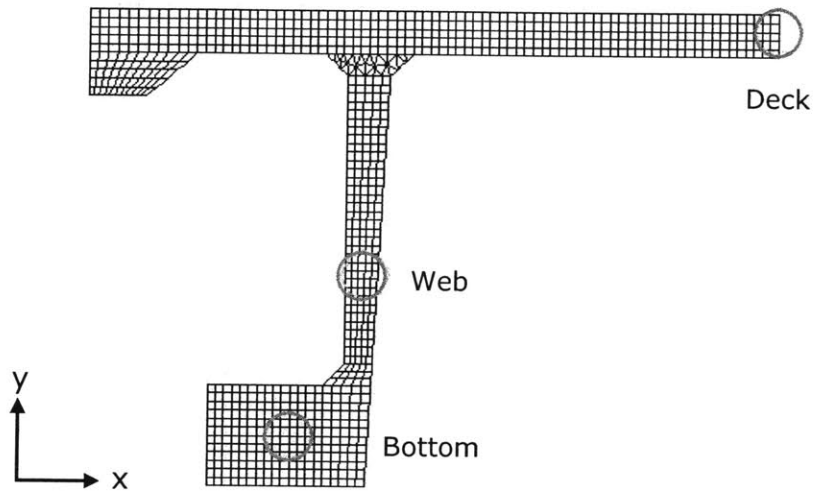
Figure 6-9: Location of measurements.
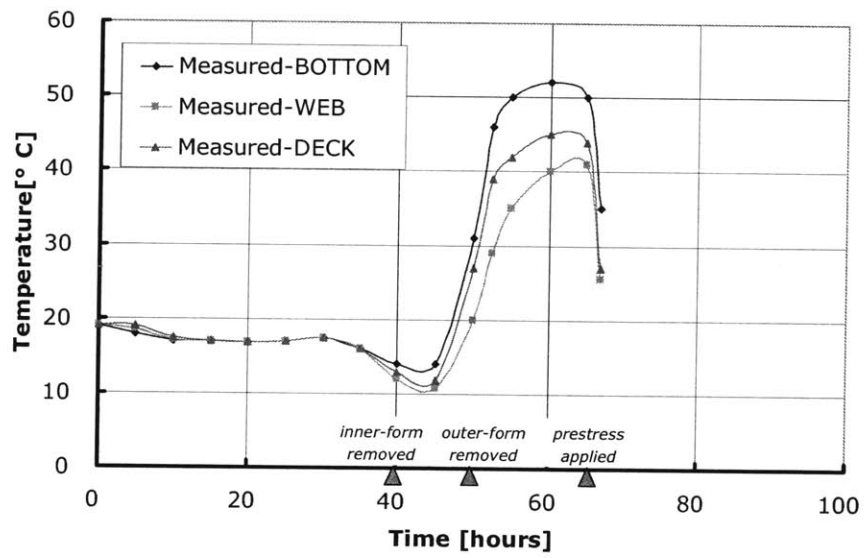
Figure 6-10: Temperature history measured on site [9].
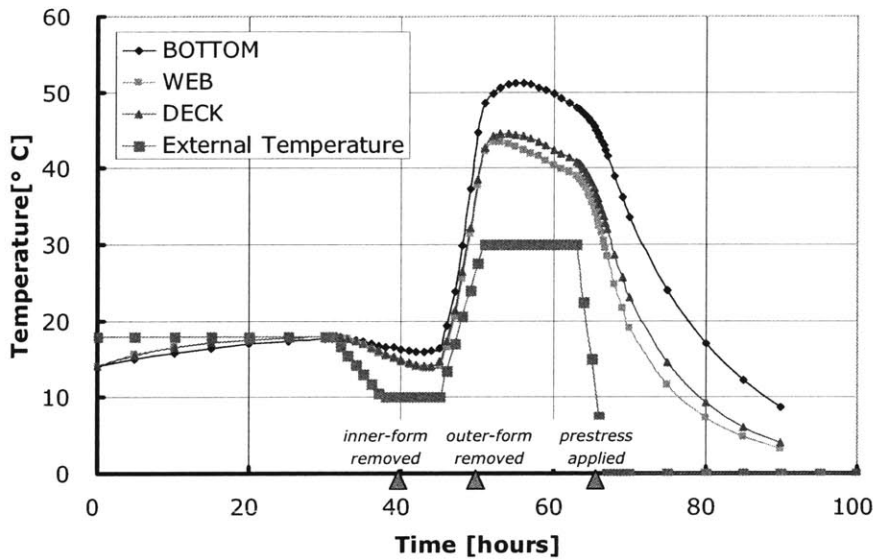
Figure 6-11: Temperature history from the simulation with $E_a/R = 4,000\ K$.

the simulation result obtained with $E_a/R = 4,150\ K$ ($\max[T - T_0] = 49\ °C$ vs. the measured $52\ °C$). Note that the temperature histories for both web and deck are little affected by the value of the activation energy, and are very similar, because their dimensions are similar.

For the mechanical simulations of stresses and deformations, we choose the $E_a/R = 4,000\ K$ simulation results. This choice is based on an overall comparison of the simulated temperature values vs. measured values, displayed in Figures 6-12 and 6-13. While Figure 6-13 shows that both simulation results give comparable correct predictions regarding temperature distribution, the $E_a/R = 4,000\ K$ simulation results (Figure 6-12) give a closer agreement with the maximum temperature measured on-site. On the other hand, the $E_a/R = 4,000\ K$ simulations overestimate the temperature in the web.

Finally, Figure 6-14 shows a typical example of a simulated temperature distribution for $E_a/R = 4,000K$ at the time of prestress application. This instant will turn out to be important. The maximum temperature difference between the bottom flange and web is around $10\ K$. As expected, the bottom flange has a higher temperature, compared to the deck and the web. Moreover, a local temperature gradient effect can be seen: the temperature at the surface is

122

(a)

(b)
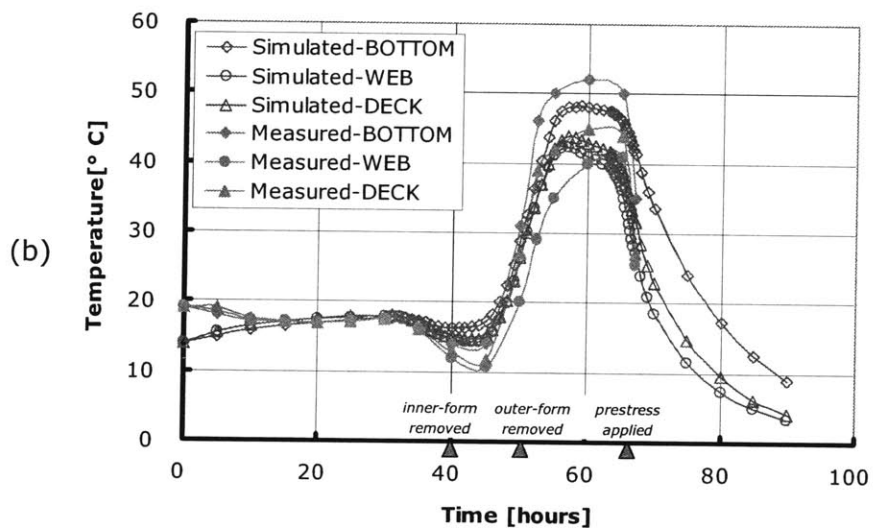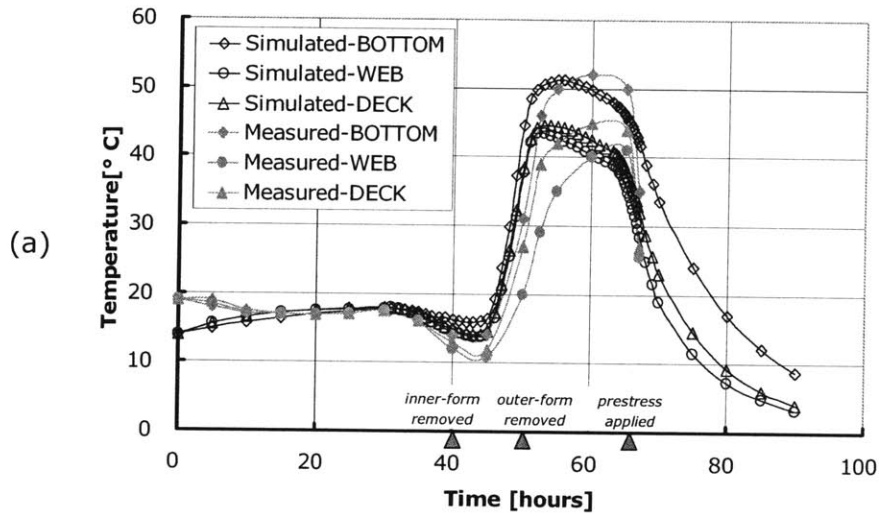
Figure 6-12: Comparison of on-site measured and simulated temperature histories: (a) $E_a/R = 4,000\ K$, (b) $E_a/R = 4,150\ K$.

MeasuredTemperature Compared with Simulated Temperature
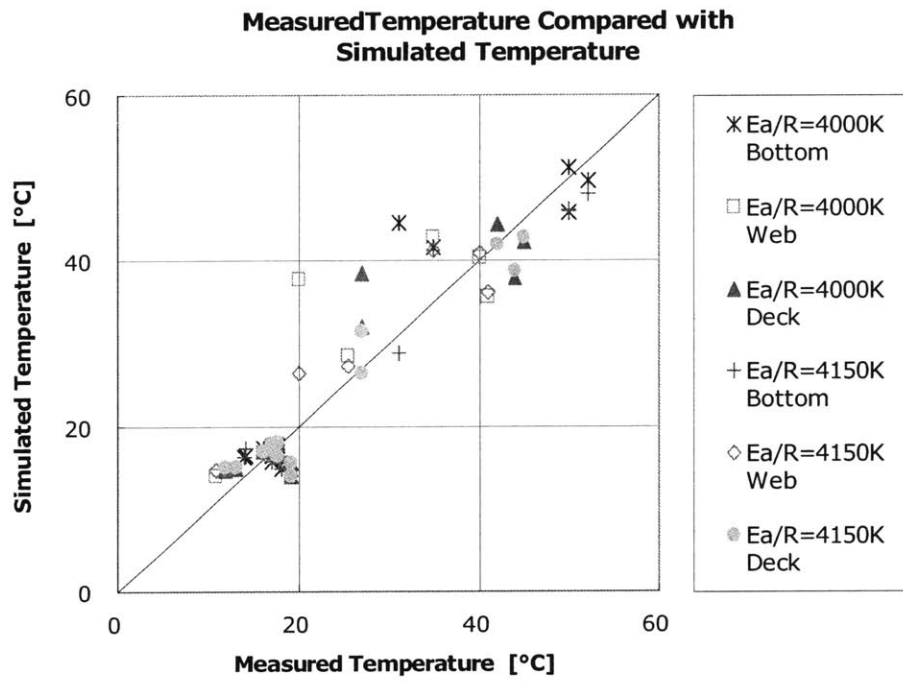
Figure 6-13: Measured temperatures compared with simulated temperature.

Max. $\Delta T \approx 10K$
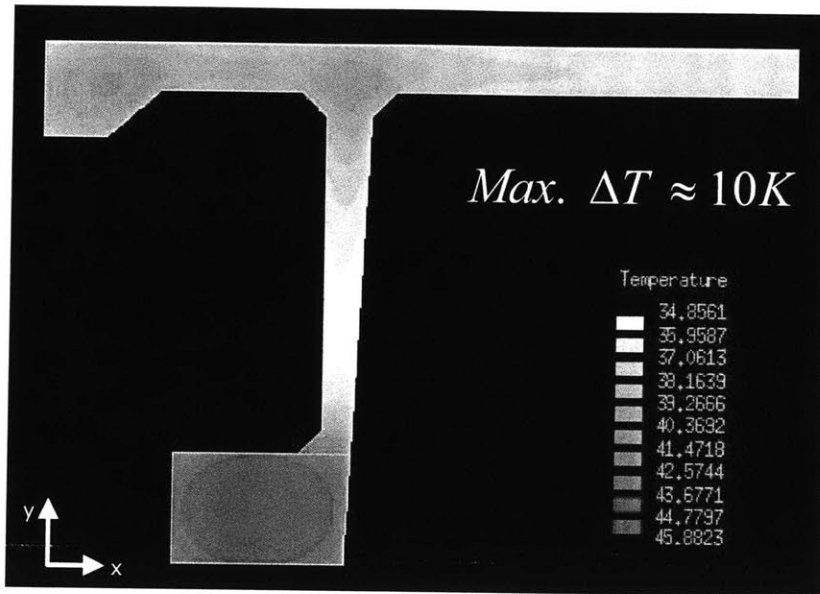
Figure 6-14: Temperature distribution at the moment of prestress application.

lower than the inside temperature.

6.3 Two-Phase Thermo-Chemo-Mechanical Analysis

The time history of temperature distribution $T(\mathbf{x},t)$ and hydration degree distribution $\xi(\mathbf{x},t)$, determined from the thermo-chemical analysis (see Section 6.2) serves as input for the mechanical analysis of stresses, deformation and permanent strains associated with cracking, that develop during casting and hardening of the UHPC girder. This mechanical analysis is achieved with the newly developed early-age UHPC module, detailed in Chapter 5 and implemented in CESAR-LCPC.

6.3.1 Plane-Section Simulation

The mechanical simulations of the girder sections are carried out in 2-D, using the plane-section assumption. It is assumed that the section remains plane during deformation, which is highly relevant for beam-type structures. This assumption allows one to reduce the complete 3-D simulation of the beam structure to 2-D simulations of the section, while considering the normal

forces and bending moments induced by the dead weight and the application of prestressing in the statically determined structure.

The plane-section assumption ensures that the total strain in the z-direction (out-of-plane direction) complies with the Bernoulli condition:

$$E_{zz}(x,y) = \epsilon_z^0 + y\theta_x - x\theta_y \tag{6.11}$$

where ϵ_z^0, θ_x and θ_y are the average strain in the z-direction and the curvatures around the x- and y-axes, respectively. These three section unknowns need to be determined. To this end, the global equilibrium in the section "A" is calculated, using the common definition of the normal force and the bending moment:

$$\mathbf{N} = \int_A \mathbf{\Sigma} \cdot \mathbf{e}_z \, dA \tag{6.12}$$

$$\mathbf{M} = \int_A (x\mathbf{e}_x + y\mathbf{e}_y) \times (\mathbf{\Sigma} \cdot \mathbf{e}_z) \, dA \tag{6.13}$$

where "$\times$" denotes the cross product. The stress tensor in any part of the section can be written as:

$$\mathbf{\Sigma} = \mathbf{\Sigma}^{PS} + \varkappa \, diag \begin{bmatrix} 1 & 1 & \frac{1-\nu}{\nu} \end{bmatrix} E_{zz} \tag{6.14}$$

where $\mathbf{\Sigma}^{PS}$ is the total stress tensor corresponding to plane strain conditions ($E_{zz} \equiv 0$), and

$$\varkappa(\xi) = \nu \frac{K_0(\xi)}{(1-2\nu)(1+\nu)} \tag{6.15}$$

with $K_0(\xi) = C_M(\xi) + C_F$ is the composite Young's modulus. Use of (6.14) in (6.12) and (6.13) leads to expressing the section equilibrium in the following form:

$$0 = \left\{ \begin{array}{c} N^{PS} - N^d \\ M_x^{PS} - M_x^d \\ M_y^{PS} - M_y^d \end{array} \right\} + \frac{1-\nu}{\nu} \left[\begin{array}{ccc} \int_A \varkappa(\xi)\,dA & \int_A \varkappa(\xi)\,y\,dA & -\int_A \varkappa(\xi)\,x\,dA \\ \int_A \varkappa(\xi)\,y\,dA & \int_A \varkappa(\xi)\,y^2\,dA & -\int_A \varkappa(\xi)\,xy\,dA \\ -\int_A \varkappa(\xi)\,x\,dA & -\int_A \varkappa(\xi)\,xy\,dA & \int_A \varkappa(\xi)\,x^2\,dA \end{array} \right] \left\{ \begin{array}{c} \epsilon_z^0 \\ \theta_x \\ \theta_y \end{array} \right\} \tag{6.16}$$

where (N^d, M_x^d and M_y^d) are prescribed normal force and moments on the beam (dead weigth and prestressing), while (N^{PS}, M_x^{PS} and M_y^{PS}) are obtained by application of (6.12) and (6.13)

to the plane-strain stress $\boldsymbol{\Sigma} \rightarrow \boldsymbol{\Sigma}^{PS}$. In the mechanical calculation, relation (6.16) is solved at every iteration, and the total stress in the section is corrected according to relation (6.14). Finally, relation (6.12) is used to evaluate the longitudinal strain $E_{zz}(t)$ at different points in the section, for which measurements from the site are available.

6.3.2 Mechanical Boundary Conditions

Like every mechanical problem, the stress and deformation analysis of the UHPC girder at early ages requires force and displacement boundary conditions as input.

Displacement Boundary Conditions

In the particular case of the early-age behavior of UHPC structures, the displacement boundary conditions are defined by the formwork. More precisely, each formwork removal on-site corresponds to a change in the displacement boundary conditions. For the four phases considered in the thermo-chemical analysis (see Section 6.2.1, Figure 6-5), the displacements are set to zero at those boundaries where a formwork is placed. The progressive formwork removal and the corresponding change in displacement boundary conditions we consider in the simulations are displayed in Figure 6-15. In this figure, straight lines represent a zero-displacement boundary[3] and the removal of the formwork from one phase to the other represents a release of this zero-displacement boundary, so that the surface becomes stress-free $(\boldsymbol{\Sigma} \cdot \mathbf{n} = \mathbf{0})$. The finite element simulations are performed on the same mesh as the thermo-chemical analysis. The zero-displacement in the symmetry axis of the section is due to symmetry considerations.

Force Boundary Condition

Beside the stress-free boundary condition at the free surfaces that relate to the formwork removal procedure (see Figure 6-5), there are two further prescribed forces to be considered: the dead weight and the prestress application. Since the girder remains on the formwork until it is lifted out, the dead weight is of minor importance. In return, application of the prestressing (in Phase 4) leads to introduce both a normal force and bending moments. These effects are considered

---

[3] The zero-displacement means that displacements normal to the boundary are zero.
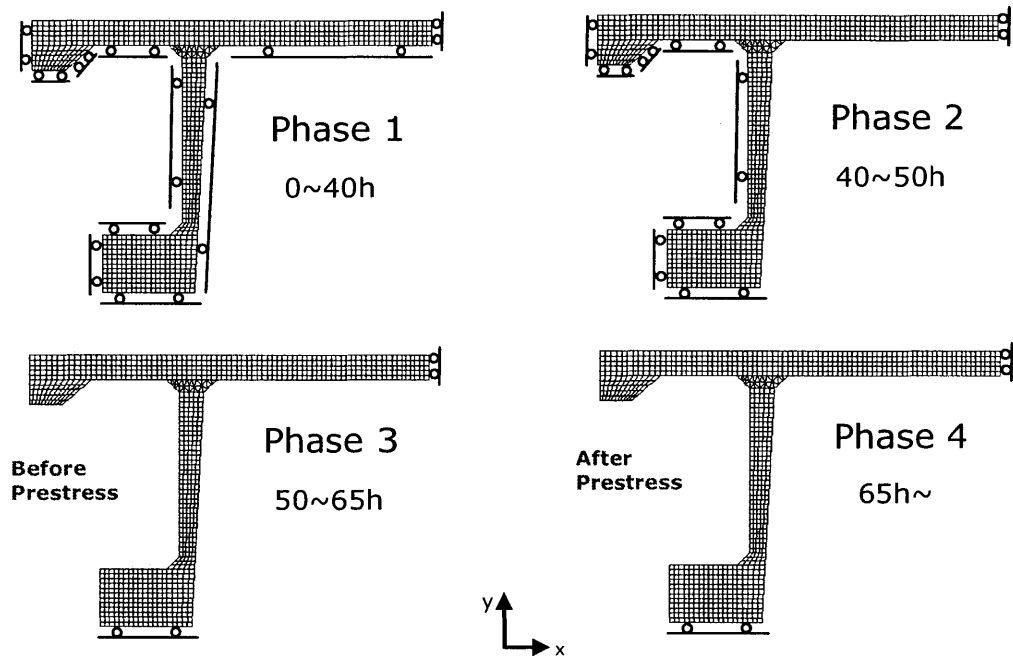
Figure 6-15: Progressive formwork removal inducing a change in displacement boundary conditions.

in the simulations through relation (6.16), by letting:

$$N^d = -P$$
$$M_x^d = Pe_y$$
$$M_y^d = Pe_x$$

(6.17)

where $P = 1.2\ MN$ is the effective prestressing force for a half girder and $(e_x,\ e_y) = (0.46\ m,$ $0.13\ m)$ is the distance between the center of gravity of the half section and the center of the prestressing force. Conditions (6.17) are prescribed in the simulations in Phase 4.

6.3.3 Mechanical Material Properties

The second set of input parameters for the mechanical analysis is the set of properties required by the two-phase early-age UHPC model. By construction, these are (see Section 4.2.4):

- The hardened UHPC properties: Elastic properties $(C_M,\ C_F,\ M$ and $\nu)$ and strength properties $(\sigma_{Mt},\ \sigma_{Mt}^{cr},\ \sigma_{Mc},\ \sigma_{Mb},\ \sigma_{Ft}$ and $\sigma_{Fc})$. These can be obtained from the test data provided by the manufacturer.

- The thermo-chemical properties of UHPC: Thermal dilatation coefficients $(\alpha_M$ and $\alpha_F)$, chemical dilatation coefficient $(\beta_M$ and $\beta_F)$ and the percolation threshold (ξ_0) (see Section 4.1.1).

For the hardened UHPC properties, the model parameters of Ductal^{TM}-Steel Fiber are employed (see Table 2.4). In addition, Table 6.2 lists the thermo-chemical deformation properties we consider in the simulations. The thermal dilatation coefficient for both composite phases are assumed to be the same. In return, only the composite matrix phase is assumed to undergo chemical shrinkage. The value of $\beta_M = -8 \times 10^{-4}$ is estimated from autogenous shrinkage values for low water/cement ratio concrete in the open literature[4] [3]. Finally, re-

---

[4]The value of $\beta_M = -8 \times 10^{-4}$ yields maximum autogenous shrinkage of the composite matrix of $\epsilon = -800\ \mu m/m$. This value includes hydration shrinkage related to the Le Chatelier contraction and the shrinkage induced by the hydric pressure that develop in the material at early-ages. Since we do not distinguish these two phenomena, the maximum shrinkage induced is an upper bound to the actual autogenous shrinkage. This is appropriate with respect to the focus of our simulation: to evaluate the risk of early-age UHPC cracking.

	Matrix	Steel Fiber
Thermal dilatation coefficient $[1/K]$	$\alpha_M = 1 \times 10^{-5}$	$\alpha_F = 1 \times 10^{-5}$
Chemical shrinkage coefficient $[1]$	$\beta_M = -8 \times 10^{-4}$	$\beta_F = 0$
Percolation threshold $[1]$	$\xi_0 = 0.1$	-

Table 6.2: Thermo-chemical deformation properties of UHPC considered in the simulations.

garding the percolation threshold, we employ $\xi = 0.1$, as generally admitted in the early-age concrete literature [25][26].

6.3.4 Validation

On-site, longitudinal strains (in the z-direction) were measured by strain gauges at the deck and the bottom flange until the application of the prestressing. We use these measured values for validation of the model and its implementation in the finite element program. Figure 6-16 compares the recorded strain measurements with the longitudinal macroscopic strains E_{zz} determined from the application of the plane-section model (6.11) in our simulations. The simulated strain history at different points in the section shows a very good agreement with the measured strains, except for the web. This is not surprising, given the discrepancy of temperature we found in the thermo-chemical simulation. Figure 6-17 displays the simulated results vs. the measured results of the deck and the bottom flange. The good agreement here provides strong evidence that our new model gives a relatively accurate prediction of the deformation behavior of the UHPC girder at early ages. Based on this validation, we can now turn to the question, what caused the early-age cracking observed in the girder.

6.4 What Caused the Early-Age UHPC Cracking?

The crack were observed normal to the longitudinal direction (beam axis). Such cracks result from a longitudinal stress excess. Thus, to answer the raised question, our main focus will be on stresses and plastic strains in the longitudinal axis.

Time History of Strains (Ezz)
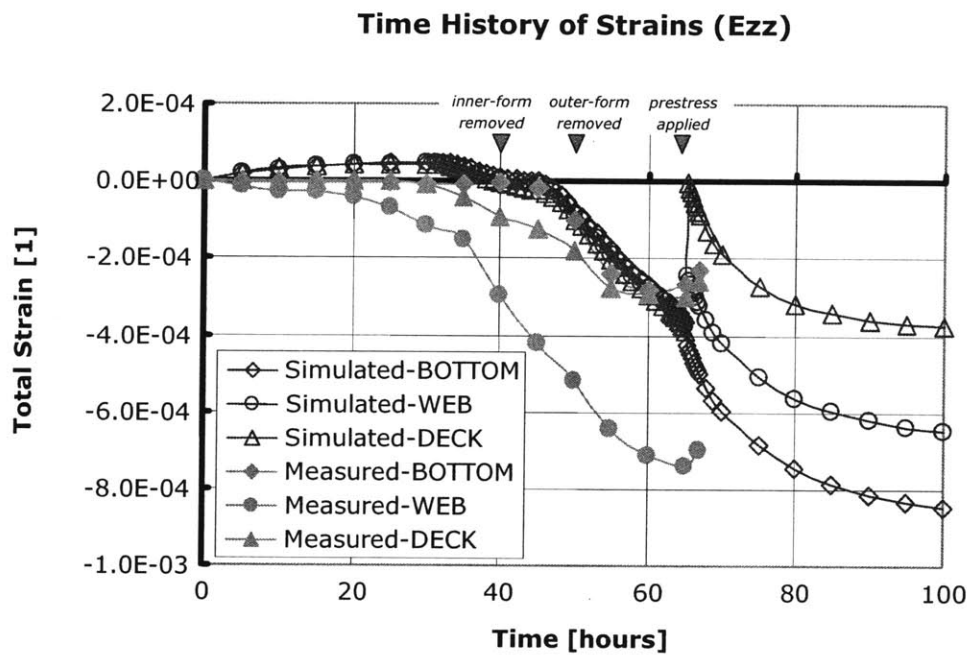
Figure 6-16: Simulated longitudinal strain histories compared with the strain measurements on site.

131

Measured Strains Compared with Simulated Strains
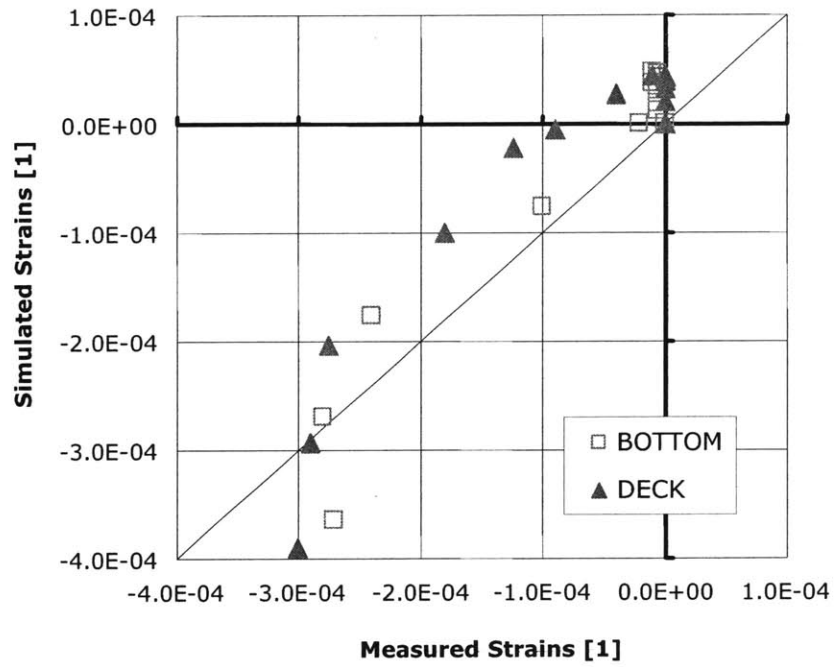
Figure 6-17: Measured strains compared with simulated strains.

6.4.1 Stress and Plastic Strain Distributions

The longitudinal macroscopic stress (Σ_{zz}) from the simulation is first investigated. In Phase 1 and 2, the mechanical properties are not developed enough to show considerable stress values, as captured in Figure 6-18. However, the stress starts to show considerable magnitudes beginning in Phase 3. Figure 6-19 (a) shows a contour map of the stress at the end of phase 3, right *before* the application of prestressing. Due to local temperature gradient effects, some parts are in compression, particularly the bottom flange where the temperature is the highest (see Figure 6-14). Since there is no external loading during the casting process[5], the structure is in a self-equilibrium state. As a consequence, the compression in the deck and bottom flange is balanced by tension in the web. Moreover, tension also exists near the surfaces due to temperature effects. Figure 6-19 (b) corresponds to the stress state right *after* the prestressing force application (Phase 4). Now, the bottom flange and the web are in compression, but the deck is mostly in tension. Due to some eccentricity of the prestressing force, the inner part of the deck shows larger tensile stress values than the outer part.

Since the plastic strain in the composite matrix corresponds to the cracking in the UHPC structure, the investigation of the matrix plastic strain provides a means to evaluate the risk of cracking during the casting process. There is no plastic strain in Phase 1 and Phase 2 (Figure 6-20), because the mechanical properties are not developed enough to show considerable stress values. Hence, there is no cracking in the structure. However, after removing the inner and outer formwork, some plastic strains occur as illustrated in Figure 6-21. *Before* application of the prestressing force, there exist some plastic strains localized on the deck surface and on the web surface. These localized plastic strains can be attributed to the local temperature gradients close to the surface, which may induce some small surface cracks. *After* prestress application, the plastic strains in the deck increase as a consequence of the tension (Figure 6-19 (b)) in the deck induced by prestressing. On the other hand, the plastic strains in the web do not change, since the web is in compression after prestress application as illustrated in Figure 6-19 (b).

---

[5]Dead weight is neglected.
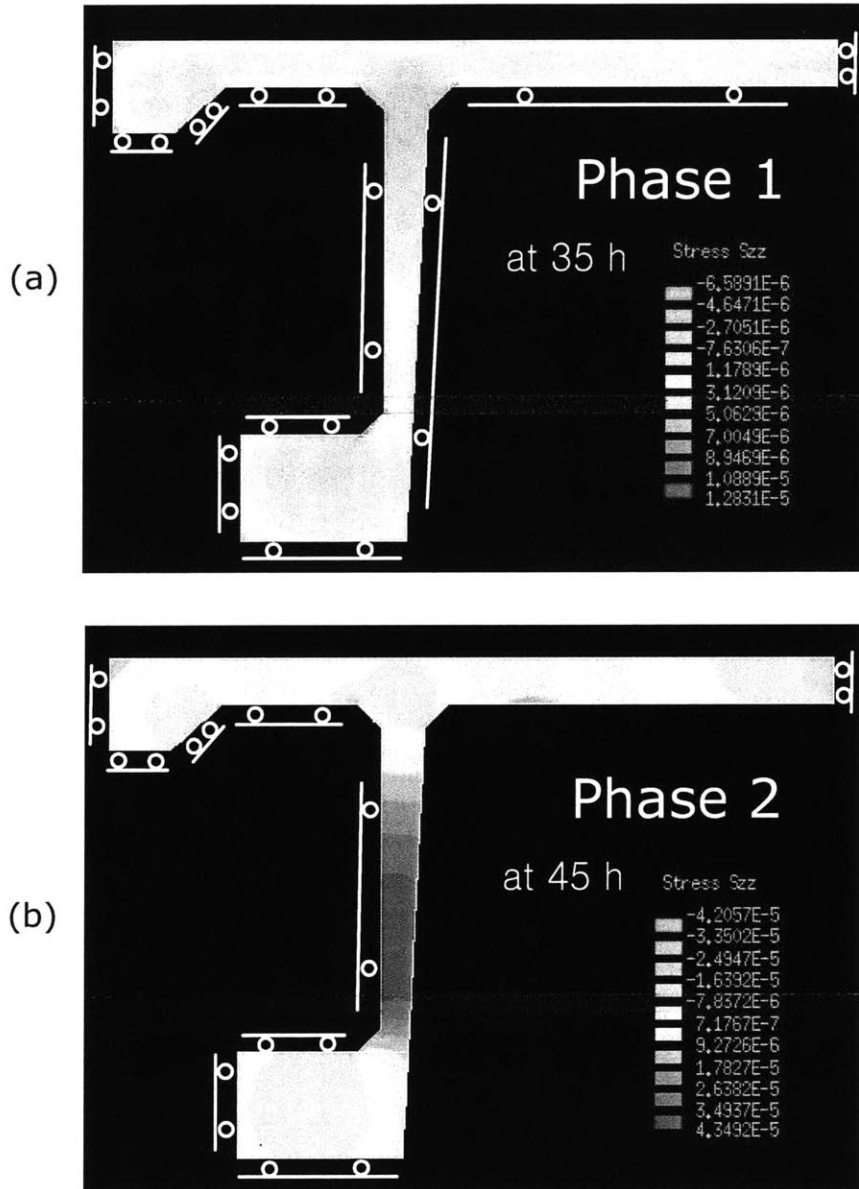
Figure 6-18: Distribution of the longitudinal macroscopic stress (Σ_{zz}): (a) At 35 hours after casting in Phase 1, (b) At 45 hours after casting in Phase 2.
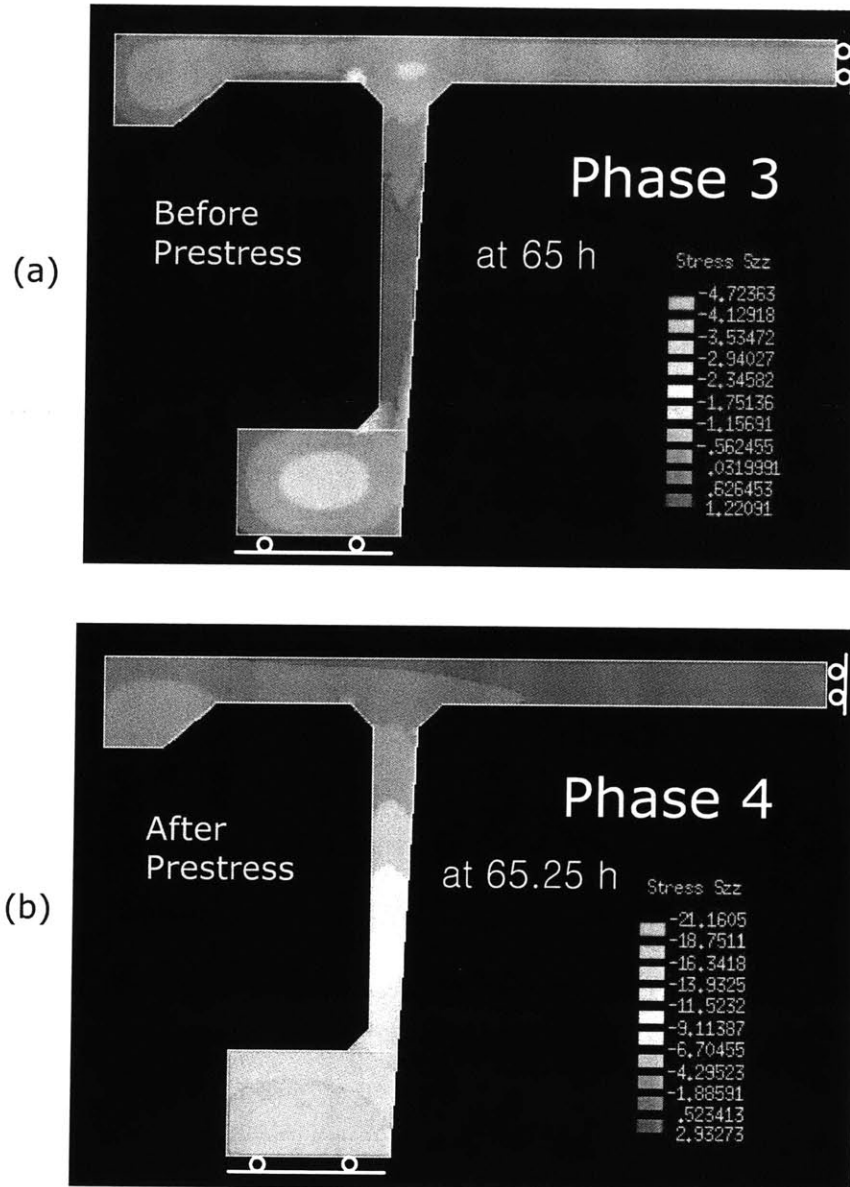
Figure 6-19: Distribution of the longitudinal macroscopic stress (Σ_{zz}): (a) Before prestress application (Phase 3), (b) After prestress application (Phase 4).

135
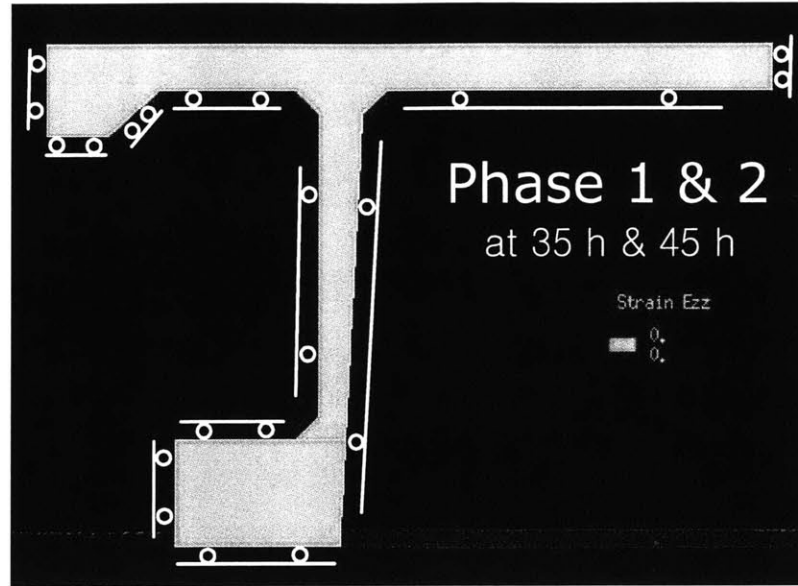
Figure 6-20: Distribution of the longitudinal plastic strain in the composite matrix ($\varepsilon^p_{M,zz}$) at both 35 and 45 hours after casting in Phase 1 and 2, respectively.

6.4.2 Stress and Plastic Strain Before and After Applying Prestress

In order to fully understand what happened, we take a closer look on the stress and plastic strain profiles along the cross section of the web and the deck. Figure 6-22 (a) displays the longitudinal macroscopic stress Σ_{zz} profile along the web. Before prestress application, most of the web is in tension while the center of both deck and bottom flange are in compression. As stated before, this phenomenon is a typical example of a self-balanced stress state. The higher temperatures in the bottom flange and in the deck lead to compression that is balanced by tension in the web. After the application of the compressive prestressing force introduced through the bottom flange, the deck is now in tension while the web and the bottom flange are in compression.

Figure 6-22 (b) shows the cracking strains that are produced by these stresses. The shown plastic strains ($\varepsilon^p_{M,zz}$) imply cracks that open in the z-direction. Before applying the pre-stressing force, small plastic strains already exist in the web and the bottom flange. After the prestressing force application, there is no additional plastic strain created because the web and the bottom flange are in compression. This confirms that the plastic strains along the web are

136
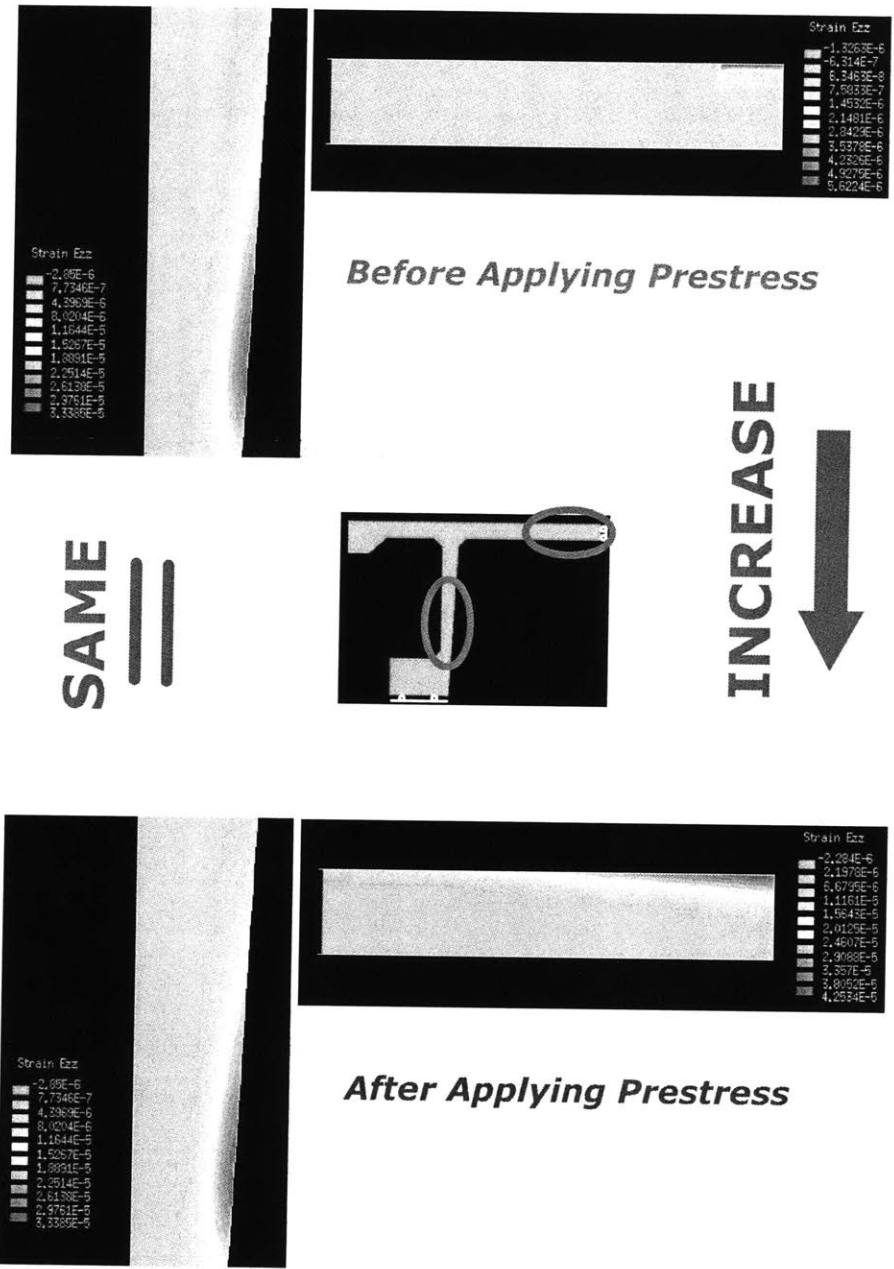
Figure 6-21: Distribution of the longitudinal plastic strain in the composite matrix ($\varepsilon^p_{M,zz}$) in the web (left) and the deck (right) before and after presstress application.

the consequence of the stresses generated due to differential thermal deformation and chemical shrinkage, but the magnitude of the strains is very small, i.e. $max\left[\varepsilon^p_{M,zz}\right] \sim 10^{-5}$.

Figure 6-23 displays longitudinal stresses and plastic strains along the deck surface. As expected from Figure 6-19 (a), most of the deck surface, prior to prestress application, is in tension due to local temperature gradients over the deck thickness (Figure 6-23 (a)). There is a small stress drop in the middle of the deck, which can be attributed to some plastic deformation as a result of these surface temperature gradients. After prestress application, the deck is mostly in tension. An important stress drop is now detected in the center of the deck. The source of this stress drop becomes clear, if we compare this result with that of chemo-elastic simulations which are also displayed in Figure 6-23 (a). The comparison shows a considerable stress drop $(max\,[\Delta\Sigma_{zz}] \sim 2\ MPa)$ in the center of the deck. Hence, this stress drop can be identified as a clear consequence of cracking, and we can expect some plastic strains in the deck.

Figure 6-23 (b) shows the longitudinal plastic strain $(\varepsilon^p_{M,zz})$ profile in the deck. Small plastic strains already exist in the center of the deck before applying the prestressing force. However, the magnitude of these strains is roughly on the same order as the plastic strains observed along the web, i.e. $max\left[\varepsilon^p_{M,zz}\right] \sim 10^{-5}$. These strains are, again, due to local thermal gradient effects. In return, the application of the prestressing force increases the plastic strains by a factor of *five*! This increase allows us to conclude that the risk of cracking was increased considerably by prestress application, which appears to us as the main source of cracking.

6.4.3   Time History of Simulation Results

To make the picture complete, Figure 6-24 displays the time history of the stress and the plastic strains for the three locations shown in Figure 6-9 (deck, web and bottom flange). As we expected, the Σ_{zz}-time history displayed in Figure 6-24 (a) shows a big jump in stresses due to the prestressing force application, which leads to compression in the web and the bottom flange, and to tension in the deck. However, as time goes on, a stress re-distribution occurs due to the stiffness change of the UHPC, which release some compression in the bottom flange that is added to the web.
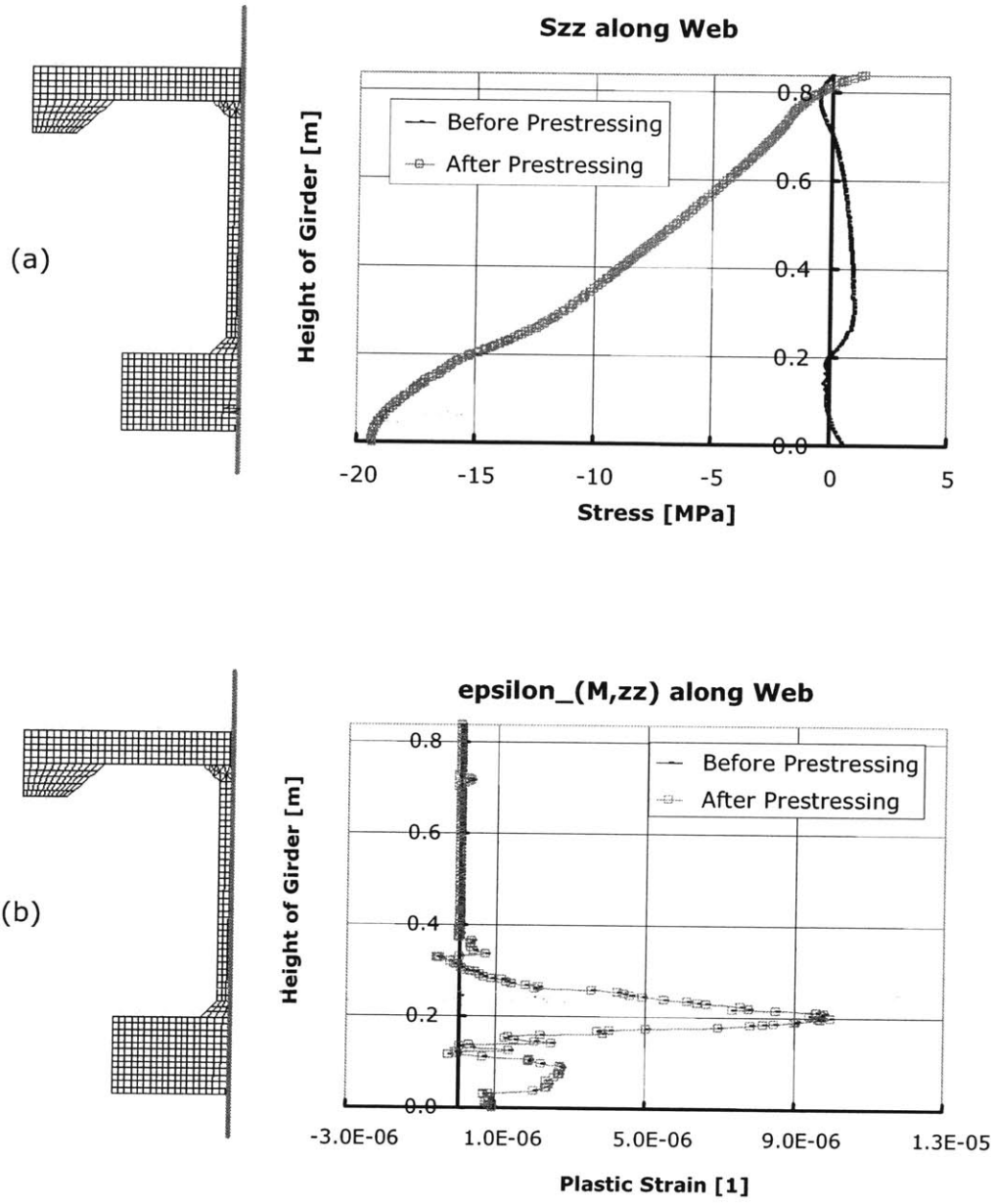
Figure 6-22: (a) Longitudinal macroscopic stress profile along the web, (b) Longitudinal plastic strain in the composite matrix along the web.
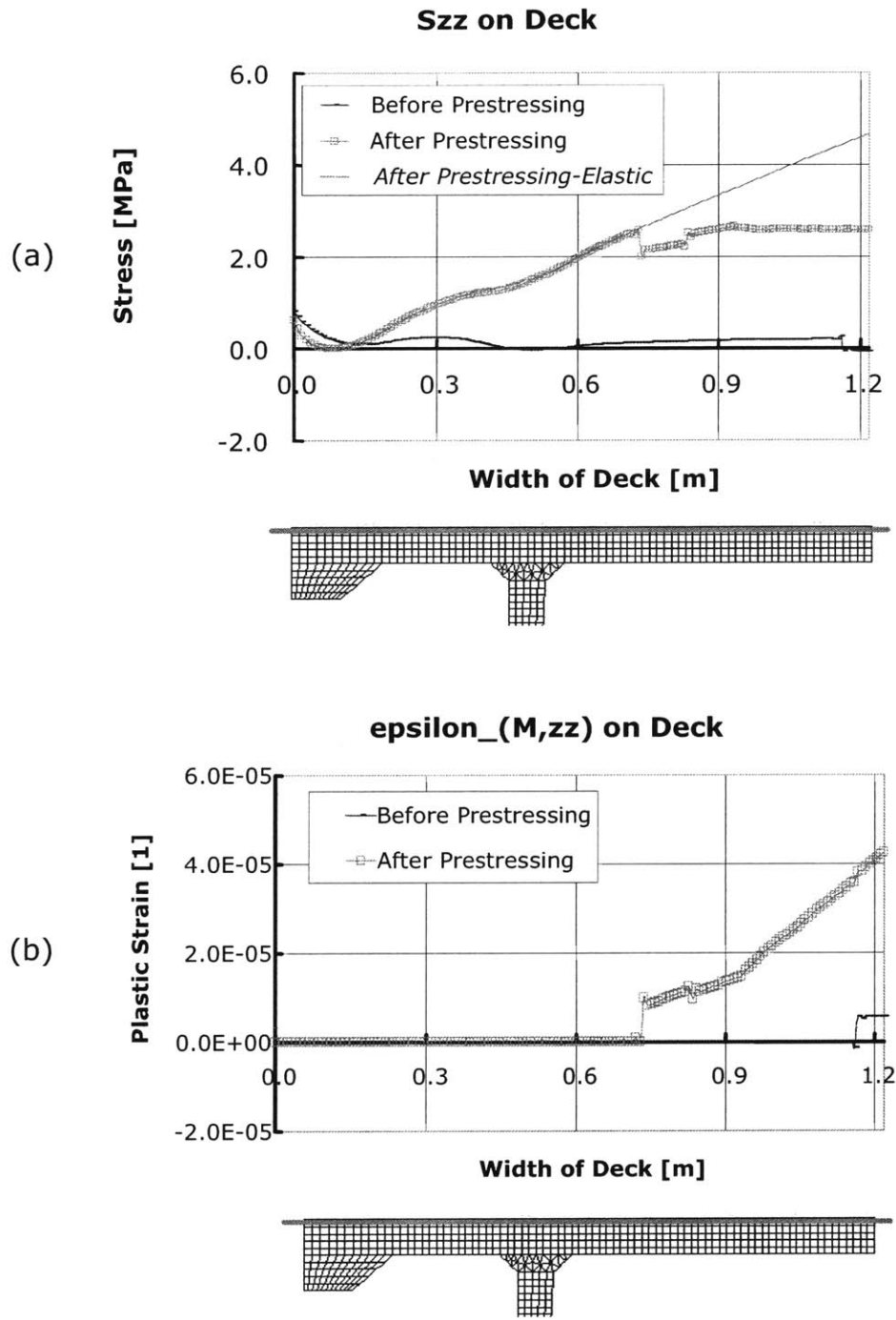
Figure 6-23: (a) Longitudinal macroscopic stress profile in the deck, (b) Longitudinal plastic strain in the composite matrix in the deck.

Figure 6-24 (b) displays the time history of the longitudinal plastic strain of the composite matrix, which captures the cracking. At the moment of removal of the outer-form, some small plastic strains occur in both the deck and the web of roughly the same order of magnitude. While the plastic strains do not change due to prestress application, the plastic strains in the deck increase substantially, inducing a high risk of early-age UHPC cracking of the web.

6.5 Discussion of Simulation Results

What we find from the simulation is that there are some small plastic strains in the web and deck even before applying the prestressing force. These plastic strains which may eventually translate in small surface cracks are very small. However, what is most important is that the plastic strains we find in the deck after applying the prestressing force are non-negligible. This important increase of plastic strains translates into an important risk of cracking of the deck. The simulation results help to understand what was observed on site during the manufacturing process. A longitudinal crack (see Figure 6-3) was found in the web and the deck at mid-span when a full scale girder was transported from the form. In order to take the 21 m long girder out from the formwork, a crane was used with two support points as shown in Figure 6-25. At this time, the deck was already pre-damaged through early application of the prestressing. Once taken out of the formwork, the girder freely bends and is subject to some vibrations. Thus, there was a high risk that the cracks propagate from the already damaged deck into the web down to the neutral axis. Therefore, the observed cracking seems to us a clear consequence of the damage induced by early application of the prestressing, which became apparent once the girder was taken out of the formwork.

To enhance our argument, we performed another simulation, in which the prestress application was delayed, and applied at 120 hours after casting (compared to 65 hours). Figure 6-26 shows the profile of the longitudinal plastic strain in the composite matrix $(\varepsilon^p_{M,zz})$ along the deck surface. The figure shows that the plastic strains could be strongly reduced (roughly half), if the prestress application were delayed to a more advanced hydration state. Hence, it can be concluded that the risk of cracking in the girder could have been reduced by delaying the moment of prestress application.

141

Time History of Szz

(a)

Time History of epsilon_(M,zz)

(b)
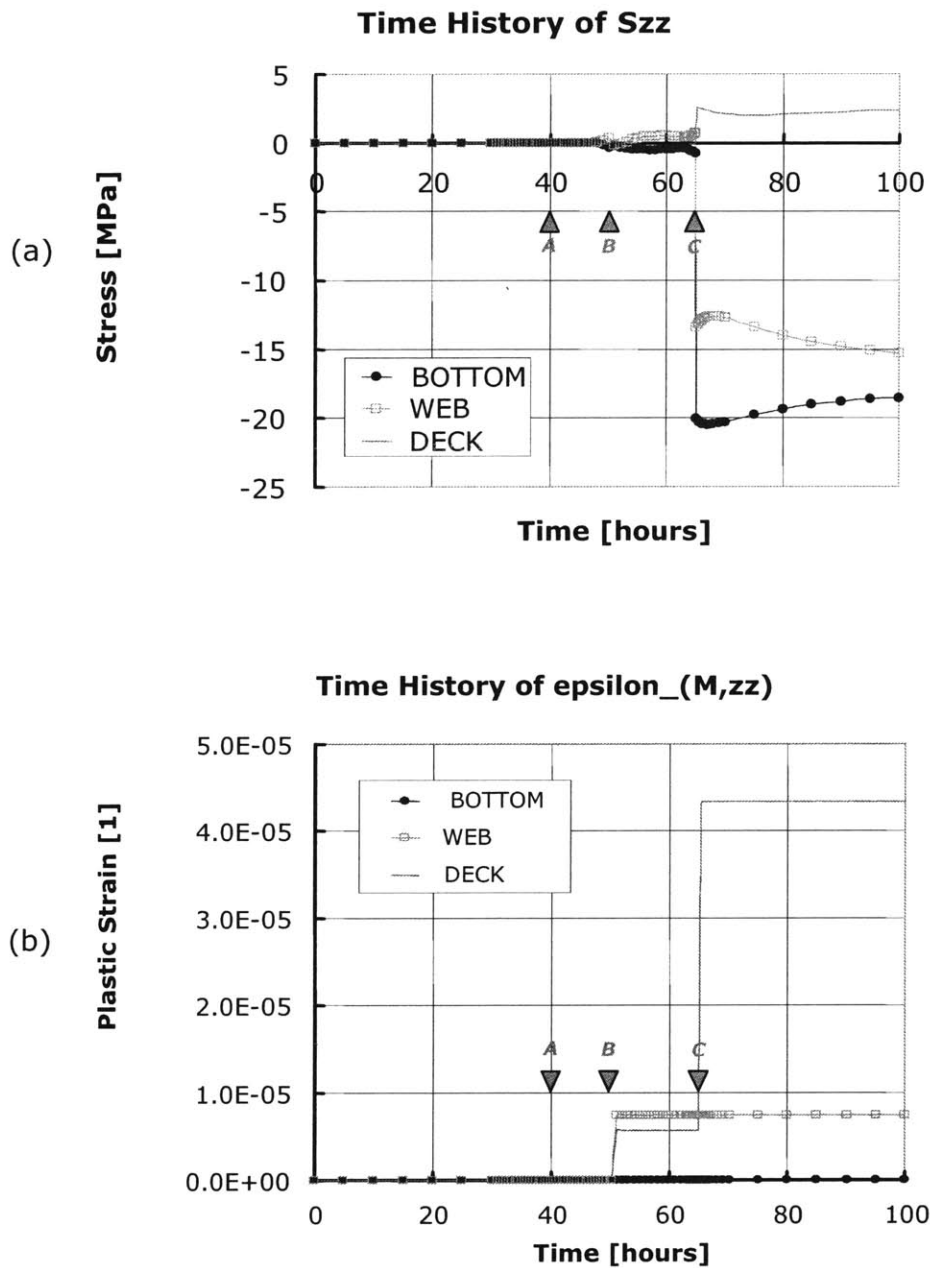
Figure 6-24: (a) Time history of the longitudinal macroscopic stresses, (b) Time history of the longitudinal plastic strains in the composite matrix [The marked triangular points indicate the following: A= inner-form removal, B=outer-form removal and C=prestress application].

(a)

(b)

Figure 6-25: (a) A lateral shot of the girder 21 m long, (b) A full scale girder is removed from the formwork [9].
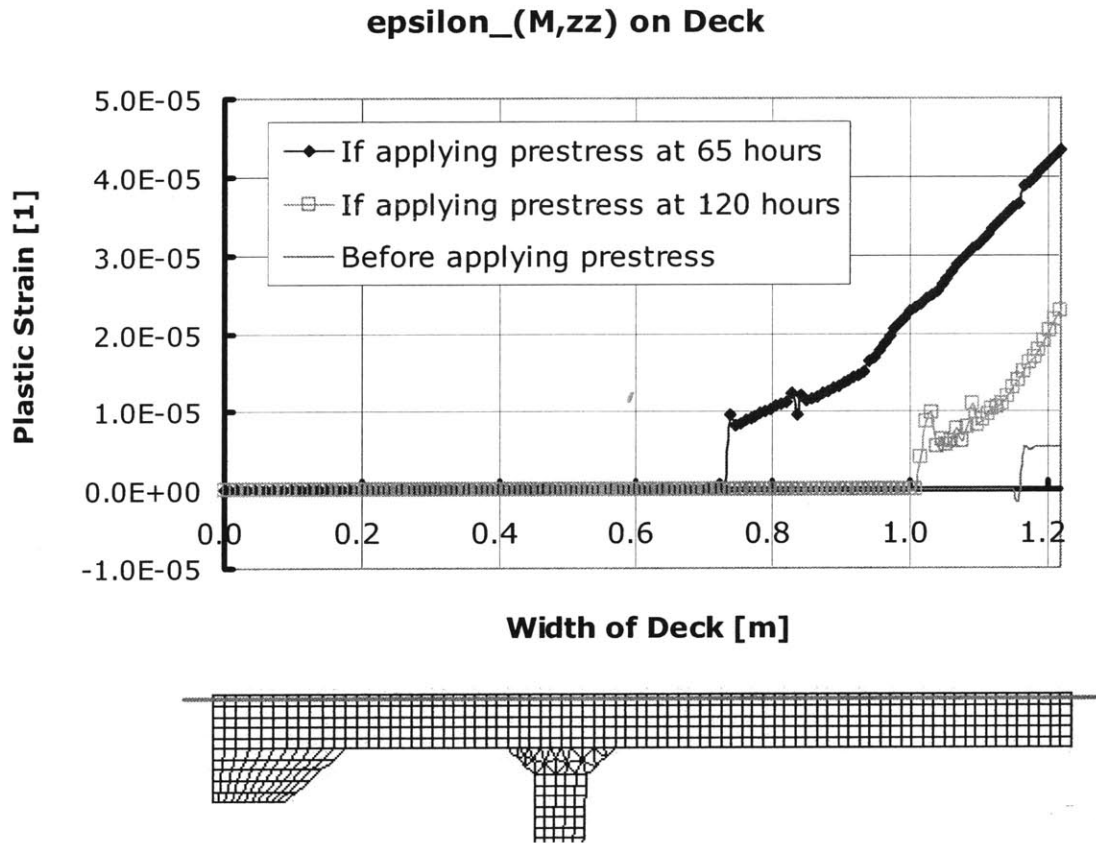
Figure 6-26: Comparison of the longitudinal plastic strains in the composite matrix along the deck.

Beside the moment of prestress application, there are two more main factors which influence the risk of early-age cracking in the considered UHPC bridge girder: autogenous shrinkage and thermal deformation. While the autogenous shrinkage is a material property which cannot be controlled once the material for the structure has been chosen, the thermal deformation can be reduced by maintaining the structure in an isothermal temperature condition. During the casting of the bridge girder, the external temperature varied between 0 $°C$ and 30 $°C$ so that this temperature variation may affect the early-age cracking. Thus, it is also important to take care of the external thermal condition in order to reduce early-age UHPC cracking.

6.6   Chapter Summary

We have raised the question whether it was possible to predict the risk of cracking in early-age UHPC structures, and eventually reduce it - by means of the first-order engineering model developed in this research. The application of the model to evaluate stresses and deformation in the FHWA-UHPC bridge girders provides evidence that it is possible:

- To predict the temperature history and the strain history occurring in the UHPC bridge girders.

- To evaluate the risk of cracking which is quantified in terms of plastic strains of the composite matrix.

This was achieved by means of a first-order engineering model for early-age UHPC materials, which is characterized by a relative small number of input parameters which can be accessed in a rational manner. No doubt, the chosen modeling approach is strongly reductionist, reducing the complex chemical reactions and phenomena that occur in UHPC materials to some very few governing phenomena that are captured by the two-phase thermo-chemo-mechanical UHPC material model, namely:

- The effect of hydration through a single hydration degree, whose evolution is monitored through a macroscopic kinetics law.

- The effect of cracking through a permanent strain associated with the cementitious composite matrix, whose evolution is monitored through strength criteria that depend on the hydration degree.

- The coupling between hydration reaction, temperature and deformation, which are monitored through a highly reduced number of input parameters, that are easily accessible for the engineering practice.

The implementation of the model in a finite element program turns out to be a versatile engineering tool to model the casting of UHPC structures, that allows engineers to predict and reduce the risk of cracking.

Part IV

CONCLUSIONS

Chapter 7

CONCLUSIONS

7.1   Summary of Report

UHPC has remarkable performance in mechanical properties, ductility, economical benefit, etc. However, early-age cracking of UHPC can become an issue during the manufacturing process due to its intrinsic characteristics: the high cement content and the highly exothermic hydration reaction. For this reason, there is a necessity to develop a material model which captures the behavior of UHPC at early ages.

The objective of this research is to develop a new material model for early-age UHPC through a thermodynamics approach. The new model is a two-phase thermo-chemo-mechanical model, which is based on two pillars. The first is a hardened two-phase UHPC material model, and the second is a hydration kinetics model for ordinary concrete.

Before developing the new model, these two theories are reviewed in detail. In the hardened UHPC material model, the matrix and the fiber phases are modeled as two separate macroscopic phases having the same macroscopic strain but different stress states for each phase. The macroscopic model is composed of three parts: a brittle-plastic matrix phase, an elasto-plastic fiber phase and an elastic coupling spring. An abrupt stress drop after the matrix cracking is captured by this macroscopic model, and the plastic strain in the composite matrix represents the cracking of UHPC. This hardened UHPC model is combined with a hydration kinetics model which is based on the application of a decoupling hypothesis which neglects the effect of mechanical change on the thermal and the chemical processes.

148

It is on the basis of these two models that we propose a new constitutive model for early-age UHPC which combines the two-phase hardened UHPC model with the hydration kinetics model. The coupling of these two model is achieved by considering the evolution of the strength and stiffness properties in the two-phase UHPC material model. As a first engineering approach, a linear evolution law is adopted for strength, and stiffness is assumed to follow a nonlinear evolution law. This new two-phase thermo-chemo-mechanical coupling model is implemented in a commercial finite element program, CESAR-LCPC. Finite element formulation including finite element equations and the return mapping algorithm are presented in detail, and the proposed model is verified through simulations of uniaxial tension tests.

The efficiency of the model and finite element program is validated with experimental data obtained during the casting of a Ductal^{TM} optimized bridge girder. Thanks to the decoupling hypothesis, the application of the early-age UHPC model can be carried out in a two-step manner: first the thermo-chemical problem is solved, followed by solving the two-phase thermo-chemo-mechanical problem. The main findings from this application can be summarized as follows:

1. A simulated adiabatic temperature curve which plays a major role in the thermo-chemical problem is obtained from the quasi-isothermal strength values measured on site. From the simulated adiabatic temperature curve and the thermal boundary conditions, the temperature distribution was successfully obtained using the thermo-chemical simulation tool.

2. The distribution of cracks on the deck and the web was predicted with the new two-phase thermo-chemo-mechanical coupling approach. This simulated deformation behavior of the girder compares well with on-site strain measurements. Thanks to the model, the observed crack pattern were explained.

3. The developed engineering tool was also employed to study means to reduce the risk of UHPC cracking. It is recommended that the external thermal condition should be well taken care of, and the moment of applying prestressing force should be delayed.

The most important contribution is the novel macroscopic model for early-age UHPC. By using the two-phase early-age UHPC model, one can evaluate the risk of cracking during the

casting of UHPC structures, and eventually reduce the risk of early-age cracking. The implementation of this model in a finite element program provides a versatile engineering tool for improving the manufacturing of UHPC structures.

7.2   Future Research

The suggested material model for early-age UHPC is limited in several aspects by simplifying assumptions, which should be addressed in future research. This material model adopts simple evolution laws (Laube's law and Byfors' law) for the evolving strength and stiffness with respect to the macroscopic hydration degree. The macroscopic hydration degree concept is only a first step towards a comprehensive materials-to-structural engineering design approach. Recent progress in experimental micro-mechanics makes it possible to assess the elastic properties at very fine scales and to upscale this elastic behavior to large scales by means of homogenization methods [4]. Thus, the simple evolution law for strength and stiffness of the UHPC material can be replaced by the micro-mechanical approach with the homogenization methods.

By using chemo-mechanics and micro-mechanics, a multi-scale hydration kinetics model could be developed to describe the hydration degrees of four clinker phases, i.e. C_3S, C_2S, C_3A and C_4AF. Such a multi-hydration degree approach would involve the activation energy of the four main hydration reactions, which could largely improve the predictive capabilities of our single hydration degree approach, in which we use one single activation energy. This multi-scale hydration kinetic model can then be applied to the two-phase UHPC model proposed in this research. The tasks can be summarized at the different length scales of cementitious materials as follows:

- At a micro-mechanical level, a link needs to be established between the four fundamental chemical hydration reactions and UHPC strength and stiffness properties.

- At the material level, the micro-thermo-chemo-mechanical behavior could be upscaled into a suitable macroscopic UHPC material model.

- At the structural level, such an improved model could examine how UHPC structures must be optimized to minimize the risk of early-age UHPC cracking.

150

Ultimately, it would then be possible to make the link between mix proportion and structural performance, and optimize the mix design for specific structural performances. The work presented here is a first step towards this goal.

Bibliography

[1] Acker, Paul. (2004). Personal Communication.

[2] Bathe, K.J. (1996). *Finite Element Procedures*, Prentice-Hall, Upper Saddle River, New Jersey.

[3] Bentur, A. (2003). "Early Age Cracking in Cementitious Systems", *Report of RILEM Technical Committee 181-EAS: Early age shrinkage induced stresses and cracking in cementitious systems*, Bagneux, France.

[4] Bernard, O., Ulm F.J., and Lemarchand E. (2003). "A multiscale micromechanics-hydration model for the early-age elastic properties of cement-based materials," *Cement and Concrete Research*, September (9): 1293-1309.

[5] Boulay, C., Le Mau, F., Renwez, S., Sercombe, J., and Toutlemonde, F. (1997). "Caractérisation du comportement au choc d'un béton de poudres réactives grâce a des essais de traction direct", *Res Rep. LCPC-BOUYGUES*, Laboratoire Central des Ponts et Chaussées, Paris, France (in French).

[6] Byfors. (1980). "Plain Concrete at Early Ages," *Swedish Cement and Concrete Institute*, Fo 3:80, Stockholm, Sweden.

[7] Chuang, E. (2002). "Ductility Enhancement of High Performance Cementitious Composites and Structures," *Ph.D. Dissertation*, Massachusetts Institute of Technology, Cambridge, Massachusetts.

[8] Chuang, E., and Ulm, F.-J. (2002). "Two-phase composite model for high performance cementitious composites," *Journal of Engineering Mechanics-ASCE*, 128(12), 1314-1323.

[9] Geist, G. (2004). "MIT Optimized Ductal Bridge Girder Castings," Internal Document from Lafarge.

[10] Heukamp, F.H, (2003). "Chemomechanics of calcium leaching of cement-based materials at different scales: the role of CH-dissolution and C-S-H degradation on strength and durability performance of materials and structures," *Ph.D. Dissertation*, Massachusetts Institute of Technology, Cambridge, Massachusetts.

[11] Kupfer, H., Hilsdorf, H., and Rusch. (1969). "Behavior of concrete under biaxial stresses," *ACI Journal*, August, 656-666.

[12] Lafarge North America website. (2004). http://imagineductal.com

[13] Laplante, P. (1993). "Propriétés mécaniques des bétons durcissants: analyse comparée des bétons classiques et à très hautes performances (Mechanical properties of hardening concrete: a comparative analysis of ordinary and high performance concrete)," *Ph.D. Dissertation*, Ecole Nationale des Ponts et Chaussées, Pararis, France (in French).

[14] Laube, M. (1990). "Werkstoffmodell zur berechnung won temperaturspannungen in massigen betonauteilen imm jungen alter," *Docotral Thesis*, TU Braunschweg.

[15] LCPC. (2004). "CESAR-LCPC Manual of Examples: Modeling of Early-Age UHPC," Laboratoire Central des Ponts et Chaussées, Paris, France.

[16] LCPC. (2001). "CESAR-LCPC Manual of Examples: Modeling of Early-Age Concrete," Laboratoire Central des Ponts et Chaussées, Paris, France.

[17] Neville, A.M. (1995). *Properties of Concrete*, Longman, Essex, England.

[18] Park, H. (2003). "Model-Based Optimization of Ultra High Performance Concrete Highway Bridge Girders," *M.S. Thesis*, Massachusetts Institute of Technology, Cambridge, Massachusetts.

[19] Perry, V.H. (2004). Personal Communication.

[20] Prestress Service Inc. (2003). Design Drawings of MIT Optimized Ductal Bridge Girder.

[21] Shim, J.M., and Ulm, F.J. (2004). "3-D Design Simulation and Validation of UHPC Model: The Shawnessy Architectural Structure," *MIT CEE Report R04-09*, Massachusetts Institute of Technology, Cambridge, Massachusetts.

[22] Simo, J., and Hughes, T. (1997). *Computational Inelasticity*, Springer-Verlag, New York.

[23] Tennis, P.D., and Jennings, H.M. (2000). "A Model for Two Types of Calcium Silicate Hydrate in the Microstructure of Portland Cement Pastes," *Cement and Concrete Research*, 30, 855-863

[24] Ulm, F.J., and Coussy, O. (2002). *Mechanics and Durability of Solids, Volume I: Solids Mechanics*, Prentice-Hall, Upper Saddle River, New Jersey.

[25] Ulm, F.J., and Coussy, O. (1995). "Modeling of Thermochemomechanical Couplings of Concrete at Early Ages," *Journal of Engineering Mechanics*, July, 785-794.

[26] Ulm, F.J., and Coussy, O. (1996). "Strength Growth as Chemo-Plastic Hardening in Early Age Concrete," *Journal of Engineering Mechanics*, December, 1123-1132.

[27] Ulm, F.J., and Coussy, O. (2001). "What Is a Massive Concrete Structure at Early Ages?: Some Dimensional Arguments," *Journal of Engineering Mechanics*, May, 512-522.

Appendix A

Plastic Projection Schemes For Triaxial Loading

- Projection Scheme for the Tension Cut-Off Condition:

$$\Delta\lambda_M^{TC} = \frac{I_{1,M}^{tr} - \sigma_{Mt}^{cr}}{9\left(K_M + K_I\right)} \tag{A.1}$$

$$\Delta\lambda_F^{TC} = \frac{I_{1,F}^{tr} - \sigma_{Ft}}{9\left(K_F + K_I\right)} \tag{A.2}$$

- Projection Scheme for the Drucker-Prager Condition:

$$\Delta\lambda_M^{UN} = \frac{\alpha_M^{UN} I_{1,M}^{tr} + \left|\mathbf{s}_M^{tr}\right| - c_M^{UN}}{2\left(G_M + G_I\right) + 9\left(\alpha_M^{UN}\right)^2\left(K_M + K_I\right)} \tag{A.3}$$

$$\Delta\lambda_M^{BI} = \frac{\alpha_M^{BI} I_{1,M}^{tr} + \left|\mathbf{s}_M^{tr}\right| - c_M^{BI}}{2\left(G_M + G_I\right) + 9\left(\alpha_M^{BI}\right)^2\left(K_M + K_I\right)} \tag{A.4}$$

$$\Delta\lambda_F^{DP} = \frac{\alpha_F^{DP} I_{1,F}^{tr} + \left|\mathbf{s}_F^{tr}\right| - c_F^{DP}}{2\left(G_F + G_I\right) + 9\left(\alpha_F^{DP}\right)^2\left(K_F + K_I\right)} \tag{A.5}$$

- Projection Scheme for the Multiple Plastic Surface Condition:

$$
\left\{
\begin{array}{c}
\Delta\lambda_M^{TC} \\[4pt]
\Delta\lambda_F^{TC} \\[4pt]
\Delta\lambda_M^{UN} \\[4pt]
\Delta\lambda_M^{BI} \\[4pt]
\Delta\lambda_F^{DP}
\end{array}
\right\}
= [\mathcal{A}]^{-1}
\left\{
\begin{array}{c}
I_{1,M}^{tr} - \sigma_{Mt}^{cr} \\[6pt]
I_{1,F}^{tr} - \sigma_{Ft} \\[6pt]
\alpha_M^{UN} I_{1,M}^{tr} + \left| \mathbf{s}_M^{tr} + 2G_I \Delta\lambda_F^{DP,q} \mathbf{N_{s_F}^{up,q}} \right| - c_M^{UN} \\[6pt]
\alpha_M^{BI} I_{1,M}^{tr} + \left| \mathbf{s}_M^{tr} + 2G_I \Delta\lambda_F^{DP,q} \mathbf{N_{s_F}^{up,q}} \right| - c_M^{BI} \\[6pt]
\alpha_F^{DP} I_{1,F}^{tr} + \left| \mathbf{s}_F^{tr} + 2G_I \left(\Delta\lambda_M^{UN,q} + \Delta\lambda_M^{BI,q} \right) \mathbf{N_{s_M}^{up,q}} \right| - c_F^{DP}
\end{array}
\right\}
$$

$$\tag{A.6}$$

where $[\mathcal{A}]$ is the following 5×5 symmetric matrix:

$$
[\mathcal{A}] =
\begin{bmatrix}
A_{11} & A_{12} & A_{13} & A_{14} & A_{15} \\
 & A_{22} & A_{23} & A_{24} & A_{25} \\
 & & A_{33} & A_{34} & A_{35} \\
 & & & A_{44} & A_{45} \\
sym. & & & & A_{55}
\end{bmatrix}
\tag{A.7}
$$

where:

$$A_{11} = 9\left(K_M + K_I\right) \; ; \qquad A_{12} = -9K_I \; ;$$

$$A_{13} = 9\alpha_M^{UN}\left(K_M + K_I\right) \; ; \quad A_{14} = 9\alpha_M^{BI}\left(K_M + K_I\right) \; ;$$

$$A_{15} = -9\alpha_F^{DP} K_I \; ;$$

$$A_{22} = 9\left(K_F + K_I\right) \; ; \quad A_{23} = -9\alpha_M^{UN} K_I \; ;$$

$$A_{24} = -9\alpha_M^{BI} K_I \; ; \qquad A_{25} = 9\alpha_F^{DP}\left(K_F + K_I\right)$$

$$A_{33} = 2\left(G_M + G_I\right) + 9\left(\alpha_M^{UN}\right)^2\left(K_M + K_I\right) \; ; \tag{A.8}$$

$$A_{34} = 2\left(G_M + G_I\right) + 9\alpha_M^{UN}\alpha_M^{BI}\left(K_M + K_I\right) \; ;$$

$$A_{35} = -9\alpha_M^{UN}\alpha_F^{DP} K_I$$

$$A_{44} = 2\left(G_M + G_I\right) + 9\left(\alpha_M^{BI}\right)^2\left(K_M + K_I\right) \; ;$$

$$A_{45} = -9\alpha_M^{BI}\alpha_F^{DP} K_I$$

$$A_{55} = 2\left(G_F + G_I\right) + 9\left(\alpha_F^{DP}\right)^2\left(K_F + K_I\right)$$

Appendix B

Input Format for EAHC Module

In CESAR-LCPC, running the EAHC module for the analysis of early-age UHPC reduces to using a new material model. The EAHC module follows the regular input format of CESAR-LCPC, except for the material input parameter. The new material model is assigned $IMOD = 119$, which indicates early-age UHPC for the analysis of the two-phase thermo-chemo-mechanical problem. Several examples which use the proposed material are presented in Reference [15], and Table B.1 provide details for each model parameter of the early-age UHPC model. Furthermore, input parameters and comments for MEXO simulation with plane-section option are presented Table B.2. This is followed by the input files used in the four-phase simulations with TEXO and MEXO. The description of the files is as follows:

$$
\begin{array}{r}
\text{TEXO} \\
\text{Simulation}
\end{array}
\left\{
\begin{array}{ll}
\text{Phase 1:} & grd\_txp1.data \\
\text{Phase 2:} & grd\_txp2.data \\
\text{Phase 3:} & grd\_txp3.data \\
\text{Phase 4:} & grd\_txp4.data
\end{array}
\right.
$$

$$
\begin{array}{r}
\text{MEXO} \\
\text{Simulation}
\end{array}
\left\{
\begin{array}{ll}
\text{Phase 1:} & grd\_ehp1.data \\
\text{Phase 2:} & grd\_ehp2.data \\
\text{Phase 3:} & grd\_ehp3.data \\
\text{Phase 4:} & grd\_ehp4.data
\end{array}
\right.
$$

Input Data	Comments
Title	*Title* = name of element group
$IMOD$ $(INAT)$	$IMOD$ = control variable for the calculation; $IMOD=119$ for early-age UHPC $(INAT)$ = only for 2-D problem
ρg ν C_M C_F M	ρg = volumetric weight ν = Poisson's ratio C_M = stiffness contribution of composite matrix in $[MPa]$ C_F = stiffness contribution of composite fiber in $[MPa]$ M = stiffness of matrix-fiber coupling in$[MPa]$

σ_{Mt} σ_{Mt}^{cr} σ_{Mc} σ_{Mb}	σ_{Mt} = initial tensile strength of composite matrix in $[MPa]$
	σ_{Mt}^{cr} = post-cracking tensile yield strength of composite
	      matrix $[MPa]$
	σ_{Mc} = initial compressive strength of composite matrix
	      in $[MPa]$
	σ_{Mb} = initial biaxial compressive strength of composite
	      matrix in $[MPa]$

σ_{Ft} σ_{Fc}	σ_{Ft} = tensile strength of composite fiber in $[MPa]$ σ_{Fc} = compressive strength of composite fiber in $[MPa]$

α_M $-\beta_M$ ξ_0 $\xi^{initial}$	α_M = thermal dilatation coefficient of composite matrix
	β_M = autogenous shrinkage for composite matrix
	ξ_0 = threshold of the hardened composite matrix
	$\xi^{initial}$ = initial hydration degree indicating whether the
	      group is chemically active or not; $\xi^{initial}=1$ for
	      hardened UHPC and $\xi^{initial}=0$ for early-age
	      UHPC

α_F $-\beta_F$	α_F = thermal dilatation coefficient of composite fiber β_F = autogenous shrinkage for composite fiber; for steel fiber $\beta_F=0$

Table B.1: Input parameters and comments for the early-age UHPC model, $IMOD = 119$. These input parameters are introduced under $ELEM$ in the MEXO input files.

Input Data	Comments
$MEXO$ M $NPAS1$	$MEXO$ = computation module for thermo-chemo-mechanical calculation M = print index; $\quad$ M=0 for printout of the number of time steps $\quad$ M=1 for printout of M=0 plus functions influencing the parameter $\qquad$ and loading functions $\quad$ M=2 for printout of the solution at each time step $\quad$ M=4 for printout of the the stresses at each time step $NPAS1$=number of time steps of the TEXO computation used for the $\qquad$ MEXO computation
TXO $M0$ $NOMF$	TXO = input of the temperature fields and degree of hydration from $\qquad$ the TEXO computation results files; if TXO is not specified $\qquad$ then calculation become hardened UHPC simulation. $M0$ = selection indicator of the time steps stored by TEXO; $\quad$ $M0$=0 if all of the time steps from the TEXO computation are used. $\quad$ $M0$=1 otherwise $NOMF$ = name of the results file created by the TEXO module
INI $NOMF$	INI = initialization of a computation by input from a restart file $NOMF$ = name of the restart file
STK $NOMF$	STK = storage of results at the last time step for a subsequent $\qquad$ computation restart $NOMF$ = name of the file on which the results of the last time $\qquad$ step are stored
EFN $IEPT$ XC, YC $VNM_0[3]$ $VNM_1[3]$ $...$ $VNM_{NPAS1}[3]$	EFN = plane-section computation $IEPT$ = print index; $\quad$ $IEPT$=1 for an unspecified section $\quad$ $IEPT$=2 for a section having y-axis as a symmetric axis $\quad$ $IEPT$=3 for a section having x-axis as a symmetric axis $\quad$ $IEPT$=4 for a section having x- and y-axis as symmetric axes XC, YC = symmetric axis coordinate if $IEPT$ having 2, 3 or 4 $VNM_{IPAS}[3] = N^d$, M_x^d, M_y^d = prescribed force and moments, $\qquad$ which follow the sign conventions in Section 6.3
NIT $IMET$ $NITER$ TOL	NIT = convergence criteria for nonlinear calculation $IMET$ =1 for default convergence checking algorithm in CESAR $NITER$ = maximum number of iteration TOL = tolerance for convergence

Table B.2: Input parameters and comments for MEXO simulation with plane-section option, EFN.

159

```
EXEC
ILIG
COMT
-------------------------------------------------------------------------
-                                                                       -
-                     CESAR-LCPC Version 3.4.x                          -
-                                                                       -
-                                                                       -
-                                                                       -
-  Name of MESH        : grd3                                           -
-  Name of COMPUTATION : tx1                                            -
-                                                                       -
-  Families       : 21  23                                             -
-                                                                       -
-  Module         : TEXO                                               -
-                                                                       -
-  .  2957 nodes                                                        -
-  .     6 groups                                                       -
-  .  1194 elements  :  863 DBQ8        31 DBT6        300 EB3          -
-                                                                       -
-------------------------------------------------------------------------

COOR
    0   1
ELEM
    0   1
Conc1
    1   1
      8.            8.            0.            2700.
Conc2
    1   1
      5.            5.            0.            2700.
Exch1
    1   1
     10.0
Exch2
    1   1
     10.0
Exch3
    1   1
     10.0
Exch4
    1   1
     14.0
CHAR
    2
ECH
    4
    3    1.
    4    1.
    5    1.
    6    1.
IMPR
    0    0
TEXO
```

160

```
    14
    10     .001
    17
     0.
 5
 5
 5
 5
 5
 5
 1
 1
 1
 1
 1
 1
 1
 1
 1
 1
CFT
    18.
 18
 18
 18
 18
 18
 18
 18
 16.75
 15.5
 14.25
 13
 11.75
 10.5
 10
 10
 10
INI
     1
    14.
STK
    grd_txp1.stk
QAB
 56
 0          20          20
 15         20.5        20
 31         21          20
 31.5       21.2        20
 32         21.3        20
 32.5       21.5        20
 33         21.6        20
 33.5       21.7        20
 34         21.8        20
 34.5       22          20
```

35	22.2	20
35.5	22.5	20
36	22.8	20
36.5	23.2	20
37	23.8	20
37.5	25.8	20
38	28.6	20
38.5	32.1	20
39	36.2	20
39.5	40.9	20
40	46.2	20
40.5	52	20
41	57.3	20
41.5	60.7	20
42	63	20
42.5	65	20
43	67	20
43.5	69	20
44	71	20
44.5	72.7	20
45	74.4	20
45.5	76.1	20
46	77.8	20
46.5	79.3	20
47	80.8	20
47.5	82.3	20
48	83.8	20
48.5	85.1	20
49	86.4	20
49.5	87.7	20
50	88.7	20
52	89.7	20
54	90.3	20
56	90.8	20
58	91.3	20
60	91.7	20
62	92.1	20
65	92.3	20
68	92.4	20
71	92.6	20
74	92.8	20
77	93	20
80	93.1	20
83	93.2	20
86	93.25	20
89	93.3	20

```
   0.                   0.                1.
2700.
4000.
```

161

```
EXEC
ILIG
COMT
-------------------------------------------------------------------------
-                                                                       -
-                      CESAR-LCPC Version 3.4.x                         -
-                                                                       -
-                                                                       -
-                                                                       -
-  Name of MESH        : grd3                                           -
-  Name of COMPUTATION : tx1                                           -
-                                                                       -
-  Families            : 21  23                                        -
-                                                                       -
-  Module              : TEXO                                          -
-                                                                       -
-  . 2957 nodes                                                        -
-  .    6 groups                                                       -
-  . 1194 elements  :  863 DBQ8       31 DBT6       300 EB3            -
-                                                                       -
-------------------------------------------------------------------------

COOR
    0   1
ELEM
    0   1
Conc1
    1   1
    8.            8.            0.            2700.
Conc2
    1   1
    5.            5.            0.            2700.
Exch1
    1   1
   10.0
Exch2
    1   1
   10.0
Exch3
    1   1
   14.0
Exch4
    1   1
   14.0
CHAR
    2
ECH
    4
    3    1.
    4    1.
    5    1.
    6    1.
IMPR
    0    0
TEXO
```

162

```
   14
   10    .001
   11
    1.
1
1
1
1
1
1
1
1
1
1
CFT
   10.
10
10
10
10
10
13.5
17
20.5
24
27.5
INI
    3
    grd_txp1.stk
STK
    grd_txp2.stk
QAB
   56
0            20            20
15           20.5          20
31           21            20
31.5         21.2          20
32           21.3          20
32.5         21.5          20
33           21.6          20
33.5         21.7          20
34           21.8          20
34.5         22            20
35           22.2          20
35.5         22.5          20
36           22.8          20
36.5         23.2          20
37           23.8          20
37.5         25.8          20
38           28.6          20
38.5         32.1          20
39           36.2          20
39.5         40.9          20
40           46.2          20
40.5         52            20
```

41	57.3	20
41.5	60.7	20
42	63	20
42.5	65	20
43	67	20
43.5	69	20
44	71	20
44.5	72.7	20
45	74.4	20
45.5	76.1	20
46	77.8	20
46.5	79.3	20
47	80.8	20
47.5	82.3	20
48	83.8	20
48.5	85.1	20
49	86.4	20
49.5	87.7	20
50	88.7	20
52	89.7	20
54	90.3	20
56	90.8	20
58	91.3	20
60	91.7	20
62	92.1	20
65	92.3	20
68	92.4	20
71	92.6	20
74	92.8	20
77	93	20
80	93.1	20
83	93.2	20
86	93.25	20
89	93.3	20

0.	0.	1.
2700.		
4000.		

163

```
EXEC
ILIG
COMT
--------------------------------------------------------------------
-                                                                  -
-                       CESAR-LCPC Version 3.4.x                   -
-                                                                  -
-                                                                  -
-                                                                  -
-  Name of MESH        : grd3
-  Name of COMPUTATION : tx1
-                                                                  -
-  Families        : 21  23                                        -
-                                                                  -
-  Module          : TEXO                                          -
-                                                                  -
-  .  2957 nodes                                                   -
-  .     6 groups                                                  -
-  .  1194 elements  :  863 DBQ8       31 DBT6       300 EB3       -
-                                                                  -
--------------------------------------------------------------------

COOR
   0   1
ELEM
   0   1
Conc1
   1   1
      8.            8.            0.            2700.
Conc2
   1   1
      5.            5.            0.            2700.
Exch1
   1   1
     14.0
Exch2
   1   1
     14.0
Exch3
   1   1
     14.0
Exch4
   1   1
     14.0
CHAR
   2
ECH
   4
   3    1.
   4    1.
   5    1.
   6    1.
IMPR
   2    2
TEXO
```

164

```
   14
   10    .001
   22
    1.
 1
 1
 1
 1
 1
 1
 1
 1
 1
 1
 1
 1
 1
 1
0.25
0.25
0.25
0.25
0.25
0.25
0.25
0.25
CFT
     27.5
30
30
30
30
30
30
30
30
30
30
30
30
28.125
26.25
24.375
22.5
20.625
18.75
16.875
15
INI
    3
    grd_txp2.stk
STK
    grd_txp3.stk
QAB
56
```

0	20	20
15	20.5	20
31	21	20
31.5	21.2	20
32	21.3	20
32.5	21.5	20
33	21.6	20
33.5	21.7	20
34	21.8	20
34.5	22	20
35	22.2	20
35.5	22.5	20
36	22.8	20
36.5	23.2	20
37	23.8	20
37.5	25.8	20
38	28.6	20
38.5	32.1	20
39	36.2	20
39.5	40.9	20
40	46.2	20
40.5	52	20
41	57.3	20
41.5	60.7	20
42	63	20
42.5	65	20
43	67	20
43.5	69	20
44	71	20
44.5	72.7	20
45	74.4	20
45.5	76.1	20
46	77.8	20
46.5	79.3	20
47	80.8	20
47.5	82.3	20
48	83.8	20
48.5	85.1	20
49	86.4	20
49.5	87.7	20
50	88.7	20
52	89.7	20
54	90.3	20
56	90.8	20
58	91.3	20
60	91.7	20
62	92.1	20
65	92.3	20
68	92.4	20
71	92.6	20
74	92.8	20
77	93	20
80	93.1	20
83	93.2	20
86	93.25	20

165

89	93.3	20	
0.		0.	1.
2700.			
4000.			

```
EXEC
ILIG
COMT
--------------------------------------------------------------------    -
-                                                                       -
-                      CESAR-LCPC Version 3.4.x                         -
-                                                                       -
-                                                                       -
-                                                                       -
-  Name of MESH         : grd3
-  Name of COMPUTATION  : tx1
-                                                                       -
-  Families             : 21  23                                        -
-                                                                       -
-  Module               : TEXO                                          -
-                                                                       -
-  .  2957 nodes                                                        -
-  .     6 groups                                                       -
-  .  1194 elements  :  863 DBQ8        31 DBT6        300 EB3          -
-                                                                       -
--------------------------------------------------------------------    -

COOR
     0   1
ELEM
     0   1
Conc1
     1   1
       8.              8.              0.              2700.
Conc2
     1   1
       5.              5.              0.              2700.
Exch1
     1   1
      14.0
Exch2
     1   1
      14.0
Exch3
     1   1
      14.0
Exch4
     1   1
      14.0
CHAR
     2
ECH
     4
     3      1.
     4      1.
     5      1.
     6      1.
IMPR
     2   2
TEXO
```

166

```
    14
    10     .001
    21
     0.25
 0.25
 0.25
 0.25
 0.25
 0.25
 0.25
 0.25
 0.25
 1.00
 1.00
 1.00
 5.00
 5.00
 5.00
 5.00
 5.00
 5.00
10.00
10.00
20.00
CFT
    15.000
 0.000
 0.000
 0.000
 0.000
 0.000
 0.000
 0.000
 0.000
 0.000
 0.000
 0.000
 0.000
 0.000
 0.000
 0.000
 0.000
 0.000
 0.000
INI
     3
    grd_txp3.stk
STK
    grd_txp4.stk
QAB
56
0          20          20
15         20.5        20
```

31	21	20
31.5	21.2	20
32	21.3	20
32.5	21.5	20
33	21.6	20
33.5	21.7	20
34	21.8	20
34.5	22	20
35	22.2	20
35.5	22.5	20
36	22.8	20
36.5	23.2	20
37	23.8	20
37.5	25.8	20
38	28.6	20
38.5	32.1	20
39	36.2	20
39.5	40.9	20
40	46.2	20
40.5	52	20
41	57.3	20
41.5	60.7	20
42	63	20
42.5	65	20
43	67	20
43.5	69	20
44	71	20
44.5	72.7	20
45	74.4	20
45.5	76.1	20
46	77.8	20
46.5	79.3	20
47	80.8	20
47.5	82.3	20
48	83.8	20
48.5	85.1	20
49	86.4	20
49.5	87.7	20
50	88.7	20
52	89.7	20
54	90.3	20
56	90.8	20
58	91.3	20
60	91.7	20
62	92.1	20
65	92.3	20
68	92.4	20
71	92.6	20
74	92.8	20
77	93	20
80	93.1	20
83	93.2	20
86	93.25	20
89	93.3	20
0.	0.	1.

167

2700.
4000.

```
EXEC
ILIG
COMT
-------------------------------------------------------------------------
-                                                                       -
-                         CESAR-LCPC Version 3.4.x                      -
-                                                                       -
-                                                                       -
-  Name of MESH        : grd3                                           -
-  Name of COMPUTATION : mxE1                                           -
-                                                                       -
-  Families       : 1 23                                               -
-                                                                       -
-  Module         : MEXO                                               -
-                                                                       -
-  .  2957 nodes                                                        -
-  .     6 groups                                                       -
-  .  1194 elements :  863 MBQ8      31 MBT6      300 EB3              -
-                                                                       -
-------------------------------------------------------------------------

COOR
    0    1
ELEM
    0    1
Conc1
  119           1
    0.0        0.17        53.9E3       1.0E0       1.65E3
    5.0E0      3.5E0      190.0E0     220.0E0
    4.6E0      9.0E0
    1.0E-5     8.00E-4       0.1          0
    1.0E-5     2.00E-8
Conc2
  119           1
    0.0        0.17        53.9E3       1.0E0       1.65E3
    5.0E0      3.5E0      190.0E0     220.0E0
    4.6E0      9.0E0
    1.0E-5     8.00E-4       0.1          0
    1.0E-5     2.00E-8
Ex1
    1    1
     0.
Ex2
    1    1
     0.
Ex3
    1    1
     0.
Ex4
    1    1
     0.
COND
    2
NUL
```

168

```
    2
  254
    1    2    4    5   13   14   28   29   49   50   52 2211 2195 2194
 2179 2177 2161 2160 2145 2143 2127 2126 2111 2109 2093 2092 2024 2022
 1974 1973 1926 1924 1876 1875 1828 1826 1778 1777 1709 1708 1657 1655
 1609 1608 1569 1567 1533 1532 1499 1498 1465 1464 1431 1430 1397 1396
 1363 1362 1329 1328 1295 1294 1261 1260 1227 1226 1193 1192 1159 1158
 1125 1124 1091 1090 1057 1056 1023 1022  940  939  889  887  851  849
  817  816 2742 2741 2739 2663 2661 2591 2589 2525 2523 2465 2463 2411
 2409 2363 2361 2321 2319 2285 2283 2255 2253 2231 2229 2213 2898 2899
 2903 2904 2908 2909 2913 2914 2918 2919 2923 2924 2928 2929 2933 2934
 2938 2939 2943 2944 2948 2949 2955 2956 2957  936  930  928  929  934
  935  954  955 1037 1038 1071 1072 1105 1106 1139 1140 1173 1174 1207
 1208 1241 1242 1275 1276 1309 1310 1343 1344 1377 1378 1411 1412 1445
 1446 1479 1480 1513 1514 1547 1548 1582 1583 1623 1624 1670 1671 1723
 1724 1792 1793 1841 1842 1890 1891 1939 1940 1988 1989 2037 2038 2107
 2108 2124 2125 2141 2142 2158 2159 2175 1755 1754 1752 1698 1696 1648
 1646 1604 1602 1566 1564 2042 2043 2047 2048 2052 2053 2057 2058 2062
 2063 2067 2068 2072 2073 2077 2078 2082 2083 2089 2090 2091  792  790
  770  768  749  747 2176 2192 2193 2209 2210 2226 1039 1003 1002  980
  978  937
    1    0
    2
  209
  747  717  715  700  698  683  681  666  664  649  647  632  630  615
  613  598  596  581  579  564  562  547  545  530  528  513  511  496
  494  479  477  462  460  445  443  428  426  411  409  394  392  377
  375  360  358  343  341  326  324  309  307  292  290  275  273  258
  256  241  239  224  222  207  205  190  188  173  171  156  154  139
  137  122  120  105  103   88   86   71   69   39   37   21   19    9
    7    3    1 1564 1517 1515 1483 1481 1449 1447 1415 1413 1381 1379
 1347 1345 1313 1311 1279 1277 1245 1243 1211 1209 1177 1175 1143 1141
 1109 1107 1075 1073 1041 1039 2091 2088 2087 2021 2020 1972 1971 1923
 1922 1874 1873 1825 1824 1776 1775 1771 1770 1766 1765 1761 1760 1756
 1755 2957 2954 2953 2894 2893 2856 2855 2818 2817 2813 2812 2808 2807
 2803 2802 2798 2797 2793 2792 2788 2787 2783 2782 2778 2777 2773 2772
 2768 2767 2763 2762 2758 2757 2753 2752 2748 2747 2743 2742 2226 2228
 2247 2249 2274 2276 2307 2309 2346 2348 2391 2393 2442 2444 2499 2501
 2562 2564 2631 2633 2706 2708 2819 2821 2857 2859 2895 2897 2898
    0    1
    0
IMPR
    0    0
MEXO
    2
   17
TXO
    0
    grd_txp1.resu
STK
    grd_ehp1.stk
EFN
 1
 0    0
 0    0    0
```

```
0    0    0
0    0    0
0    0    0
0    0    0
0    0    0
0    0    0
0    0    0
0    0    0
0    0    0
0    0    0
0    0    0
0    0    0
0    0    0
0    0    0
0    0    0
0    0    0
NIT
1    300 0.05
```

169

```
EXEC
ILIG
COMT
-------------------------------------------------------------------------
-                                                                       -
-                        CESAR-LCPC Version 3.4.x                       -
-                                                                       -
-                                                                       -
-                                                                       -
-  Name of MESH        : grd3                                           -
-  Name of COMPUTATION : mxE1                                           -
-                                                                       -
-  Families      : 1  23                                               -
-                                                                       -
-  Module        : MEXO                                                 -
-                                                                       -
-  . 2957 nodes                                                         -
-  .      6 groups                                                      -
-  . 1194 elements :  863 MBQ8        31 MBT6       300 EB3             -
-                                                                       -
-------------------------------------------------------------------------

COOR
   0    1
ELEM
   0    1
Conc1
   119         1
      0.0       0.17        53.9E3      1.0E0      1.65E3
      5.0E0     3.5E0      190.0E0    220.0E0
      4.6E0     9.0E0
      1.0E-5    8.00E-4      0.1         0
      1.0E-5    2.00E-8
Conc2
   119         1
      0.0       0.17        53.9E3      1.0E0      1.65E3
      5.0E0     3.5E0      190.0E0    220.0E0
      4.6E0     9.0E0
      1.0E-5    8.00E-4      0.1         0
      1.0E-5    2.00E-8
Ex1
   1   1
    0.
Ex2
   1   1
    0.
Ex3
   1   1
    0.
Ex4
   1   1
    0.
COND
   2
NUL
```

170

```
   2
 149
   1    2    4    5   13   14   28   29   49   50   52  936  930  928
 929  934  935  954  955 1037 1038 1071 1072 1105 1106 1139 1140 1173
1174 1207 1208 1241 1242 1275 1276 1309 1310 1343 1344 1377 1378 1411
1412 1445 1446 1479 1480 1513 1514 1547 1548 1582 1583 1623 1624 1670
1671 1723 1724 1792 1793 1841 1842 1890 1891 1939 1940 1988 1989 2037
2038 2107 2108 2124 2125 2141 2142 2158 2159 2175 2898 2899 2903 2904
2908 2909 2913 2914 2918 2919 2923 2924 2928 2929 2933 2934 2938 2939
2943 2944 2948 2949 2955 2956 2957 2176 2192 2193 2209 2210 2226 1039
1003 1002  980  978  937 1755 1754 1752 1698 1696 1648 1646 1604 1602
1566 1564 2042 2043 2047 2048 2052 2053 2057 2058 2062 2063 2067 2068
2072 2073 2077 2078 2082 2083 2089 2090 2091
   1    0
   2
 122
2957 2954 2953 2894 2893 2856 2855 2818 2817 2813 2812 2808 2807 2803
2802 2798 2797 2793 2792 2788 2787 2783 2782 2778 2777 2773 2772 2768
2767 2763 2762 2758 2757 2753 2752 2748 2747 2743 2742 2226 2228 2247
2249 2274 2276 2307 2309 2346 2348 2391 2393 2442 2444 2499 2501 2562
2564 2631 2633 2706 2708 2819 2821 2857 2859 2895 2897 2898 1564 1517
1515 1483 1481 1449 1447 1415 1413 1381 1379 1347 1345 1313 1311 1279
1277 1245 1243 1211 1209 1177 1175 1143 1141 1109 1107 1075 1073 1041
1039 2091 2088 2087 2021 2020 1972 1971 1923 1922 1874 1873 1825 1824
1776 1775 1771 1770 1766 1765 1761 1760 1756 1755
   0    1
   0
IMPR
   0    0
MEXO
   2
  11
TXO
   0
    grd_txp2.resu
INI
    grd_ehp1.stk
STK
    grd_ehp2.stk
EFN
 1
 0   0
 0    0    0
 0    0    0
 0    0    0
 0    0    0
 0    0    0
 0    0    0
 0    0    0
 0    0    0
 0    0    0
 0    0    0
 0    0    0
 0    0    0
NIT
 1  300 0.05
```

```
EXEC
ILIG
COMT
----------------------------------------------------------------
-                                                              -
-                    CESAR-LCPC Version 3.4.x                  -
-                                                              -
-                                                              -
-  Name of MESH        : grd3                                  -
-  Name of COMPUTATION : mxE1                                  -
-                                                              -
-  Families      : 1  23                                       -
-                                                              -
-  Module        : MEXO                                        -
-                                                              -
-  . 2957 nodes                                                -
-  .    6 groups                                               -
-  . 1194 elements :  863 MBQ8       31 MBT6      300 EB3       -
-                                                              -
----------------------------------------------------------------

COOR
   0    1
ELEM
   0    1
Conc1
   119          1
     0.0      0.17        53.9E3      1.0E0     1.65E3
     5.0E0    3.5E0      190.0E0    220.0E0
     4.6E0    9.0E0
     1.0E-5   8.00E-4      0.1        0
     1.0E-5   2.00E-8
Conc2
   119          1
     0.0      0.17        53.9E3      1.0E0     1.65E3
     5.0E0    3.5E0      190.0E0    220.0E0
     4.6E0    9.0E0
     1.0E-5   8.00E-4      0.1        0
     1.0E-5   2.00E-8
Ex1
   1    1
    0.
Ex2
   1    1
    0.
Ex3
   1    1
    0.
Ex4
   1    1
    0.
COND
   2
NUL
```

171

```
   2
  11
   1    2    4    5   13   14   28   29   49   50   52
   1    0
   2
  39
2957 2954 2953 2894 2893 2856 2855 2818 2817 2813 2812 2808 2807 2803
2802 2798 2797 2793 2792 2788 2787 2783 2782 2778 2777 2773 2772 2768
2767 2763 2762 2758 2757 2753 2752 2748 2747 2743 2742
   0    1
   0
IMPR
   0    0
MEXO
   2
  22
TXO
   0
     grd_txp3.resu
INI
     grd_ehp2.stk
STK
     grd_ehp3.stk
EFN
  1
  0    0
  0    0    0
  0    0    0
  0    0    0
  0    0    0
  0    0    0
  0    0    0
  0    0    0
  0    0    0
  0    0    0
  0    0    0
  0    0    0
  0    0    0
  0    0    0
  0    0    0
  0    0    0
  0    0    0
  0    0    0
  0    0    0
  0    0    0
  0    0    0
  0    0    0
  0    0    0
NIT
  1  300 0.05
```

```
EXEC
ILIG
COMT
-------------------------------------------------------------------
-                                                                 -
-                    CESAR-LCPC Version 3.4.x                     -
-                                                                 -
-                                                                 -
-                                                                 -
-  Name of MESH        : grd3                                     -
-  Name of COMPUTATION : mxE1                                     -
-                                                                 -
-  Families        : 1  23                                        -
-                                                                 -
-  Module          : MEXO                                         -
-                                                                 -
-   . 2957 nodes                                                  -
-   .    6 groups                                                 -
-   . 1194 elements  :  863 MBQ8      31 MBT6      300 EB3        -
-                                                                 -
-------------------------------------------------------------------

COOR
    0   1
ELEM
    0   1
Conc1
   119        1
     0.0        0.17        53.9E3      1.0E0    1.65E3
     5.0E0      3.5E0      190.0E0    220.0E0
     4.6E0      9.0E0
     1.0E-5     8.00E-4      0.1         0
     1.0E-5     2.00E-8
Conc2
   119        1
     0.0        0.17        53.9E3      1.0E0    1.65E3
     5.0E0      3.5E0      190.0E0    220.0E0
     4.6E0      9.0E0
     1.0E-5     8.00E-4      0.1         0
     1.0E-5     2.00E-8
Ex1
    1   1
     0.
Ex2
    1   1
     0.
Ex3
    1   1
     0.
Ex4
    1   1
     0.
COND
    2
NUL
```

172

```
    2
   11
    1    2    4    5   13   14   28   29   49   50   52
    1    0
    2
   39
 2957 2954 2953 2894 2893 2856 2855 2818 2817 2813 2812 2808 2807 2803
 2802 2798 2797 2793 2792 2788 2787 2783 2782 2778 2777 2773 2772 2768
 2767 2763 2762 2758 2757 2753 2752 2748 2747 2743 2742
    0    1
    0
IMPR
    0    0
MEXO
    2
   21
TXO
    0
   grd_txp4.resu
INI
   grd_ehp3.stk
STK
   grd_ehp4.stk
EFN
 1
 0   0
 0             0             0
-1.2          0.55          0.16
-1.2          0.55          0.16
-1.2          0.55          0.16
-1.2          0.55          0.16
-1.2          0.55          0.16
-1.2          0.55          0.16
-1.2          0.55          0.16
-1.2          0.55          0.16
-1.2          0.55          0.16
-1.2          0.55          0.16
-1.2          0.55          0.16
-1.2          0.55          0.16
-1.2          0.55          0.16
-1.2          0.55          0.16
-1.2          0.55          0.16
-1.2          0.55          0.16
-1.2          0.55          0.16
-1.2          0.55          0.16
-1.2          0.55          0.16
NIT
 1   300 0.05
```